Wrinkling instabilities: modelling, analysis and computation



Hamza Aderemi Alawiye

The Queen's College

University of Oxford

A thesis submitted for the degree of

Doctor of Philosophy

Trinity 2020

Abstract

Wrinkling is a universal instability occurring in a wide variety of engineering and biological materials. Despite extensive study across different systems, a full description is still lacking, particularly in the case of growing materials. Most studies consist of some combination of a substantially simplified elastic model, an analysis that does not go beyond first order, and numerical simulations in commercial software packages that do not necessarily correspond to the mathematical system studied. This thesis addresses all three of these shortcomings by providing a systematic analysis of a fully hyperelastic bilayer past the linear stability threshold into the weakly nonlinear regime, along with a carefully discretised numerical bifurcation analysis of the system.

For comparison, we assume that wrinkling is generated either by the isotropic growth of the film or by the lateral compression of the entire film-substrate system (both in plane strain). We adopt a stream-function-based formulation and perform an exhaustive linear analysis of the wrinkling problem for all stiffness ratios and under a variety of additional boundary and material effects. Namely, we consider the effect of added pressure, surface tension, an upper substrate, and fibres. We obtain analytical estimates of the instability in the two asymptotic regimes of long and short wavelengths.

We then carry out a weakly-nonlinear analysis to derive an amplitude equation that describes the evolution of the wrinkling amplitude beyond the bifurcation point, followed by a comprehensive numerical bifurcation analysis of the problem using the finite element method. We demonstrate excellent agreement between the weakly-nonlinear analysis and the numerical experiments and are also able to directly solve for the bifurcation point in our discretised system and characterise the effect of implementation details such as the aspect ratio of the computational domain on the observed bifurcation point.

We then explore solutions of the amplitude equation in the case that the wrinkling amplitude is allowed to vary over long spatial and/or temporal scales. Finally, we demonstrate that our numerical experiments are able to identify secondary bifurcations in the system similar to those observed in experiments for which analytical methods have thus far been unable to provide a complete explanation.

Acknowledgements

Firstly, I would like to express my deepest gratitude to my supervisors: Professor Alain Goriely and Professor Patrick Farrell. They have patiently provided a near-endless stream of inspiration, ideas, motivation, knowledge, expertise and—perhaps most importantly—humour, without which the realisation of this document would not have been possible. I will look back on my time spent under their tutelage fondly and strive to embody the many lessons they have taught me in my future endeavours.

I owe a great deal of thanks to my undergraduate supervisor Professor Filip Rindler, whose mentorship and encouragement set me on this path, and the EPSRC, whose funding (through award EP/L015811/1) supported me through the course of my studies.

As with most of life's ventures, this thesis was not conceived in isolation. I am fortunate to have been part of such a thriving research community, and have benefited greatly from mathematical discussions with a number of people including Professor S. Jon Chapman, Joseph Hogg, Professor Peter Howell, Attila Kovács, Professor Ellen Kuhl, Professor Simon Tavener, Professor Dominic Vella and Dr. Jessica Williams. Additionally, I'd like to thank the administrative staff at the Mathematical Institute for their support.

It is difficult for me to express the degree to which I feel indebted to my Oxonian friends Archna, Avi, Joseph, Julia, Tessa, Tori and Tristan as well as my sister Salma. Without any one of the people named above, and undoubtedly many others, I might not have had the resolve to finish this thesis. Finally, I would like to thank my parents, Imran and Zaynab, for the spirit of intellectual curiosity that they have fostered in me and their unwavering encouragement over the last 26 years of my life.

Contents

List of Figures **ix**

1 Introduction **1**
1.1 Introduction . . . 1
1.2 Review of wrinkling instabilities . . . 4
1.2.1 Concepts and definitions . . . 5
1.2.2 Biot's instability . . . 8
1.2.3 Growth-induced instabilities . . . 12
1.2.4 Instabilities in multi-layered structures . . . 13
1.2.5 Related topics . . . 14
1.3 Other preliminaries . . . 15
1.3.1 Weakly nonlinear analysis . . . 15
1.3.2 The finite element method . . . 19
1.4 Contribution . . . 23
1.5 Notation . . . 25

2 The model **27**
2.1 General formulation . . . 27
2.2 Growth and compression . . . 28
2.3 Mixed coordinate formulation . . . 30
2.4 Boundary conditions . . . 32

3 Linear analysis **35**
3.1 Perturbation . . . 35
3.2 Bifurcation analysis . . . 37
3.2.1 Compression case . . . 37
3.2.2 Growth case . . . 39
3.3 Generalisations . . . 42
3.3.1 Bilayer with surface tension . . . 42
3.3.2 Bilayer with upper substrate . . . 47
3.3.3 Pressure . . . 50
3.3.4 Fibre-reinforced substrate . . . 52
3.4 Conclusions . . . 54

4 Derivation of the amplitude relation **57**
4.1 Growth case . . . 57
4.1.1 On creasing . . . 62
4.1.2 Verification of the amplitude relation . . . 63
4.2 Compression case . . . 64

5 Numerical bifurcation analysis **67**
5.1 Discretisation of the problem . . . 67
5.2 Computation of bifurcation diagrams . . . 69
5.3 Numerical results . . . 71
5.3.1 Comparison of amplitude of numerical and analytical solutions 73
5.4 Direct computation of the primary bifurcation point . . . 73
5.4.1 Effect of computational domain aspect ratio . . . 74

6 Solutions of the amplitude relation **79**
6.1 Hamiltonian form . . . 79
6.2 Explicit solutions . . . 82

7 Epilogue **85**
7.1 Summary . . . 85
7.2 Future work . . . 86
7.2.1 Numerical realisation of variable amplitude solutions . . . 86
7.2.2 Period-doubling . . . 87
7.2.3 Creasing . . . 89
7.2.4 Three dimensional models . . . 90
7.2.5 Remodelling and general growth laws . . . 91

Appendices

A Boundary conditions **95**
A.1 Regular case . . . 95
A.2 Boundary conditions for an upper substrate . . . 97

B Software availability **99**

References **101**

List of Figures

1.1 3D reconstructions of the cortical folding process in ferret (top) and human (bottom) brains from MR data. Reproduced with permission from Barnette et al. (2009). 2

1.2 Examples of growth-induced wrinkling across different length scales: (A) a bacterial biofilm, (B) a human brain, (C) a pumpkin skin and (D) a Shar-Pei dog. Image A reused from Asally et al. (2012), image B reproduced with permission from Hill and Walsh (2005), image C reused from Yin et al. (2008) ©2008 National Academy of Sciences, image D is by Dave Wharton, used under CC BY-SA 2.0 4

1.3 Experimental image showing the creasing instability in a cross-section of an elastomeric bilayer under compression. In this case, the Young's modulus of the film (green) is approximately 17 times smaller than that of the substrate (black, underneath). The scale bar represents 20 µm. Reproduced with permission from Cai et al. (2012). 16

1.4 A cartoon of an infinite beam attached to a nonlinear Winkler foundation under uniaxial compression. 17

2.1 Geometry of the domain. The system is composed of a bilayer with an infinitely deep layer of width $2L$ bonded by a film of thickness 1. Considering only plane strain, the problem is reduced to the deformation of a two-dimensional system under either compression or growth causing wrinkling. The boundary conditions are: continuity of traction and displacement between the layers, traction free upper layer, no displacement at $Y = -\infty$ and horizontal periodicity. . . . 28

3.1 The maxima of the dispersion curves of $\det(\mathbf{M}) = 0$ in the λ-k plane provide the first critical values of λ at which oscillatory solutions can be obtained. For instance, the critical compression λ_{cr} and wavenumber k_{cr} are indicated for the top curve. The curves from top to bottom are obtained for decreasing values of β. The bottom curve is obtained for a value of $\beta < 1$. 38

3.2 The critical wavenumber $k_{\rm cr}$ and compression $\lambda_{\rm cr}$ as functions of β^{-1}. The two points on the curves correspond to the critical values found for $\beta = 10$. For $\beta < 1$, the critical compression is given by the Biot value and $k_{\rm cr} \to \infty$. The asymptotic estimates provide good approximations of these curves up to $\beta \approx 20$ (red/dashed). Please note that the vertical axis in this figure and similar figures found later in this document represents *both* the wavenumber and the compression as indicated by the curve labels. 39
3.3 Solutions of the dispersion relation for a range of β values. In a thought experiment, the film grows starting at $\gamma = 1$. The homogeneous solution remains stable until a new solution emerges at $\gamma = \gamma_{\rm cr}$ associated with wavenumber $k = k_{\rm cr}$. For $\beta > \beta_{\rm min}$, the solution arises before Biot's instability (indicated by a dashed line).The two upper curves are obtained for values of β just above and just below the critical value $\beta_{\rm min}$. 41
3.4 Critical solutions value of growth and wavenumber as a function of $1/\beta$ (asymptotic approximations shown dashed). Critical solutions exist for $\beta > \beta_{\rm min} \approx 1/1.9$ after which, the Biot instability is the dominant instability. 41
3.5 λ as a function of k for $\beta = 10$, $d = 7.5$ (here $k_{\rm cr} \approx 0.58$ and $\lambda_{\rm cr} \approx 0.78$). 44
3.6 Exact (solid) and approximate (dashed) values of $k_{\rm cr}$ and $\lambda_{\rm cr}$ as functions of β^{-1} for $d = 7.5$ 44
3.7 $k_{\rm cr}$ and $\lambda_{\rm cr}$ as functions of d for $\beta = 10$ 45
3.8 Exact (solid) and approximate (dashed) values of $k_{\rm cr}$ and $\gamma_{\rm cr}$ as functions of β^{-1} for $d = 7.5$ 46
3.9 $k_{\rm cr}$ and $\gamma_{\rm cr}$ as functions of d for $\beta = 10$. 46
3.10 The critical wavenumber $k_{\rm cr}$ and compression $\lambda_{\rm cr}$ as functions of $\beta_{\rm f}^{-1}$ for $\beta_{\rm t} = \beta_{\rm f}/20$ 48
3.11 The critical wavenumber $k_{\rm cr}$ and compression $\lambda_{\rm cr}$ as functions of $\beta_{\rm t}^{-1}$ for $\beta_{\rm f} = 10$ 48
3.12 The critical wavenumber $k_{\rm cr}$ and compression $\lambda_{\rm cr}$as functions of $\beta_{\rm f}^{-1}$ for $\beta_{\rm t} = \beta_{\rm f}/20$ 50
3.13 The critical wavenumber $k_{\rm cr}$ and compression $\lambda_{\rm cr}$ as functions of $\beta_{\rm t}^{-1}$ for $\beta_{\rm f} = 10$ 50
3.14 $k_{\rm cr}$ and $\lambda_{\rm cr}$ as functions of β^{-1} for $m = 5/9$ 53
3.15 $k_{\rm cr}$ and $\lambda_{\rm cr}$ as functions of m for $\beta = 10$ 54
3.16 $k_{\rm cr}$ and $\gamma_{\rm cr}$ as functions of m for $\beta = 10$ 54

4.1 $\mathscr{C}_0$, $\mathscr{C}_1$ and $\mathscr{C}_2$ as functions of β^{-1} in the growth case 62
4.2 Growth factor $\gamma_{\rm ss}$ at the super-to-sub transition 62

4.3 $\mathscr{C}_0$, $\mathscr{C}_1$ and $\mathscr{C}_2$ as functions of β^{-1} in the compression case 66

5.1 Example numerical wrinkling solution for $\beta = 4$, $\gamma = 1.303$ (colored by strain—we can see the mesh because the strain approximation is discontinuous) 71
5.2 Observed amplitude of numerical solutions (black) and amplitude relation (4.22) (orange) for $\beta \in \{20, 10, 4, 2\}$. The amplitude relation (which is valid for a small perturbation of γ_{cr}) shows good agreement with the numerics well into the post-buckling regime. 72
5.3 Error in computed bifurcation point as a function of aspect ratio α for $\beta = 2.5$ 76
5.4 Computed critical growth factor as a function of β^{-1}. For each value of β considered, we performed the computations for 11 uniformly spaced aspect ratios $\alpha \in [1, 1.5]$ (all shown) 76

6.1 Potentials for which v_{-2} vanishes 81
6.2 Potentials for which v_{-2} does not vanish 81
6.3 Profile of a subcritical variable amplitude solution for $\beta^{-1} = 1.01$, $\gamma = \gamma_{\text{cr}} - 0.01^2$. Note that the aspect ratio is not 1:1 84

7.1 Example of the same localised alteration to a wrinkling solution in different places for $\gamma = 1.27$, $\beta = 10$. 87
7.2 Experimental images demonstrating the evolution of a wrinkling instability into a period-doubling instability. Reproduced with permission from Pocivavsek et al. (2008) and Brau et al. (2011). . . 88
7.3 Period-doubled finite element solution in the compression case with $\beta = 100$, $\lambda = 0.6425$ (top). Further continuation to $\lambda = 0.5925$ brings the top surface into a deeply folded configuration approaching self contact (bottom). 89
7.4 Self-intersecting numerical solution (top) with zoom detail (bottom) for $\beta = 5$, $\gamma \approx 1.3$. 90
7.5 Morphologies in numerical solutions for the anisotropic growth tensor (7.2) with $\beta = 20$ and various $\gamma \in [1, 1.6]$. 92

We are not interested in the fact that the brain has the consistency of cold porridge.

— Alan M. Turing

1 Introduction

Contents

1.1 Introduction 1
1.2 Review of wrinkling instabilities 4
1.2.1 Concepts and definitions 5
1.2.2 Biot's instability 8
1.2.3 Growth-induced instabilities 12
1.2.4 Instabilities in multi-layered structures 13
1.2.5 Related topics 14
1.3 Other preliminaries 15
1.3.1 Weakly nonlinear analysis 15
1.3.2 The finite element method 19
1.4 Contribution 23
1.5 Notation 25

1.1 Introduction

While Turing's throwaway comment at the beginning of a radio discussion (Turing, 1952) on the possibility of artificial intelligence largely holds true—for the most part, the mysteries of the *function* of the brain offer greater allure than those concerning its *form*—it belies the considerable complexity that underpins the shape of many organs and it is only recently that we have begun to apply sufficiently rich mathematical models of biological tissues to understand why the porridge-like mass

in each of our crania has the intricate structure that it does. The morphogenesis of the mammalian brain is a fine example of growth-induced pattern formation: in humans, the growth of the embryonic cortex accompanies a transformation from a largely smooth surface to one featuring deep folds beginning around 24 weeks of gestation (shown in fig. 1.1). All over the human body (and indeed in many other biological systems), there are similarly complex examples of shapes and structures that form as we grow. These growth processes are driven by the interplay of genetics, biochemistry and mechanics and have been the subject of study since at least the time of Galileo (Galilei, 1638). Perhaps most famously, D'Arcy Thompson's treatise *On Growth and Form* (Thompson, 1961) made a particularly detailed case for the consideration of physical forces and mathematical laws in understanding the form of living beings. From this work and others (a brief history can be found in Taber (1995), Ambrosi et al. (2011) or Goriely (2017)), the field of growth biomechanics began to take root.

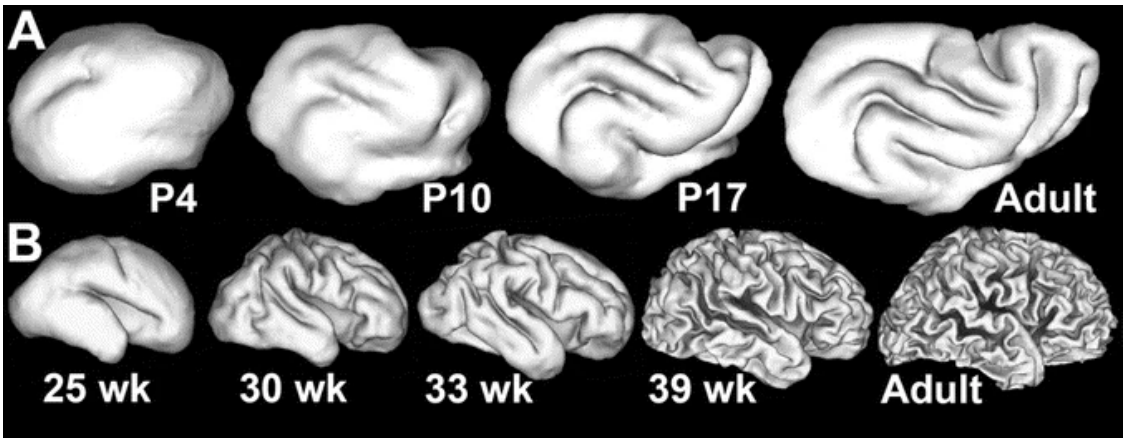


Figure 1.1: 3D reconstructions of the cortical folding process in ferret (top) and human (bottom) brains from MR data. Reproduced with permission from Barnette et al. (2009).

During the mid-20th century, papers such as Mooney (1940) and Rivlin (1948) began the crucial work of extending the hugely successful theory of linear elasticity (which is itself a generalisation of Hooke's law—*ut tensio, sic vis* (Hooke, 1678)) to describe the behaviour of bodies that undergo large deformations. This was spurred in part by an explosion in the use of rubber as a wartime material despite a purely empirical understanding of its properties. Based on largely forgotten work

by Cauchy in the previous century (Cauchy, 1823; Cauchy, 1827), the resulting *theory of nonlinear elasticity* has been a scientific and mathematical triumph, finding wide applicability in engineering contexts as well as driving progress in pure mathematical areas such as the calculus of variations.

In time, it was recognised that the vocabulary of nonlinear elasticity had many insights to offer to biomechanics, where many materials undergo large deformations (Skalak, 1981). While both growth processes and elastic responses can both readily be described in the language of kinematics, the interplay between them can be subtle: stress influences growth and growth influences stress. A crucial leap in the understanding of how to marry these effects was the application of a *decomposition of the deformation gradient* in Rodriguez, Hoger, and McCulloch (1994), a codification of the idea that an *observed* growth deformation can be understood on a local level as the composition of a growth operation from one stress-free state to another (which does not have to vary continuously in space) with an elastic operation that ensures the body is in a physically realisable state. This decomposition has become the basis of a large body of work, including this thesis, though there are still outstanding questions revolving around whether the growth part of the decomposition can be shown to be governed by some constitutive relation. Discussion of the history of this approach in biomechanics can be found in the review articles Garikipati (2009) and Menzel and Kuhl (2012).

With this framework in place, many instances of growth-induced pattern formation, some examples of which are illustrated in fig. 1.2, can be viewed through the lens of mechanical instability—they arise by a process analogous to the buckling of beams or columns (as studied in Euler (1744)). The existence of non-homogeneous patterns after growth corresponds to a bifurcation in the equilibrium equations of the system after the addition of an incremental deformation. While this approach is well studied in traditional elastic contexts, it is not immediately obvious that the residual stresses that result from growth processes can induce mechanical instabilities alone. Indeed, it is only in the past two decades that this has conclusively shown to be the

case (Ben Amar and Goriely, 2005). This thesis presents a comprehensive analysis of one such growth-induced instability: wrinkling.

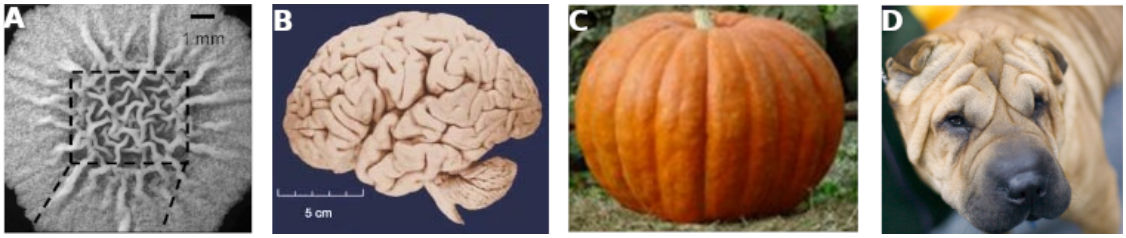


Figure 1.2: Examples of growth-induced wrinkling across different length scales: (A) a bacterial biofilm, (B) a human brain, (C) a pumpkin skin and (D) a Shar-Pei dog. Image A reused from Asally et al. (2012), image B reproduced with permission from Hill and Walsh (2005), image C reused from Yin et al. (2008) ©2008 National Academy of Sciences, image D is by Dave Wharton, used under CC BY-SA 2.0

1.2 Review of wrinkling instabilities

The systematic study of wrinkling instabilities in soft materials began in earnest in the late 20th century. Tanaka et al. (1987) demonstrated that polymer gels immersed in liquid evolve patterns on their surface as they swell and derived the scaling behaviour of the wrinkling wavelength with respect to the thickness of the gel. Bowden et al. (1998) deposited thin metal films on thermally expanded polymers to create visually striking ordered networks of patterns after cooling, noting that the controlled generation of such patterns could be used to create optical components such as diffraction gratings. This marks a shift in attitude towards the occurrence of instability in engineering contexts: instead of being viewed as a failure mode (as it is in the case of buckling structural supports in buildings, for instance), it was promoted as a novel fabrication method. In subsequent years, many similar experimental observations and analyses were conducted in areas of application such as flexible electronics (Khang et al., 2006; Lacour et al., 2004), stimuli-responsive biomaterial design (Kim, Yoon, and Hayward, 2010; Cao et al., 2014) and measurement of material properties (Chung, Nolte, and Stafford, 2011). In the study of growth, these techniques were used to provide insight into the morphogenesis of human brains (Ben Amar and Bordner, 2017; Goriely et al., 2015),

intestines (Ben Amar and Jia, 2013), skin (Ciarletta and Ben Amar, 2012) and other organs (Ciarletta, Balbi, and Kuhl, 2014; Li et al., 2011).

1.2.1 Concepts and definitions

We begin by giving an introduction to the formalism of kinematics and nonlinear elasticity. The interested reader can find a more detailed treatment in Ciarlet (1987).

The fundamental abstraction of the theory of elasticity is the *body*, a region of three-dimensional space that we identify with a *reference configuration* $\mathcal{B} \subset \mathbb{R}^3$. A *deformation* is a sufficiently smooth, orientation-preserving, injective mapping $\boldsymbol{\chi} : \mathcal{B} \to \mathbb{R}^3$. We denote a point in the reference configuration by $\mathbf{X}$ with its coordinates with respect to a standard orthonormal basis denoted by (X, Y, Z). We denote points in the image of $\boldsymbol{\chi}$, also referred to as the *deformed configuration* by $\mathbf{x}$, expressed by its coordinates with respect to the same standard basis as (x, y, z). Note that, in general, these bases need not coincide but for the purposes of this thesis we will not need to consider this generality. It is sometimes convenient to work in terms of the displacement $\mathbf{u} \coloneqq \boldsymbol{\chi} - \mathbf{id}$ instead of the deformation itself.

To understand the geometric effect of a deformation, we must consider how a vector in the tangent space of a point in $\mathcal{B}$ is transformed by $\boldsymbol{\chi}$. The linear map that describes this transformation is known as the *deformation gradient* $\mathbf{F}$ is defined by

$$\mathbf{F} \coloneqq \frac{\partial \boldsymbol{\chi}}{\partial \mathbf{X}}. \tag{1.1}$$

Local changes in volume after the deformation are determined by the *Jacobian determinant*

$$J \coloneqq \det \mathbf{F}. \tag{1.2}$$

By considering the Taylor expansion of $\boldsymbol{\chi}$ around a point $\mathbf{X}$, we find that we can express the transformation of an infinitesimal length element by the action of the *right Cauchy-Green strain tensor*

$$\mathbf{C} \coloneqq \mathbf{F}^\top \mathbf{F}. \tag{1.3}$$

In order to complete our picture of the physics of deformations, we must also be able to described forces acting on bodies. By drawing on the axioms of force balance and moment balance along with the stress principle of Cauchy and Euler, one can deduce the existence of the *Cauchy stress tensor* $\mathbf{T} : \boldsymbol{\chi}(\mathcal{B}) \to \mathrm{Sym}_3(\mathbb{R})$, which satisfies the *equations of equilibrium in the deformed configuration*

$$\begin{aligned} -\operatorname{\mathbf{div}} \mathbf{T} &= \rho \mathbf{b} \qquad \text{in } \boldsymbol{\chi}(\mathcal{B}), \\ \mathbf{T}\mathbf{n} &= \mathbf{s} \qquad \text{on } \boldsymbol{\chi}(\Gamma_1) \subset \boldsymbol{\chi}(\partial\mathcal{B}), \end{aligned} \tag{1.4}$$

where ρ is the mass density, $\mathbf{b}$ is the acting *body force density*, $\mathbf{s}$ is the acting *surface force density* and $\mathbf{n}$ is the surface normal vector, all measured in the deformed configuration. In this thesis, we will only consider conservative forces. An equivalent expression to (1.4) in the reference configuration can be found by considering the *first Piola-Kirchhoff stress tensor* $\mathbf{T}_0 : \mathcal{B} \to \mathrm{M}_3(\mathbb{R})$, defined by

$$\mathbf{T}_0(\mathbf{X}) = J(\mathbf{X})\mathbf{T}(\boldsymbol{\chi}(\mathbf{X}))(\mathbf{F}(\mathbf{X}))^{-\top}. \tag{1.5}$$

The *equations of equilibrium in the reference configuration* are given by

$$\begin{aligned} -\operatorname{\mathbf{div}} \mathbf{T}_0 &= \rho_0 \mathbf{b}_0 \qquad \text{in } \mathcal{B}, \\ \mathbf{T}_0\mathbf{N} &= \mathbf{s}_0 \qquad \text{on } \Gamma_1, \end{aligned} \tag{1.6}$$

where $\rho_0 = J\rho \circ \boldsymbol{\chi}$ is the mass density, $\mathbf{b}_0 = \mathbf{b} \circ \boldsymbol{\chi}$ is the acting *body force density*, $\mathbf{s}_0 = J|\mathbf{F}^{-T}\mathbf{n}|\mathbf{s} \circ \boldsymbol{\chi}$ is the acting *surface force density* and $\mathbf{N}$ is the surface normal vector, all measured in the reference configuration.

We call a material *elastic* if its first Piola-Kirchhoff stress tensor only depends on $\boldsymbol{\chi}$ through its gradient—i.e.

$$\mathbf{T}_0(\mathbf{X}) = \hat{\mathbf{T}}_0(\mathbf{F}(\mathbf{X}), \mathbf{X}). \tag{1.7}$$

This is equivalent to the Cauchy stress tensor having the same property. We call an elastic material *hyperelastic* if there exists a *stored energy function* $W : \mathrm{M}_3^+(\mathbb{R}) \times \mathcal{B} \to \mathbb{R}$ such that

$$\hat{\mathbf{T}}_0(\mathbf{F}, \mathbf{X}) = \frac{\partial W}{\partial \mathbf{F}}(\mathbf{F}, \mathbf{X}). \tag{1.8}$$

If this is the case, then solving the equations of equilibrium of the system can be seen as a necessary condition for the minimisation of the *total energy functional*—defined by

$$I(\boldsymbol{\chi}) = \int_{\mathcal{B}} W(\mathbf{F}(\mathbf{X}), \mathbf{X}) \, \mathrm{d}\mathbf{X} + \int_{\mathcal{B}} \rho_0 V(\boldsymbol{\chi}) \, \mathrm{d}\mathbf{X} - \int_{\Gamma_1} \mathbf{s}_0 \cdot \boldsymbol{\chi}(\mathbf{X}) \, \mathrm{d}A, \tag{1.9}$$

where V is a potential for the body force—over the space of *admissible deformations*: those deformations which satisfy an imposed displacement on some set $\Gamma_0 \subset \partial\mathcal{B}$.

For many materials, the energetic cost of changing the volume is extremely large. In these materials, it is often convenient to model them as being *incompressible*, where we further restrict the set of admissible deformations to require that $J = 1$ everywhere. This is equivalent to replacing the stored energy function with

$$\overline{W}(\mathbf{F}(\mathbf{X}), \mathbf{X}) \coloneqq W(\mathbf{F}(\mathbf{X}), \mathbf{X}) - p(J(\mathbf{X}) - 1), \tag{1.10}$$

where p is a Lagrange multiplier. We can compute the first Piola-Kirchhoff stress using this modified energy function

$$\overline{\mathbf{T}}_0(\mathbf{F}) \coloneqq \frac{\partial \overline{W}}{\partial \mathbf{F}}(\mathbf{F}), \tag{1.11}$$

(dropping $\mathbf{X}$ dependence for notational convenience) and push it forward to obtain the Cauchy stress

$$\begin{aligned} \overline{\mathbf{T}} &= J^{-1} \overline{\mathbf{T}}_0 \mathbf{F}^\top \\ &= J^{-1} \left(\frac{\partial W}{\partial \mathbf{F}} \mathbf{F}^\top - p(\operatorname{cof} \mathbf{F}) \mathbf{F}^\top \right) \\ &= \hat{\mathbf{T}} - p\mathbf{1}, \end{aligned} \tag{1.12}$$

where $\mathbf{1}$ is the identity matrix in $\mathrm{M}_3(\mathbb{R})$. This gives us a physical interpretation for p: it represents a hydrostatic pressure that has no effect on the motion itself. The equations of equilibrium for incompressible elasticity in the reference configuration are then given by

$$\begin{aligned} -\mathbf{div}(\mathbf{T}_0 - p \operatorname{cof} \mathbf{F}) &= \rho_0 \mathbf{b}_0 \qquad \text{in } \mathcal{B}, \\ J &= 1 \qquad \text{in } \mathcal{B}, \\ \mathbf{T}_0 \mathbf{N} &= \mathbf{s}_0 \qquad \text{on } \Gamma_1, \end{aligned} \tag{1.13}$$

and now features an additional unknown: p. The simplest explicit hyperelastic model is the incompressible *neo-Hookean* material, which can be derived from statistical thermodynamic models of rubber (Treloar, 1956). It has a stored energy density function given by

$$W(\mathbf{F}, \mathbf{X}) = \frac{\mu}{2}\left(\mathrm{tr}(\mathbf{F}^\top \mathbf{F}\right) - 3) = \frac{\mu}{2}\left(\mathrm{tr}(\mathbf{C}) - 3\right) \tag{1.14}$$

where $\mu > 0$ is the *shear modulus* of the rubber in its unstressed state (Biot, 1963).

1.2.2 Biot's instability

One of the first mathematical studies of wrinkling in elastic solids came from Biot in his seminal paper (Biot, 1963). In this work, he considers an incompressible elastic half-space under uniform compression of two different types, each of which induces a *surface instability*—at some critical value of compression, a family of deformations that display periodic oscillation localised to the surface of the material become viable solutions of the equilibrium equations of elasticity. The wavelength of the oscillations along the surface of the material is undetermined by the theory as there is no possible choice of a length scale for an infinite half plane. Here we give an exposition of this result (drawing on additional material presented in Biot (1965) and Goriely (2017)), which will allow us to fix notation and terminology for the rest of this thesis.

The body under consideration is an incompressible neo-Hookean half-space occupying the region $Y > 0$ under uniform compression in the X direction. A unit cube in the material has normal stresses T_{11}, T_{22} and T_{33} applied to its faces to become a cuboid with side lengths λ_1, λ_2 and λ_3 after deformation. The deformation gradient $\mathbf{F}$ is then $\mathrm{diag}(\lambda_1, \lambda_2, \lambda_3)$, the stored energy density is given by

$$W(\mathbf{F}, \mathbf{X}) = \frac{\mu}{2}(\lambda_1^2 + \lambda_2^2 + \lambda_3^2 - 3), \tag{1.15}$$

and incompressibility means that the stretches must satisfy

$$\lambda_1 \lambda_2 \lambda_3 = 1. \tag{1.16}$$

From (1.12) we see that we can write the components of the Cauchy stress as

$$\begin{aligned} T_{11} &= \mu\lambda_1^2 - p, \\ T_{22} &= \mu\lambda_2^2 - p, \\ T_{33} &= -p, \end{aligned} \tag{1.17}$$

Let us now consider the case of *plane strain* compression, where the body is subjected to a force in only the first direction and is constrained in the third direction, i.e. $T_{22} = 0$ and $\lambda_3 = 1$. We can then describe the deformation in terms of a single stretch λ:

$$\lambda_1 = \lambda, \quad \lambda_2 = \frac{1}{\lambda}. \tag{1.18}$$

Solving (1.17) for p gives us

$$T_{11} = \mu\left(\lambda^2 - \frac{1}{\lambda^2}\right) \tag{1.19}$$

We can now introduce a two-dimensional *incremental deformation* around the homogeneous solution we computed above. This consists of perturbing the deformation

$$\boldsymbol{\chi}(\mathbf{X}) = \boldsymbol{\chi}^{(0)}(\mathbf{X}) + \epsilon\boldsymbol{\chi}^{(1)}(\boldsymbol{\chi}^{(0)}(\mathbf{X})), \tag{1.20}$$

where $\boldsymbol{\chi}^{(0)}$ is the homogeneous deformation considered above and ϵ is a small parameter, and the pressure

$$p = p^{(0)} + \epsilon p^{(1)}. \tag{1.21}$$

The surface normal in the deformed configuration then has an expansion of the form

$$\mathbf{n} = \mathbf{n}^{(0)} + \epsilon\mathbf{n}^{(1)}, \tag{1.22}$$

and the deformation gradient $\mathbf{F}$ can then be computed to be

$$\mathbf{F} = \left(\mathbf{1} + \epsilon\mathbf{F}^{(1)}\right)\mathbf{F}^{(0)}. \tag{1.23}$$

We then perform a perturbation expansion of $\overline{\mathbf{T}}$ to first order, i.e. substitute

$$\overline{\mathbf{T}} = \overline{\mathbf{T}}^{(0)} + \epsilon\overline{\mathbf{T}}^{(1)} + O(\epsilon^2), \tag{1.24}$$

and use the constitutive relation (1.12) to express $\overline{\mathbf{T}}^{(1)}$ in terms of $\mathbf{F}^{(0)}$ and $\mathbf{F}^{(1)}$:

$$\overline{\mathbf{T}}^{(0)}+\epsilon\overline{\mathbf{T}}^{(1)}+O(\epsilon^2)=\left.\frac{\partial W}{\partial \mathbf{F}}\right|_{\mathbf{F}=(\mathbf{1}+\epsilon\mathbf{F}^{(1)})\mathbf{F}^{(0)}}\mathbf{F}^{(0)\top}(\mathbf{1}+\epsilon\mathbf{F}^{(1)})^{\top}-(p^{(0)}+\epsilon p^{(1)})\mathbf{1}. \quad (1.25)$$

Hence, at each order in ϵ, we have

$$\begin{aligned}\overline{\mathbf{T}}^{(0)}&=\left.\frac{\partial W}{\partial \mathbf{F}}\right|_{\mathbf{F}=\mathbf{F}^{(0)}}\mathbf{F}^{(0)\top}-p^{(0)}\mathbf{1},\\ \overline{\mathbf{T}}^{(1)}&=\left((\mathbf{F}^{(1)}\mathbf{F}^{(0)}):\left.\frac{\partial^2 W}{\partial \mathbf{F}^2}\right|_{\mathbf{F}=\mathbf{F}^{(0)}}\right)\mathbf{F}^{(0)\top}+\left.\frac{\partial W}{\partial \mathbf{F}}\right|_{\mathbf{F}=\mathbf{F}^{(0)}}\mathbf{F}^{(0)\top}\mathbf{F}^{(1)\top}-p^{(1)}\mathbf{1}.\end{aligned} \quad (1.26)$$

Substituting in the neo-Hookean energy density gives us

$$\begin{aligned}\overline{\mathbf{T}}^{(0)}&=\mu\mathbf{F}^{(0)}\mathbf{F}^{(0)\top}-p^{(0)}\mathbf{1},\\ \overline{\mathbf{T}}^{(1)}&=\mu(\mathbf{F}^{(1)}\mathbf{F}^{(0)}\mathbf{F}^{(0)\top}+\mathbf{F}^{(0)}\mathbf{F}^{(0)\top}\mathbf{F}^{(1)\top})-p^{(1)}\mathbf{1}.\end{aligned} \quad (1.27)$$

The components of the Cauchy stress at first order are given by

$$\begin{aligned}T^{(1)}_{11}&=2\mu\lambda^2F^{(1)}_{11}-p^{(1)},\\ T^{(1)}_{22}&=2\mu\lambda^{-2}F^{(1)}_{22}-p^{(1)},\\ T^{(1)}_{12}&=T^{(1)}_{21}=\mu(\lambda^{-2}F^{(1)}_{12}+\lambda^2F^{(1)}_{21}).\end{aligned} \quad (1.28)$$

The equations of equilibrium (1.4) can then be solved at each order in ϵ. At first order, these read:

$$\begin{aligned}-\operatorname{\mathbf{div}}\overline{\mathbf{T}}^{(1)}&=\mathbf{0} \qquad \text{in } \boldsymbol{\chi}(\mathcal{B}),\\ \overline{\mathbf{T}}^{(0)}\mathbf{n}^{(1)}+\overline{\mathbf{T}}^{(1)}\mathbf{n}^{(0)}&=\mathbf{0} \qquad \text{on } \boldsymbol{\chi}(\Gamma_1),\end{aligned} \quad (1.29)$$

with the incompressibility constraint $J=1$ becoming

$$\operatorname{tr}\mathbf{F}^{(1)}=0, \quad (1.30)$$

where we have used the approximation to the determinant at the identity

$$\det(\mathbf{1}+\epsilon\mathbf{A})=1+\operatorname{tr}(\mathbf{A})\epsilon+O(\epsilon^2). \quad (1.31)$$

This linear system of equations is homogeneous and admits periodic solutions of the form

$$\begin{aligned}\boldsymbol{\chi}^{(1)}(x,y)&=\begin{pmatrix}a_x\\ a_y\end{pmatrix}e^{ikx+ik\zeta y},\\ p^{(1)}(x,y)&=ika_pe^{ikx+ik\zeta y},\end{aligned} \quad (1.32)$$

where the unknown a_x, a_y and a_p (but not k) are determined up to a single degree of freedom by the solutions of the following solvability condition:

$$\lambda^2 + (\lambda^2 + \lambda^{-2})\zeta^2 + \lambda^{-2}\zeta^4 = 0. \tag{1.33}$$

This equation has four solutions ($\zeta = \pm i$ and $\zeta = \pm\lambda^2 i$), but only those which correspond to incremental deformations which decay at infinity are of physical relevance, leaving us with $\zeta_1 = i$ and $\zeta_2 = \lambda^2 i$. Each solution ζ_i allows us to specify a_x, a_y and a_p in terms of a single parameter a_i, so (1.32) now reads

$$\begin{aligned} \boldsymbol{\chi}^{(1)}(x,y) &= \begin{pmatrix} a_1 \\ a_1 i \end{pmatrix} c_1 e^{ikx-ky} + \begin{pmatrix} a_2 \\ a_2\lambda^{-2} i \end{pmatrix} c_2 e^{ikx-\lambda^2 ky}, \\ p^{(1)}(x,y) &= i a_1 c_1 k(\lambda^2 - \lambda^{-2}) e^{ikx-ky}, \end{aligned} \tag{1.34}$$

where the a_i, c_i, k and λ remain undetermined. The final stage is the application of the stress-free boundary condition on the surface of the half-space. At each order in ϵ, an outward normal vector at the free surface is given by

$$\begin{aligned} \mathbf{n}^{(0)} &= -\begin{pmatrix} 0 \\ 1 \\ 0 \end{pmatrix}, \\ \mathbf{n}^{(1)} &= -\begin{pmatrix} (a_1 c_1 + a_2 c_2 \lambda^{-2}) k e^{ikx} \\ 1 + (a_1 c_1 + a_2 c_2) i k e^{ikx} \\ 0 \end{pmatrix}. \end{aligned} \tag{1.35}$$

Substituting this into (1.29) shows that nonzero incremental deformations are viable when λ is a root of

$$1 - 4\lambda^2 + 2\lambda^4 + \lambda^8. \tag{1.36}$$

The only positive real root of this polynomial with $\lambda \neq 1$ is given by

$$\lambda_{\text{biot}} \coloneqq \frac{1}{3}\left((17 + 3\sqrt{33})^{1/3} - \frac{2}{(17 + 3\sqrt{33})^{1/3}} - 1\right) \approx 0.543689. \tag{1.37}$$

Thus, we have found a critical compression ratio at which an incremental deformation featuring periodic oscillations at the surface of the half-space becomes a solution of the equations of equilibrium—i.e. a wrinkling instability. The physical interpretation of this finding is not immediately obvious: both the amplitudes a_i and the wavenumber k of the oscillations are left undetermined by the analysis. Indeed, in

a half-space (which is not physically realisable), there is no defining length scale to make sense of these notions. In practice, experiments with finite rubber blocks show that they develop localised *creasing* instabilities at much lower compressions—typically around $\lambda \approx 0.65$—than those predicted by the above analysis. Nonetheless, this prototypical example sets out a general method by which one might compute the critical strain required to induce wrinkling which can then be applied to geometries for which this instability is actually realised.

1.2.3 Growth-induced instabilities

As briefly mentioned previously, volumetric growth processes can generate residual stresses in elastic bodies (Skalak et al., 1996). It has been shown (Ben Amar and Goriely, 2005) that these stresses can be sufficient to induce an instability even in the absence of external loading. Here, we demonstrate how the method of incremental deformations described in the previous section can be modified to incorporate the effects of volumetric growth.

The mathematical foundation of our continuum-mechanical model is the theory of volumetric morphoelasticity—a kinematic "description of growth processes that change the shape and volume of a body and quantify the stresses generated through these processes" (Goriely, 2017). The crucial ingredient in this adaptation is the aforementioned decomposition of the deformation gradient (due to Rodriguez, Hoger, and McCulloch (1994)):

$$\mathbf{F} = \mathbf{A}\mathbf{G}, \tag{1.38}$$

where $\mathbf{A}$ is the *elastic deformation tensor* (which describes deformations resulting from stresses) and $\mathbf{G}$ is the *growth tensor* (which describes the addition of new material). By this decomposition, growth of three-dimensional bodies is broken down into two constituent parts: a local growth process followed by the development of elastic strains to maintain the integrity of the body. The stored energy density W is now considered as a function of $\mathbf{A} = \mathbf{F}\mathbf{G}^{-1}$ and the condition of elastic incompressibility reads $\det \mathbf{A} = 1$. The growth tensor $\mathbf{G}$ may vary throughout the

material, but is often taken to be constant or piecewise constant. The formulation of appropriate constitutive laws to govern the form of $\mathbf{G}$ is still an area of active research (Menzel and Kuhl, 2012). Note that in the incompressible case, the Jacobian determinant now satisfies

$$J = \det \mathbf{F} = \det(\mathbf{AG}) = \det \mathbf{G}. \tag{1.39}$$

The method of incremental deformations then proceeds as demonstrated for Biot's instability and has been successfully applied to model surface wrinkling in biological tissues such as mucosa (Li et al., 2011) and indeed the cortex of the brain. While the precise details of the mechanical basis of cortical folding are still the subject of active research, there is mounting evidence that the key ingredient driving the process is the volumetric expansion of the tissue itself (Xu et al., 2010; Bayly et al., 2013; Bayly, Taber, and Kroenke, 2014; Budday, Steinmann, and Kuhl, 2014). In particular, it was recently demonstrated that the wrinkling instability also correctly captures variations of thickness between the ridges and grooves (gyri and sulci) of the cerebral cortex in both analogue polymer experiments and computational simulations (Holland et al., 2018).

1.2.4 Instabilities in multi-layered structures

Multi-layered elastic materials have been widely studied in the engineering literature with applications ranging from construction materials (Allen, 1969) to 3D printing. These structures are of immediate interest in the context of almost all of the previously mentioned biological tissues—many organs are inhomogeneous and/or anisotropic in their composition. However, the differences in mechanical properties between these different layers of biological tissue may be subtle, which rules out often-used simplifying assumptions such as extreme stiffness ratios and necessitates the exploration of the intermediate parameter space in full generality.

Perturbation methods have been used to great success to compute the critical uniaxial compression required to cause buckling of an elastic half-space coated in a thin, stiffer elastic film (Cai and Fu, 1999). Following works have considered

variations of the physical setting such as pre-stretching the substrate (Cao and Hutchinson, 2012), further compressing the buckled bilayer to induce a second, periodic-doubling bifurcation (Fu and Cai, 2015), the limiting behaviour of the system as the stiffness ratio of the layers tends to unity (Fu and Ciarletta, 2015), the effect of adding reinforced fibres to the substrate (Stewart et al., 2016) and the replacement of compression with growth as a mechanism to induce buckling (Ben Amar and Bordner, 2017).

This final modification is of particular relevance in the study of the morphogenesis of the brain. The physical structure of mammalian brains consists of distinct layers of cells with similar, but different mechanical properties and thicknesses. In particular, we can divide the brain into the outer layer of grey matter (the cortex), which primarily consists of neuron cell bodies, and the inner white matter (the subcortex), which primarily consists of axons and their insulating myelin sheaths.

Experimental verification of these theories is currently limited due to the difficulties involved in acquiring and mechanically testing brain matter *in utero*, but advances in noninvasive imaging techniques may provide the data needed to better validate their predictions (Ronan et al., 2013; Garcia et al., 2018). Recently, it has been demonstrated that it is possible to capture the mechanical response of brain tissue in an elasticity-based framework (Mihai et al., 2017). Furthermore, preliminary numerical simulations have been able to demonstrate—at least phenomenologically—brain morphogenesis in this framework (see Bayly et al. (2013) and Budday et al. (2015)).

1.2.5 Related topics

Plate models

A slightly different approach to wrinkling and similar pattern formation phenomena comes from works of plates bounded on a substrate (Audoly and Boudaoud, 2008; Kohn, 2014). In these works, elastic sheets bonded to elastic substrates are modelled using a variational form of the von Kármán plate equations (which can be derived from full 3D nonlinear elasticity (Ciarlet, 1997)) and identifies wrinkling as the

result of competition between minimisation of the nonconvex membrane energy and the regularising bending energy. In particular, scaling laws of the energy with respect to thickness of the elastic sheet were identified and it was demonstrated that this fitted with characteristic wrinkling patterns seen in the physical world (Kohn and Nguyen, 2013; Bella and Kohn, 2017). While these studies provide precise estimates, they have a limited (and well acknowledged) range of validity regarding properties of the displacement field of the plate which cannot capture some of the phenomenology we see in thick, multi-layered elastic media.

Creasing

Another important related phenomenon in the theory of soft solids is *creasing*, where a sharp, self contacting region forms almost instantaneously when a critical compression is exceeded, as demonstrated in fig. 1.3. Experimentally, this is seen to occur at a lower critical strain than that predicted by Biot's analysis (Trujillo, Kim, and Hayward, 2008) and in recent years, an understanding of this phenomenology as a separate elastic surface instability has been developed (Li et al., 2012). This has come from both numerical studies (Hohlfeld and Mahadevan, 2011; Hong, Zhao, and Suo, 2009) and recent asymptotic analyses (Karpitschka et al., 2017; Ciarletta, 2018), which address the mathematical difficulties involved in capturing the discontinuities associated with the presence of the sharp crease through use of coupled radial near-field and far-field solutions.

1.3 Other preliminaries

1.3.1 Weakly nonlinear analysis

It has long been known that linear methods are not sufficient to capture the post-buckling behaviour of materials. Perhaps most famously, Koiter (1945) demonstrated that a nonlinear theory was required in order to explain discrepancies between predicted and experimentally observed critical loads in thin structures such as shells and plates. Depending on the setting, it was found that the linear theory might significantly underestimate or overestimate the load that a structure could

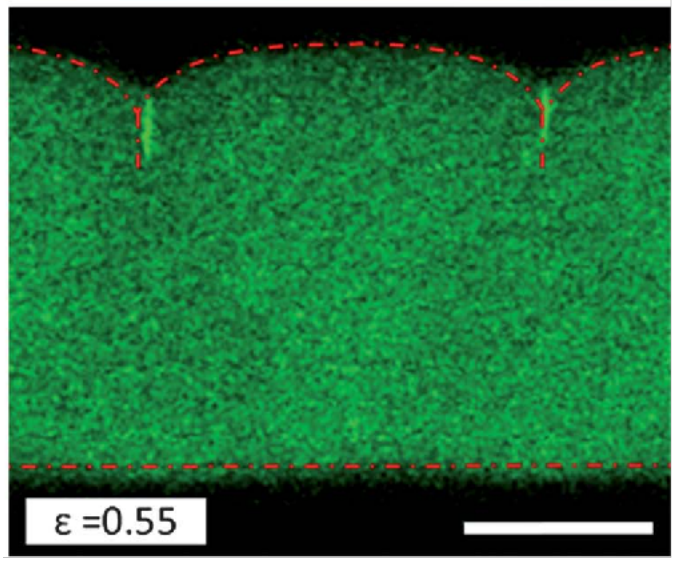


Figure 1.3: Experimental image showing the creasing instability in a cross-section of an elastomeric bilayer under compression. In this case, the Young's modulus of the film (green) is approximately 17 times smaller than that of the substrate (black, underneath). The scale bar represents 20 µm. Reproduced with permission from Cai et al. (2012).

endure before buckling, either of which could have negative consequences in the context of aeronautical engineering that motivated much work in the field at the time. In the following decades, advances were made including the development of methods involving multiple scales (Lange and Newell, 1971) and the extension of these methods to the significantly more algebraically complex setting of nonlinear elasticity (Fu and Ogden, 1999).

Here, we give an exposition of one such method applied to a toy problem that shares some features of the wrinkling problem of interest to us. The key idea is that we must examine perturbation expansions involving higher order terms. In particular, the bifurcation parameter is perturbed past the critical value computed from the first order analysis. By solving the equilibrium equations of the system at higher orders, the undetermined amplitude of the first order solution can be computed. To illustrate this process, we demonstrate it on the problem of the planar deflection of an infinite, uniform Euler-Bernoulli beam attached to a cubically nonlinear Winkler foundation—that is to say that the restoring force to a deflection of the beam is determined locally, but is not linear. A schematic of this quasi-physical model is shown in fig. 1.4. Static configurations of such a rod under the

action of a compressive force P along the length of the rod (in the x direction) satisfy the following (scaled) nonlinear ODE:

$$\frac{\mathrm{d}^4 v}{\mathrm{d}x^4} + P\frac{\mathrm{d}^2 v}{\mathrm{d}x^2} + v - \kappa_2 v^2 - \kappa_3 v^3 = 0 \qquad x \in \mathbb{R}, \tag{1.40}$$

where v is the displacement in the y direction and the κ_i are parameters describing the nonlinearity of the foundation (they have no direct physical interpretation). In the case of a finite but long rod, we can consider the effect of different boundary conditions at the rod ends (see Lange and Newell (1971) for details), but this will not be necessary for the infinite case. This model is well studied in the literature; a similar analysis to what will follow can be found in Fu (2001), for example.

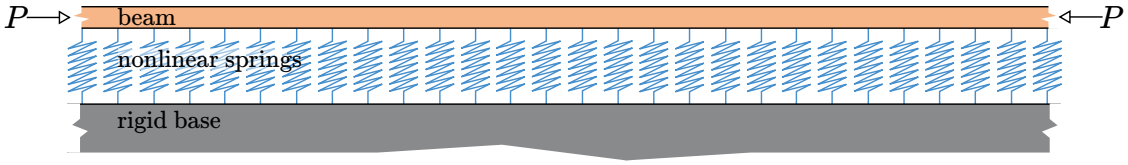


Figure 1.4: A cartoon of an infinite beam attached to a nonlinear Winkler foundation under uniaxial compression.

We wish to find non-trivial solutions of this equation (clearly $v \equiv 0$ is always a solution regardless of the values of P, κ_2 and κ_3) as the compressive force increases. First, let us apply the perturbation expansion

$$v(x) = \epsilon v^{(1)}(x) + \epsilon^2 v^{(2)}(x) + \epsilon^3 v^{(3)}(x) + O(\epsilon^4). \tag{1.41}$$

At first order, (1.40) becomes

$$\mathcal{L}[v^{(1)}] := \frac{\mathrm{d}^4 v^{(1)}}{\mathrm{d}x^4} + P\frac{\mathrm{d}^2 v^{(1)}}{\mathrm{d}x^2} + v^{(1)} = 0 \qquad x \in \mathbb{R} \tag{1.42}$$

This linear ODE has physically relevant solutions of the form

$$v^{(1)}(x) = ae^{ikx} + \bar{a}e^{-ikx} \tag{1.43}$$

where the wave number k satisfies

$$P = k^2 + k^{-2} \tag{1.44}$$

Thus, the minimal value of P for which non-trivial solutions can exist is $P_{cr} = 2$ (obtained at critical wave number $k_{cr} = 1$).

We now consider what happens when we increase the compressive force by a small increment from this critical point, writing

$$P = P_{cr} + \epsilon^2 P_1, \tag{1.45}$$

and attempt to solve the equation at higher orders. At second order, we obtain:

$$\mathcal{L}[v^{(2)}](x) = \kappa_2 \left(a \exp(ix) + \bar{a} \exp(-ix)\right)^2 \tag{1.46}$$

which we can solve to obtain (up to the addition of a constant multiple of v_1)

$$v^{(2)}(x) = \kappa_2 \left(\frac{1}{9} a^2 \exp(2ix) + \frac{1}{9}\bar{a}^2 \exp(-2ix) + 2a\bar{a}\right). \tag{1.47}$$

At third order, we obtain:

$$\begin{aligned}\mathcal{L}[v^{(3)}](x) = &\left(\frac{2}{9}\kappa_2^2 + \kappa_3\right) a^3 \exp(3ix) + \left(P_1 + \frac{38}{9}\kappa_2^2 a\bar{a} + 3\kappa_3 a\bar{a}\right) a \exp(ix) \\ &+ \left(\frac{2}{9}\kappa_2^2 + \kappa_3\right) \bar{a}^3 \exp(-3ix) + \left(P_1 + \frac{38}{9}\kappa_2^2 a\bar{a} + 3\kappa_3 a\bar{a}\right) \bar{a} \exp(-ix)\end{aligned} \tag{1.48}$$

Here, we finally see the effect of the increased compression on the system and we can now proceed to derive a relationship between the amplitude of our deformation a and the compressive force P. In order for the formal expansion (1.41) to be uniformly valid, we require that each $v^{(i)}$ is bounded in x. The $\exp(ix)$ and $\exp(-ix)$ terms in (1.48) are in the kernel of $\mathcal{L}$ and would therefore result in "secular" terms of the form $x \exp(ix)$ in a general solution of the ODE, violating our boundedness condition. Thus, the condition we require on a is the satisfaction of the "amplitude equation":

$$\left(P_1 + \frac{38}{9}\kappa_2^2 a\bar{a} + 3\kappa_3 a\bar{a}\right) a = 0 \tag{1.49}$$

Without loss of generality we can assume a to be real (allowing complex values only changes the phase of the oscillations), resulting in the following solutions of (1.49):

$$a = 0 \quad \text{and} \quad a = \pm\sqrt{\frac{-9P_1}{38\kappa_2^2 + 27\kappa_3}} \tag{1.50}$$

In particular, we can see that non-trivial solutions are only possible for values of $P < P_{cr}$. This is the desired *subcritical* bifurcation we were seeking. In chapter 4, we shall see how a similar amplitude relation arises in the study of the wrinkling instability and that its criticality behaviour changes type depending on the material properties of the system.

1.3.2 The finite element method

In traditional engineering contexts, there are many instances where experimental verification of a design or theory may be too costly or dangerous and direct mathematical analysis is intractable. The development of numerical methods such as the finite element method (backed by some key technological advances in computing) presented a "third way" in which quantitative information about some physical phenomenon could be discerned by means of the approximate solution of some equation(s) relating to it.

The key idea in most numerical methods is *discretisation*, the replacement of something continuous with something discrete that in some sense approximates the original object. In the case of the finite element method for the solution of linear elliptic partial differential equations, we begin by taking the *weak formulation* of the equation so that it is in the form

$$\text{find } u \in \boldsymbol{\Upsilon} \text{ such that } B[u, v] = l[v] \quad \forall v \in \boldsymbol{\Upsilon}, \tag{1.51}$$

where $\boldsymbol{\Upsilon}$ is an appropriate Banach space (prototypically a Sobolev space—see (Evans, 2010) for the necessary theoretical background), $B : \boldsymbol{\Upsilon} \times \boldsymbol{\Upsilon} \to \mathbb{R}$ is a coercive, continuous bilinear form and $l : \boldsymbol{\Upsilon} \to \mathbb{R}$ is a linear form. We then discretise the typically infinite dimensional function space $\boldsymbol{\Upsilon}$ by replacing it with a finite-dimensional subspace $\boldsymbol{\Upsilon}_h \subset \boldsymbol{\Upsilon}$—usually some set of piecewise polynomial functions with bounded degree. The discretised problem then reads

$$\text{find } u_h \in \boldsymbol{\Upsilon}_h \text{ such that } B[u_h, v_h] = l[v_h] \quad \forall v_h \in \boldsymbol{\Upsilon}_h, \tag{1.52}$$

where h is a parameter that determines the fineness of the discretisation. Denoting the basis elements of $\boldsymbol{\Upsilon}_h$ by ϕ_i ($i \in \{1, \dots N(h)\}$), u_h can be written as

$$u_h = \sum_{i=1}^{N(h)} U_i \phi_i, \tag{1.53}$$

for some unknown coefficients U_i. We can then rewrite (1.52) as

$$\text{find } (U_1 \dots U_{N(h)}) \in \mathbb{R}^{N(h)} \text{ such that } \sum_{i=1}^{N(h)} B[\phi_i, \phi_j] = l[\phi_j] \quad \forall j \in \{1, \dots N(h)\}, \tag{1.54}$$

which is simply a system of $N(h)$ linear equations that can be solved using linear algebra methods. In the case that the bilinear form B is symmetric, we can rewrite (1.51) as a minimisation problem in the following way:

$$\text{find } u \in \boldsymbol{\Upsilon} \text{ such that } I(u) \leq I(v) \quad \forall v \in \boldsymbol{\Upsilon}, \tag{1.55}$$

where $I(v) \coloneqq B(v, v)/2 - l(v)$. Note that we can rewrite (1.51) as

$$\mathcal{F}(u; v) \coloneqq I'(u)v = 0. \tag{1.56}$$

The corresponding discretised problem to (1.55) is

$$\text{find } u_h \in \boldsymbol{\Upsilon}_h \text{ such that } I(u_h) \leq I(v_h) \quad \forall v_h \in \boldsymbol{\Upsilon}_h. \tag{1.57}$$

This approach is often referred to as "energy minimisation", as the "energy" I often arises from a physical energy when solving many problems in physics. In such cases, the finite element approximation has an intuitive physical meaning: the finite element approximation $\mathbf{u}_h$ is the minimal energy solution in $\boldsymbol{\Upsilon}_h$. A modified version of Céa's Lemma tells us that the finite element approximation is optimal in the *energy norm* induced by B.

In order to apply the finite element method to nonlinear equations such as the equilibrium equations of elasticity, we require some modifications. The energy I is no longer necessarily quadratic in its argument, but we can still write an equation of the form (1.56) to describe our variational formulation—there is no longer a bilinear form B, but there $\mathcal{F}$ is still linear in the test function v. To

solve this nonlinear equation, we turn to the Newton-Kantorovich method, an iterative scheme based on the Taylor expansion

$$\mathcal{F}(u + \delta u; v) \approx \mathcal{F}(u; v) + \mathcal{F}_u(u; v)\delta u. \tag{1.58}$$

If we seek δu such that $\mathcal{F}(u + \delta u; v) = 0$, this approximate relation can be viewed as a linear equation in δu, which can then be solved by previously described methods. For a more thorough discussion on the precise assumptions required to make sense of this, refer to Farrell (2020).

There is an enormous body of theoretical work on the numerical analysis of the finite element method, much of which lies outside the scope of this document. Here, we will highlight a few important properties of the method and discuss the construction of certain finite element spaces relevant in the context of elasticity; we advise the interested reader to review Brenner and Scott (2008) for a much more thorough treatment.

The first important property we will consider is exactly in which sense we can say that the solution to the discretised problem can be said to be an approximation to the solution of the original problem. The answer to this question is given by the the following result.

Lemma 1.1 (Céa's Lemma)**.** *Let u be the solution to the variational problem* (1.51)*. The finite element approximation $u_h \in \boldsymbol{\Upsilon}_h$ of $u \in \boldsymbol{\Upsilon}$ given by the solution to the discretised problem* (1.52) *is the best fit to u in $\|\cdot\|_{\boldsymbol{\Upsilon}}$ up to a constant, i.e.:*

$$\|u - u_h\|_{\boldsymbol{\Upsilon}} \leq \frac{c_1}{c_0} \min_{v_h \in \boldsymbol{\Upsilon}_h} \|u - v_h\|_{\boldsymbol{\Upsilon}},$$

for some c_0, c_1 dependent only on B.

Proof. Brenner and Scott (2008) Theorem 2.8.1 □

This quasi-optimality lemma forms the basis of *error analysis* for the finite element method. Once a particular finite element space has been chosen, the minimisation problem on the right can be analysed to give the expected rate of convergence of u_h to u as $h \to 0$.

In order to construct a finite element space, first we must discretise our domain. We break up the domain into a collection of pairwise disjoint open sets K_i for which the union of their closures is equal to the closure of the domain. A common choice for such a subdivision in two dimensions (direct analogues exist in higher dimensions) is a *triangulation*, where each K_i is a triangle and no vertex of a triangle lies on the interior of any other triangle's edge. Given a single triangle K, the other two ingredients we require are a d-dimensional space of functions $\mathcal{P}$—say, the polynomials of degree at most q—and the *degrees of freedom* $\mathcal{N}$, a basis for the dual space $\mathcal{P}^*$. To given a concrete example, let us take K to be the triangle with vertices $(0,0)$, $(0,1)$ and $(1,0)$; $\mathcal{P} = \mathcal{P}_1$ (the linear polynomials on K) and $\mathcal{N} = \{N_1, N_2, N_3\}$ to be the evaluation maps at each of the vertices of K, i.e.

$$N_1(v) = v(0,0), \quad N_2(v) = v(0,1), \quad N_3(v) = v(1,0). \tag{1.59}$$

We can then specify any linear polynomial on K with the three numbers given by evaluation on the nodes of K, allowing us to build our global finite element approximation u_h locally on an element-by-element basis. If this is done in such a way that the global approximation is continuous, one obtains the CG_1 finite element (also known as the *degree 1 continuous Galerkin element* or *linear Lagrange element*) and if this continuity constraint is dropped, one obtains the DG_1 element (the *degree 1 discontinuous Galerkin element*). This construction can be extended to use higher degree polynomial functions by adding further evaluation points to the edges and interior of the triangle.

In order to solve problems in incompressible elasticity, we must be able to impose the nonlinear constraint of incompressibility $J = 1$. Thus, we must specify a finite element space for both the displacement and the Lagrange multiplier p used to impose the constraint. Such *mixed finite element problems* require somewhat careful numerical treatment, as we will now demonstrate. First, let us state the variational

form of the equilibrium equations of incompressible elasticity:

$$\begin{aligned}\int_{\mathcal{B}}\left[\frac{\partial W}{\partial \mathbf{F}}\left(\mathbf{1}+\frac{\partial \mathbf{u}}{\partial \mathbf{X}},\mathbf{X}\right)-p\,\mathrm{cof}\left(\mathbf{1}+\frac{\partial \mathbf{u}}{\partial \mathbf{X}}\right)\right]:\frac{\partial \mathbf{v}}{\partial \mathbf{X}}\,\mathrm{d}\mathbf{X}&\\ =\int_{\mathcal{B}}\rho_0\mathbf{b}_0\cdot\mathbf{v}\,\mathrm{d}\mathbf{X}+\int_{\Gamma_1}\mathbf{s}_0\cdot\mathbf{v}\,\mathrm{d}A\quad\forall\mathbf{v}\in\boldsymbol{\Upsilon},&\qquad(1.60)\\ \int_{\mathcal{B}}q\left[\det\left(\mathbf{1}+\frac{\partial \mathbf{u}}{\partial \mathbf{X}}\right)-1\right]\mathrm{d}\mathbf{X}=0\quad\forall q\in\boldsymbol{\Lambda},&\end{aligned}$$

where the function spaces are given by

$$\boldsymbol{\Upsilon}=\{\mathbf{v}\in H^1(\mathcal{B};\mathbb{R}^3):\mathbf{v}|_{\Gamma_0}=0\},\quad \boldsymbol{\Lambda}=L^2(\mathcal{B},\mathbb{R}).\qquad(1.61)$$

It can be shown (see Le Tallec (1994) for the full details) that in order for a finite element discretisation of (1.60) to be well-posed, the solution $\mathbf{u}_h$ and the finite element spaces $\boldsymbol{\Upsilon}_h$ and $\boldsymbol{\Lambda}_h$ must satisfy the following *inf-sup condition*:

$$\inf_{\substack{q_h\in\boldsymbol{\Lambda}_h\\ \|q_h\|=1}}\sup_{\substack{\mathbf{v}_h\in\boldsymbol{\Upsilon}_h\\ \|\mathbf{v}_h\|=1}}\int_{\mathcal{B}}q_h\,\mathrm{cof}\left(\mathbf{1}+\frac{\partial \mathbf{u}_h}{\partial \mathbf{X}}\right):\frac{\partial \mathbf{v}_h}{\partial \mathbf{X}}\,\mathrm{d}\mathbf{X}=c_0>0,\qquad(1.62)$$

where c_0 depends only on h. This is extremely difficult to verify directly, but it can be shown that element spaces that satisfy a constraint of the same type for the Stokes problem will also satisfy (1.62) for incompressible hyperelasticity under certain conditions (see Braess and Ming (2005)). A detailed exposition of the numerical analysis of the Stokes problem and other mixed finite element problems can be found in Boffi, Brezzi, and Fortin (2013). A popular choice of stable element pair for such problems in two dimensions is the generalised Taylor-Hood element $(CG_k)^2\times CG_{k-1}$ for $k\geq 2$ (Taylor and Hood, 1973), but we will make use of the Scott-Vogelius element $(CG_k)^2\times DG_{k-1}$ (Scott and Vogelius, 1985). In general, this is only stable for $k\geq 4$, which requires a prohibitively high number of degrees of freedom, but it can be shown (Olshanskii and Rebholz, 2011) that a particular choice of triangulation can make this element stable in two dimensions for $k\geq 2$.

1.4 Contribution

This thesis makes a number of contributions:

- The presentation of a stream function based framework for the study of the wrinkling instability in elastic bilayers for problems involving growth, compression or a combination of the two.

- The consideration of the effect of a number of physical effects to the incidence of the wrinkling instability, namely the contributions of added surface tension, pressure, fibres, or the presence of an additional top layer. The stiff film asymptotic limit is computed where tractable and we identify whether the system supports a Biot-type or Euler-type instability for sufficiently soft films.

- An extension of the linear analysis to the post-buckling regime to compute an amplitude relation for the growth case including a mode amplitude that can vary over far spatial and slow temporal scales. This gives the stiffness ratio threshold at which the wrinkling bifurcation changes from supercritical to subcritical.

- A numerical bifurcation analysis of the problem of a growing neo-Hookean film on a neo-Hookean substrate using the deflated continuation algorithm. We show excellent agreement with the analytically derived amplitude equation with no fitting parameters.

- Discretisation and solution of the Moore-Spence system for the bilayer problem for direct numerical computation of the critical growth value in the discretised system. We characterise the effect of implementation details such as domain width on the bifurcation behaviour of the system.

- Exploration of the solution set of the amplitude equation, a nonlinear Klein-Gordon type equation. We identify the parameter regimes where localised solutions are possible in the subcritical case.

- Identification of secondary bifurcations in the numerical bifurcation analysis of the bilayer problem that correspond to phenomena seen in physical experiments and may direct analytical studies in future works.

Most of the material in this thesis has already been published in the following journal articles, which form the basis of the text in this thesis:

- H. Alawiye, E. Kuhl, and A. Goriely. *Revisiting the wrinkling of elastic bilayers I: linear analysis.* Philosophical Transactions of the Royal Society A, 377:20180076, 2019.
- H. Alawiye, P. E. Farrell, and A. Goriely. *Revisiting the wrinkling of elastic bilayers II: post-bifurcation analysis.* Journal of the Mechanics and Physics of Solids, 143:104053, 2020

1.5 Notation

A list of commonly used notation is given in table 1.1. Occasionally, one of the symbols in the table is used with a different meaning (often with a subscript, as a subscript or with a diacritic); this is clarified wherever it occurs.

Table 1.1: Index of frequently used symbols

Symbol	Name
$\mathbf{A}$	Elastic deformation gradient
$\mathcal{B}$	Domain
$\mathscr{C}$	Coefficient of amplitude relation
$\mathbf{F}$	Deformation gradient
$\mathbf{G}$	Growth tensor
I	Total energy functional
J	Volume ratio (Jacobian determinant)
L	Domain length
$\mathbf{M}$	Solvability matrix
$\mathbf{N}$	Surface normal vector (reference configuration)
O	Big O (Bachmann-Landau notation)
$\mathbf{T}$	Cauchy stress tensor
$\mathbf{T}_0$	First Piola-Kirchhof stress tensor
W	Stored energy density
$\mathbf{X}$	Reference coordinate vector
X	Reference coordinate (1st direction)
Y	Reference coordinate (2nd direction)
a	Amplitude
c_i	Arbitrary constant
e_i	Root of equation

Symbol	Name
f	Function
f	Of the film (as subscript)
g	Growth ratio
h	Profile function
k	Wavenumber
$\mathbf{n}$	Surface normal vector (deformed configuration)
p	Pressure (Lagrange multiplier)
s	Of the substrate (as subscript)
t	Time
$\mathbf{u}$	Displacement vector
u	Displacement in 1st direction
v	Displacement in 2nd direction
$\mathbf{x}$	Deformed coordinate vector
x	Deformed coordinate (1st direction)
y	Deformed coordinate (2nd direction)
Ψ	Stream function
β	Stiffness ratio
γ	Growth ratio in film
δ	Small increment
ϵ	Small parameter
ζ	Far spatial variable
λ	Compression ratio
μ	Shear modulus
ρ	Density
τ	Slow temporal variable

This chapter is derived from Alawiye, Kuhl, and Goriely (2019).

2 The model

Contents

2.1 General formulation 27
2.2 Growth and compression 28
2.3 Mixed coordinate formulation 30
2.4 Boundary conditions 32

2.1 General formulation

The basis of our computations is a three-dimensional formulation similar to those presented in Ben Amar and Bordner (2017) and Holland et al. (2017). We can substantially simplify the problem by only considering two-dimensional deformations, which is achieved by assuming that the material is in *plane strain*—that there is both no displacement in the transverse dimension and no dependence of the other components of the displacement on the spatial coordinate in that dimension.

We consider the following model, illustrated in fig. 2.1: let the region $\mathcal{B}_\mathrm{s}$ represent the initial unstressed infinite elastic substrate and $\mathcal{B}_\mathrm{f}$ be an elastic film bonded to its upper surface. Together, these form the domain $\mathcal{B} = \mathcal{B}_\mathrm{f} \cup \mathcal{B}_\mathrm{s}$. Let μ_s and μ_f represent the shear moduli of their respective layers, $\beta = \mu_\mathrm{f}/\mu_\mathrm{s}$ be their ratio and $\mathbf{X}$ be a coordinate system across the two layers in the reference configuration. Let

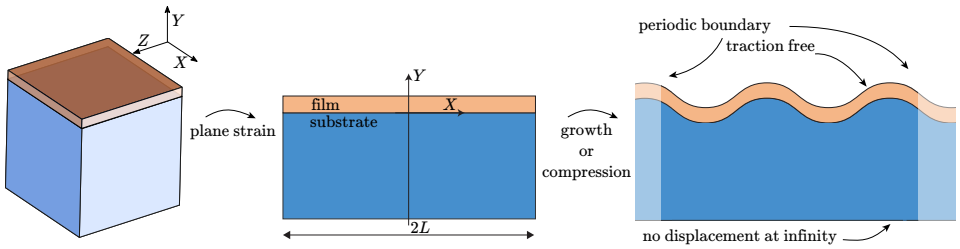


Figure 2.1: Geometry of the domain. The system is composed of a bilayer with an infinitely deep layer of width $2L$ bonded by a film of thickness 1. Considering only plane strain, the problem is reduced to the deformation of a two-dimensional system under either compression or growth causing wrinkling. The boundary conditions are: continuity of traction and displacement between the layers, traction free upper layer, no displacement at $Y = -\infty$ and horizontal periodicity.

us henceforth fix our domains as $\mathcal{B}_\mathrm{f} = [-L, L] \times (0, 1]$ (taking the thickness of the film to be 1 without loss of generality) and $\mathcal{B}_\mathrm{s} = [-L, L] \times (-\infty, 0]$ for some fixed $L > 0$ to be determined. After a static deformation, the new material coordinates of the deformed configuration are given by $\mathbf{x}(\mathbf{X})$ with deformation gradient

$$\mathbf{F} = \frac{\partial \mathbf{x}}{\partial \mathbf{X}}. \tag{2.1}$$

We consider the two extreme cases that we label *growth* and *compression*.

2.2 Growth and compression

The fundamental assumption which allows us to incorporate material growth into the framework of elasticity comes from the theory of morphoelasticity, as described earlier. We assume that any residual stresses within the material in the absence of applied loads are the result of growth on a local level and hence that we can decompose the deformation gradient multiplicatively as in (1.38). The application of the growth tensor alone to the reference configuration may not produce a physically realisable body, but the following application of the elastic tensor introduces stresses that enforce the boundary conditions and remove unphysical phenomena such as self-intersection.

For a hyperelastic material, with elastic strain-energy density function W, we can define an augmented energy density functional for the composed deformation by

$$\overline{W}(\mathbf{F}, \mathbf{G}) = (\det \mathbf{G}) W(\mathbf{F}\mathbf{G}^{-1}) - p\left(\det(\mathbf{F}\mathbf{G}^{-1}) - 1\right). \tag{2.2}$$

Here, p is a Lagrange multiplier that imposes the incompressibilty constraint. In the particular case of a neo-Hookean material that we use here, the strain-energy density of an elastic deformation is given by

$$W(\mathbf{A}) = \frac{\mu}{2}(\operatorname{tr} \mathbf{A}\mathbf{A}^\top - 3). \tag{2.3}$$

Let $\boldsymbol{\Xi}$ be the set of *admissible elastic deformations*—those deformations with sufficient regularity for (2.2) to be integrable. For a fixed growth tensor $\mathbf{G}$ we can write the elastic deformation tensor $\mathbf{A}$ induced by any $\mathbf{x} \in \boldsymbol{\Xi}$ as

$$\mathbf{A} = \mathbf{F}\mathbf{G}^{-1} = \frac{\partial \mathbf{x}}{\partial \mathbf{X}}\mathbf{G}^{-1}. \tag{2.4}$$

We can also consider an additional lateral compression in addition to or in place of growth in our system. As with growth, we can specify an initial diagonal stretch tensor $\mathbf{A}_0$ to prescribe the external stretches that are applied to the bilayer. Since no new material is generated in this process, we must have $\det \mathbf{A}_0 = 1$. Our multiplicative decomposition is now

$$\mathbf{F} = \mathbf{A}\mathbf{A}_0\mathbf{G}. \tag{2.5}$$

Since $\mathbf{A}_0$ represents an elastic process, our energy density functional (2.2) is unchanged. Indeed, we only separate it from $\mathbf{A}$ for notational convenience.

We will study initial, stretch tensors $\mathbf{A}_0$ given by

$$\mathbf{A}_0 = \begin{pmatrix} \lambda & 0 \\ 0 & \lambda^{-1} \end{pmatrix}, \tag{2.6}$$

and a growth tensor $\mathbf{G}$ satisfying $\det \mathbf{G} = J$. In our case, we fix $\mathbf{G} = g\mathbf{I}$, where

$$g(\mathbf{X}) = \begin{cases} \gamma & \mathbf{X} \in \mathcal{B}_\mathrm{f} \\ 1 & \mathbf{X} \in \mathcal{B}_\mathrm{s} \end{cases}. \tag{2.7}$$

We then have $J = g^2$. In our study, we will specialise to the compression-only case by taking $J = 1$.

We can now specify our mathematical problem. We look for deformations $\mathbf{x}$ that are local minimisers of the total elastic energy of our system, subject to

the elastic incompressibility constraint $\det \mathbf{A} = 1$. More explicitly, given $\mathbf{G}$ and $\mathbf{A}_0$, our variational problem is

$$\underset{\substack{\mathbf{x}\in\boldsymbol{\Xi}\\ p\in\boldsymbol{\Lambda}}}{\text{minimise}} \quad I(\mathbf{x},p) \coloneqq \int_{\mathcal{B}} (\frac{\mu}{2}\det\mathbf{G})\left(\operatorname{tr}\left(\mathbf{A}\mathbf{A}^{\top}\mathbf{A}_0^2\right)-3\right) - p(\det\mathbf{A}-1)\,\mathrm{d}\mathbf{X}, \tag{2.8}$$

where $\boldsymbol{\Lambda}$ is a suitable Lagrange multiplier space that allows us to impose the pointwise constraint on $\mathbf{A}$. The Euler-Lagrange equation for this system yields a necessary condition on minimisers of the energy.

2.3 Mixed coordinate formulation

Taking advantage of the two-dimensional nature of the problem, we can make use of a technical tool to automatically satisfy the elastic incompressibility constraint. Essentially, we can find a *stream function* for the deformation, which is named after a similar construction used for the 2D Stokes flow. The difference here is that the domain of the stream function is a *mixed coordinate space*—it is a function of coordinates in both the reference and deformed configurations. The idea was first proposed in this setting by Rooney and Carroll (1984) and used in Ben Amar and Ciarletta (2010) and Ben Amar and Bordner (2017).

Let $\mathbf{x}(\mathbf{X}) = (x(X,Y), y(X,Y))$ be any two-dimensional deformation for which

$$\det\mathbf{F} = \frac{\partial x}{\partial X}\frac{\partial y}{\partial Y} - \frac{\partial x}{\partial Y}\frac{\partial y}{\partial X} \equiv J, \tag{2.9}$$

where J is piecewise constant in each subdomain of $\mathcal{B}$. More general growth conditions can be incorporated into this formulation, but for simplicity we will only study the constant case. Any such $\mathbf{F}$ can be decomposed multiplicatively as in (1.38) into an incompressible elastic deformation tensor $\mathbf{A}$. Away from some pathological cases, we can use an implicit function theorem based argument to define a function Ψ on the mixed coordinates (x,Y) such that

$$X = \frac{1}{J\lambda}\frac{\partial\Psi}{\partial Y}(x,Y) \quad \text{and} \quad y = \frac{1}{\lambda}\frac{\partial\Psi}{\partial x}(x,Y). \tag{2.10}$$

From these representations, we can also compute the partial derivatives found in $\mathbf{F} = \frac{\partial \mathbf{x}}{\partial \mathbf{X}}$ to rewrite the deformation gradient as

$$\mathbf{F} = \frac{1}{\partial_{xY}\Psi} \begin{pmatrix} J\lambda & -\partial_{YY}\Psi \\ J\partial_{xx}\Psi & \lambda^{-1}\left((\partial_{xY}\Psi)^2 - \partial_{YY}\Psi\partial_{xx}\Psi\right) \end{pmatrix}. \tag{2.11}$$

Explicitly computing the determinant of $\mathbf{F}$, we find

$$\det \mathbf{F} = \frac{1}{(\partial_{xY}\Psi)^2}\left[J\left((\partial_{xY}\Psi)^2 - \partial_{YY}\Psi\partial_{xx}\Psi\right) + J\partial_{xx}\Psi\partial_{YY}\Psi\right] = J, \tag{2.12}$$

hence the determinant constraint (2.9) is automatically satisfied exactly. To translate our energy functional into this stream function formulation, we make the change of integration variables

$$\mathrm{d}x\mathrm{d}Y = \frac{\partial x}{\partial X}\mathrm{d}X\mathrm{d}Y = \frac{J\lambda}{\partial_{xY}\Psi}\mathrm{d}X\mathrm{d}Y. \tag{2.13}$$

Since $\det \mathbf{A} = 1$ by construction, the Lagrange multiplier term in (2.8) disappears and leaves us with the minimisation problem

$$\begin{aligned} \underset{\Psi\in\boldsymbol{\Phi}}{\text{minimise}} \quad \tilde{I}(\Psi) \coloneqq \int_{\tilde{\mathcal{B}}} \frac{\mu}{2J\lambda^3\partial_{xY}\Psi}\Big[&-2J\lambda^2(\partial_{xY}\Psi)^2 + \\ &+ (\partial_{xY}\Psi)^4 - 2\partial_{YY}\Psi(\partial_{xY}\Psi)^2\partial_{xx}\Psi + J^2\lambda^2\left(\lambda^2 + (\partial_{xx}\Psi)^2\right) + \\ &+(\partial_{YY}\Psi)^2\left(\lambda^2 + (\partial_{xx}\Psi)^2\right)\Big]\,\mathrm{d}x\mathrm{d}Y, \end{aligned} \tag{2.14}$$

where $\tilde{\mathcal{B}}$ is the mixed coordinate configuration of the domain $\mathcal{B}$ and $\boldsymbol{\Phi}$ is the set of stream functions that produce admissible deformations.

To obtain the Euler-Lagrange equation of (2.14) and its boundary conditions explicitly, we must compute the first variation of its integral functional $\tilde{I}$. For notational simplicity, we rewrite $\tilde{I}$ as

$$\tilde{I}(\Psi) = \int_{\tilde{\mathcal{B}}} f(\partial_{xx}\Psi, \partial_{xY}\Psi, \partial_{YY}\Psi)\,\mathrm{d}x\mathrm{d}Y. \tag{2.15}$$

The Euler-Lagrange equations for the system are then given by

$$\begin{aligned} \frac{\partial^2}{\partial x^2}\left(\frac{\partial f}{\partial(\partial_{xx}\Psi_{\mathrm{f}})}\right) + \frac{\partial^2}{\partial x\partial Y}\left(\frac{\partial f}{\partial(\partial_{xY}\Psi_{\mathrm{f}})}\right) + \frac{\partial^2}{\partial Y^2}\left(\frac{\partial f}{\partial(\partial_{YY}\Psi_{\mathrm{f}})}\right) = 0, \\ \frac{\partial^2}{\partial x^2}\left(\frac{\partial f}{\partial(\partial_{xx}\Psi_{\mathrm{s}})}\right) + \frac{\partial^2}{\partial x\partial Y}\left(\frac{\partial f}{\partial(\partial_{xY}\Psi_{\mathrm{s}})}\right) + \frac{\partial^2}{\partial Y^2}\left(\frac{\partial f}{\partial(\partial_{YY}\Psi_{\mathrm{s}})}\right) = 0 \end{aligned}. \tag{2.16}$$

2.4 Boundary conditions

The physical constraints we impose on the system at the boundaries are illustrated in fig. 2.1. We impose that all displacements in the substrate vanish at infinity, that the displacements are x-periodic and that the upper surface of the film is traction free. We define separate stream functions Ψ_f and Ψ_s for each layer of the system and we seek to simultaneously solve for the energy-minimising stream function of each layer. The problems for each layer are coupled by the introduction of boundary conditions at the layer interfaces that impose continuity of traction and displacement between layers.

From the physical condition that the two layers can not detach from one another, we obtain, at $Y = 0$:

$$\frac{\partial \Psi_\mathrm{f}}{\partial x} = \frac{\partial \Psi_\mathrm{s}}{\partial x}, \tag{2.17a}$$

$$\frac{\partial \Psi_\mathrm{f}}{\partial Y} = \gamma^2 \frac{\partial \Psi_\mathrm{s}}{\partial Y}. \tag{2.17b}$$

From repeated integration by parts in our calculation of the first variation, we obtain additional natural boundary conditions at the interface ($Y = 0$), representing the physical conditions on the continuity of traction:

$$\frac{\partial}{\partial Y}\left(\frac{\partial f}{\partial(\partial_{YY}\Psi_\mathrm{f})}\right) + \frac{\partial}{\partial x}\left(\frac{\partial f}{\partial(\partial_{xY}\Psi_\mathrm{f})}\right) = \frac{\partial}{\partial Y}\left(\frac{\partial f}{\partial(\partial_{YY}\Psi_\mathrm{s})}\right) + \frac{\partial}{\partial x}\left(\frac{\partial f}{\partial(\partial_{xY}\Psi_\mathrm{s})}\right), \tag{2.18a}$$

$$\gamma^2 \frac{\partial f}{\partial(\partial_{YY}\Psi_\mathrm{f})} = \frac{\partial f}{\partial(\partial_{YY}\Psi_\mathrm{s})}. \tag{2.18b}$$

On the top of the film ($Y = 1$), we obtain the traction-free conditions through the same process:

$$\frac{\partial}{\partial Y}\left(\frac{\partial f}{\partial(\partial_{YY}\Psi_\mathrm{f})}\right) + \frac{\partial}{\partial x}\left(\frac{\partial f}{\partial(\partial_{xY}\Psi_\mathrm{f})}\right) = 0, \tag{2.19a}$$

$$\frac{\partial f}{\partial(\partial_{YY}\Psi_\mathrm{f})} = 0. \tag{2.19b}$$

Finally, we impose the decay conditions

$$\lim_{Y\to-\infty} \partial_x \Psi_\mathrm{s} - Y = 0, \tag{2.20a}$$

$$\lim_{Y\to-\infty} \partial_Y \Psi_\mathrm{s} - x = 0. \tag{2.20b}$$

The two fourth-order PDEs for Ψ_{f} and Ψ_{s} in (2.16), the x-periodicity condition and the eight boundary conditions given by (2.17)–(2.20) form the full Euler-Lagrange system. It should be noted that the explicit form of these Euler-Lagrange equations and their boundary conditions are lengthy with significant nonlinearity, making their direct solution impossible through analytic means.

This chapter is derived from Alawiye, Kuhl, and Goriely (2019).

3 Linear analysis

Contents

3.1 Perturbation 35
3.2 Bifurcation analysis 37
3.2.1 Compression case 37
3.2.2 Growth case 39
3.3 Generalisations 42
3.3.1 Bilayer with surface tension 42
3.3.2 Bilayer with upper substrate 47
3.3.3 Pressure 50
3.3.4 Fibre-reinforced substrate 52
3.4 Conclusions 54

3.1 Perturbation

Despite the difficulties that a complete characterisation of solutions to this problem presents, it is easy to see that the homogeneous growth solution given by

$$\mathbf{x}^{(0)}(X,Y) = \begin{cases} (\lambda X, \gamma^2\lambda^{-1}Y) & (X,Y) \in \mathcal{B}_{\mathrm{f}}, \\ (\lambda X, \lambda^{-1}Y) & (X,Y) \in \mathcal{B}_{\mathrm{s}}, \end{cases} \tag{3.1}$$

with corresponding stream functions

$$\begin{aligned} \Psi_{\mathrm{f}}^{(0)}(x,Y) &= \gamma^2 xY \qquad\qquad Y \in (0,1], \\ \Psi_{\mathrm{s}}^{(0)}(x,Y) &= xY \qquad\qquad Y \in (-\infty,0], \end{aligned} \tag{3.2}$$

is a solution of (2.16). Consider a perturbation of the form $\Psi = \Psi^{(0)} + \epsilon\Psi^{(1)}$, where ϵ is a small positive parameter. To linear order in ϵ, the Euler-Lagrange equations for the system read

$$\begin{aligned}\lambda^2\frac{\partial^4\Psi_{\mathrm{f}}^{(1)}}{\partial Y^4} + (\gamma^4+\lambda^4)\frac{\partial^4\Psi_{\mathrm{f}}^{(1)}}{\partial x^2\partial Y^2} + \gamma^4\lambda^2\frac{\partial^4\Psi_{\mathrm{f}}^{(1)}}{\partial x^4} = 0,\\ \lambda^2\frac{\partial^4\Psi_{\mathrm{s}}^{(1)}}{\partial Y^4} + (1+\lambda^4)\frac{\partial^4\Psi_{\mathrm{s}}^{(1)}}{\partial x^2\partial Y^2} + \lambda^2\frac{\partial^4\Psi_{\mathrm{s}}^{(1)}}{\partial x^4} = 0,\end{aligned} \tag{3.3}$$

with boundary conditions given explicitly in Appendix A. Assuming a periodic decomposition of the form $\Psi^{(1)}(x,Y) = \sin(kx)h^{(1)}(Y)$ for some $k > 0$, we arrive at the ODEs

$$\begin{aligned}\lambda^2\frac{\mathrm{d}^4h_{\mathrm{f}}^{(1)}}{\mathrm{d}Y^4} - k^2(\gamma^4+\lambda^4)\frac{\mathrm{d}^2h_{\mathrm{f}}^{(1)}}{\mathrm{d}Y^2} + \gamma^4k^4\lambda^2h_{\mathrm{f}}^{(1)} = 0,\\ \lambda^2\frac{\mathrm{d}^4h_{\mathrm{s}}^{(1)}}{\mathrm{d}Y^4} - k^2(1+\lambda^4)\frac{\mathrm{d}^2h_{\mathrm{s}}^{(1)}}{\mathrm{d}Y^2} + k^4\lambda^2h_{\mathrm{s}}^{(1)} = 0,\end{aligned} \tag{3.4}$$

with boundary conditions given in Appendix A. Solving (3.4) with the decay conditions at $Y \to \infty$ (A.2g-A.2h), we obtain the general solutions

$$\begin{aligned}h_{\mathrm{f}}^{(1)}(Y) &= c_1e^{-k\gamma^2Y} + c_2e^{k\gamma^2Y} + c_3e^{-kY} + c_4e^{kY},\\ h_{\mathrm{s}}^{(1)}(Y) &= c_5e^{kY} + c_6Ye^{kY},\end{aligned} \tag{3.5}$$

in the case $\lambda = 1$,

$$\begin{aligned}h_{\mathrm{f}}^{(1)}(Y) &= c_1e^{-k\lambda Y} + c_2Ye^{-k\lambda Y} + c_3e^{k\lambda Y} + c_4Ye^{k\lambda Y},\\ h_{\mathrm{s}}^{(1)}(Y) &= c_5e^{k\lambda^{-1}Y} + c_6e^{k\lambda Y},\end{aligned} \tag{3.6}$$

in the case $\lambda = \gamma$ and

$$\begin{aligned}h_{\mathrm{f}}^{(1)}(Y) &= c_1e^{-k\gamma^2\lambda^{-1}Y} + c_2e^{k\gamma^2\lambda^{-1}Y} + c_3e^{-k\lambda Y} + c_4e^{k\lambda Y},\\ h_{\mathrm{s}}^{(1)}(Y) &= c_5e^{k\lambda^{-1}Y} + c_6e^{k\lambda Y},\end{aligned} \tag{3.7}$$

otherwise. Substituting these expressions into our boundary conditions, we obtain a homogeneous system of six linear equations in the six unknown coefficients $\mathbf{c} \coloneqq \{c_i\}_{i=1}^6$ that can be abbreviated as

$$\mathbf{M}(k,\gamma,\beta)\mathbf{c} = \mathbf{0}, \tag{3.8}$$

where $\mathbf{M}$ is a 6×6 matrix. This system will only have nontrivial solutions if

$$\det\mathbf{M} = 0, \tag{3.9}$$

thus giving us a solvability condition for our system.

3.2 Bifurcation analysis

We now focus our attention on two specific cases: a bilayer that is compressed unilaterally but experiences no growth and a bilayer that is under no compression but has a growing upper layer. The determinant of $\mathbf{M}$ is sufficiently complex that its zero level set cannot be obtained in closed form. However, they can be obtained asymptotically for short and long wavelengths and solved numerically in the intermediate regime.

3.2.1 Compression case

In the case of pure compression, we set $\gamma = 1$ and consider λ as our bifurcation parameter. The determinant of $\mathbf{M}$ can be written in the form

$$\det \mathbf{M}(k, \lambda, \beta) = \frac{1}{\lambda^7} \sum_{i=0}^{4} p_i(k, \lambda, \beta) e^{k\zeta_i}, \tag{3.10}$$

where each p_i is a polynomial in its arguments and $(\zeta_i)_{i=0}^4 = (0, \lambda^{-1} + \lambda, -\lambda^{-1} + \lambda, \lambda^{-1} - \lambda, -\lambda^{-1} - \lambda)$. For large values of k, $\exp(k\zeta_1)$ is the dominant term, and thus p_1 must vanish in order for the determinant to vanish in that limit. This polynomial—which has total degree 34—vanishes whenever λ is equal to either a particular root of the equation

$$\lambda^3 + \lambda^2 + \lambda - 1 = 0, \tag{3.11}$$

given by

$$\lambda_{\text{biot}} = \frac{1}{3}\left((17 + 3\sqrt{33})^{\frac{1}{3}} - \frac{2}{(17 + 3\sqrt{33})^{\frac{1}{3}}} - 1\right) \approx 0.543689, \tag{3.12}$$

or a particular root $\lambda_*(\beta)$ of a polynomial given by the equation

$$\begin{cases} (1+\beta)\lambda^3 + (1-\beta)\lambda^2 + (1+\beta)\lambda - 1 + \beta = 0 & \text{if} \quad \beta < 1, \\ (1+\beta)\lambda^3 - (1-\beta)\lambda^2 + (1+\beta)\lambda + 1 - \beta = 0 & \text{if} \quad \beta > 1. \end{cases} \tag{3.13}$$

The root in question is not present in the case $\beta = 1$ (this is in fact the classical Biot instability of an elastic half space as the two layers can no longer be distinguished), but when it exists, it is always strictly less than λ_{biot}. Thus, λ_{biot} provides a

lower bound for the critical compression ratio required to cause the emergence of nontrivial solutions.

To better understand the solution set, we can solve the determinant relation numerically. We can fix a stiffness ratio β and find the compression ratio λ as a function of the wavenumber k. An example of such a *dispersion curve* is shown in fig. 3.1 for the particular value $\beta = 10$.

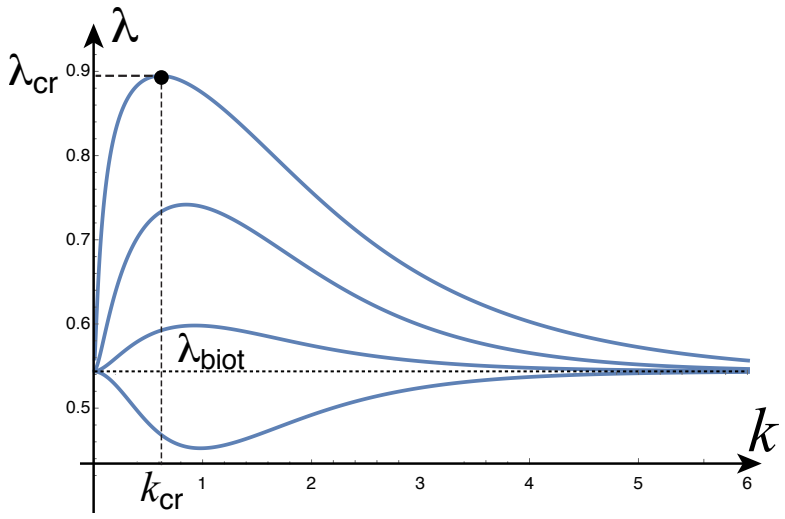


Figure 3.1: The maxima of the dispersion curves of $\det(\mathbf{M}) = 0$ in the λ-k plane provide the first critical values of λ at which oscillatory solutions can be obtained. For instance, the critical compression λ_{cr} and wavenumber k_{cr} are indicated for the top curve. The curves from top to bottom are obtained for decreasing values of β. The bottom curve is obtained for a value of $\beta < 1$.

From this, we can deduce that if we were to gradually decrease the compression ratio λ from 1, we would expect to see nontrivial periodic solutions emerging at $\lambda_{\text{cr}} \approx 0.89$ with wavenumber $k_{\text{cr}} \approx 0.61$. We can repeat this process and track the position of this critical point as we vary the value of β, as shown in fig. 3.2.

As β decreases towards 1, λ_{cr} approaches λ_{biot}. For values of β infinitesimally above 1, a finite wavenumber $k \approx 0.941$ is selected, but at $\beta = 1$, all wavenumbers are possible. For $\beta < 1$, we see the reappearance of a critical point, but it is in fact a local minimum rather than a local maximum. Hence, surface instability appears first for all values of $\beta < 1$.

For large values of β corresponding to a stiff film on a soft substrate, the selected wavenumber becomes vanishingly small and the critical compression

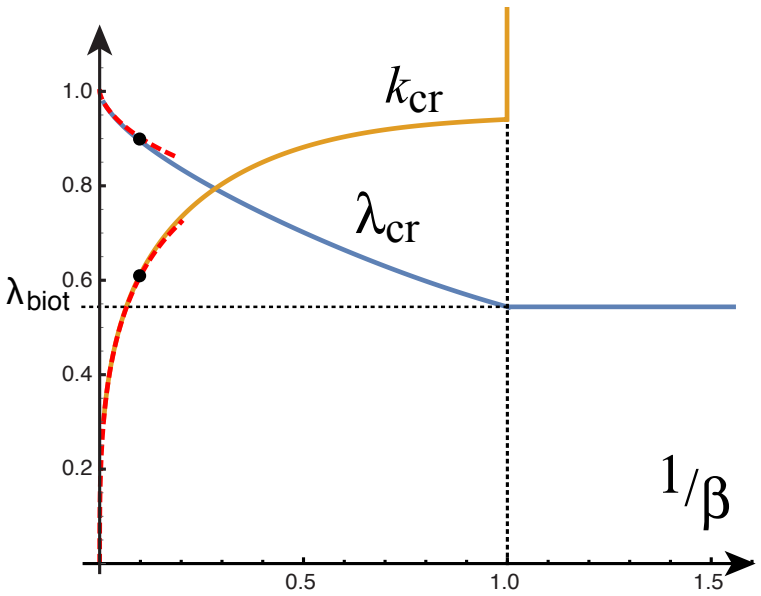


Figure 3.2: The critical wavenumber k_{cr} and compression λ_{cr} as functions of β^{-1}. The two points on the curves correspond to the critical values found for $\beta = 10$. For $\beta < 1$, the critical compression is given by the Biot value and $k_{\mathrm{cr}} \to \infty$. The asymptotic estimates provide good approximations of these curves up to $\beta \approx 20$ (red/dashed). Please note that the vertical axis in this figure and similar figures found later in this document represents *both* the wavenumber and the compression as indicated by the curve labels.

ratio on an infinite domain approaches 1, corresponding to the Euler buckling instability. A standard asymptotic analysis reveals the following approximations (illustrated in fig. 3.2):

$$\lambda_{\mathrm{cr}} = 1 - \frac{3^{2/3}}{4}\beta^{-2/3} + \frac{33 \cdot 3^{1/3}}{160}\beta^{-4/3} - \frac{3^{2/3}}{8}\beta^{-5/3} - \frac{7629}{22400}\beta^{-2} + \frac{39 \cdot 3^{1/3}}{160}\beta^{-7/3} + \frac{3302617}{5376000 \cdot 3^{1/3}}\beta^{-8/3} + O(\beta^{-3}), \tag{3.14}$$

$$k_{\mathrm{cr}} = 3^{1/3}\beta^{-1/3} - \frac{3}{5}\beta^{-1} + \frac{463 \cdot 3^{2/3}}{5600}\beta^{-5/3} + \frac{3217}{33600 \cdot 3^{2/3}}\beta^{-7/3} + O(\beta^{-8/3}). \tag{3.15}$$

We recover the well-known dependence for the wavelength with a $\beta^{1/3}$ scaling that was already established by Biot (Biot, 1937) and has been recovered numerous times since then (see Sun et al. (2012), for example).

3.2.2 Growth case

The growth case displays many similarities to the compression case. Considering large values of k once more reveals the existence of a Biot-type wrinkling instability

for the system as described in section 1.1. As before, the determinant can be written in the form

$$\det \mathbf{M}(k, \gamma, \beta) = \frac{1}{\gamma^3} \sum_{i=0}^{4} p_i(k, \gamma, \beta) e^{k\zeta_i}, \tag{3.16}$$

where each p_i is a polynomial in its arguments and $(\zeta_i)_{i=0}^4 = (0, 1+\gamma^2, -1+\gamma^2, -1-\gamma^2, 1-\gamma^2)$. For large enough k, $\exp(k\zeta_1)$ is the dominant term and hence in order for the determinant to vanish in that limit, p_1 must vanish. We find that polynomial p_1 vanishes whenever γ is equal to either a particular root of the equation

$$\gamma^3 - \gamma^2 - \gamma - 1 = 0, \tag{3.17}$$

given by

$$\gamma_{\text{biot}} = \frac{1}{\lambda_{\text{biot}}} = \frac{1}{3}\left(1 + \left(19 - 3\sqrt{33}\right)^{\frac{1}{3}} + \left(19 + 3\sqrt{33}\right)^{\frac{1}{3}}\right) \approx 1.83929, \tag{3.18}$$

or a particular root $\gamma_*(\beta)$ of the equation

$$\beta^2\gamma^6 - (3\beta^2 + 2\beta)\gamma^4 - (\beta^2 + 4\beta + 4)\gamma^2 - (\beta^2 + 2\beta) = 0. \tag{3.19}$$

Further examination reveals that we have $\gamma_*(\beta) > \gamma_{\text{biot}}$ for all values of $\beta > 0$. Thus, γ_{biot} provides an upper bound on the critical growth factor required in order to achieve nontrivial periodic solutions.

Solving the determinant relation numerically once more, we can fix a stiffness ratio β and find the growth factor γ as a function of the wavenumber k. An example of such a dispersion relation is shown in fig. 3.3 for the particular value $\beta = 3$.

In a thought experiment where we gradually increase the growth factor γ from 1, we expect to see nontrivial periodic solutions emerging at γ_{cr}. As before, by repeating this process, we can track the position of this critical point as we vary the value of β, as shown in fig. 3.4.

As β decreases, γ_{cr} approaches γ_{biot} and we see that the value of k_{cr} increases without bound, demonstrating the aforementioned instability. The value of $\beta = \beta_{\text{min}}$ at which the wavenumber first diverges can be found exactly (but is not given explicitly here) and is $\beta_{\text{min}} \approx 1.90379$.

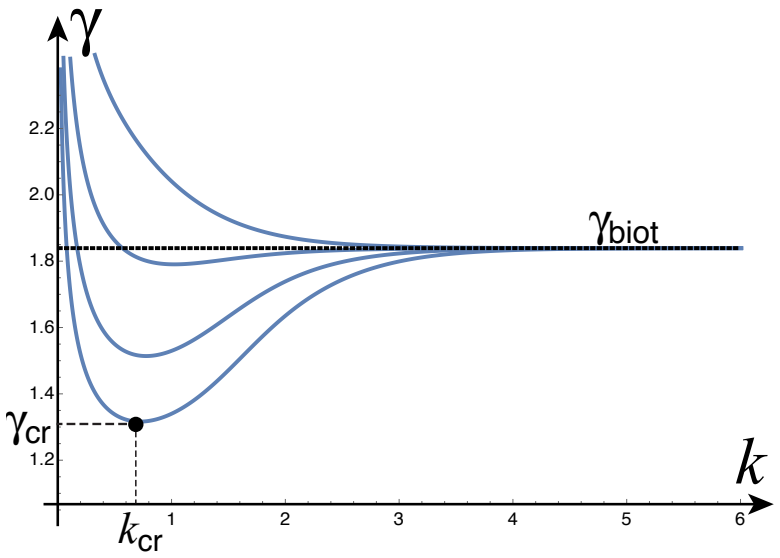


Figure 3.3: Solutions of the dispersion relation for a range of β values. In a thought experiment, the film grows starting at $\gamma = 1$. The homogeneous solution remains stable until a new solution emerges at $\gamma = \gamma_{\text{cr}}$ associated with wavenumber $k = k_{\text{cr}}$. For $\beta > \beta_{\text{min}}$, the solution arises before Biot's instability (indicated by a dashed line).The two upper curves are obtained for values of β just above and just below the critical value β_{min}.

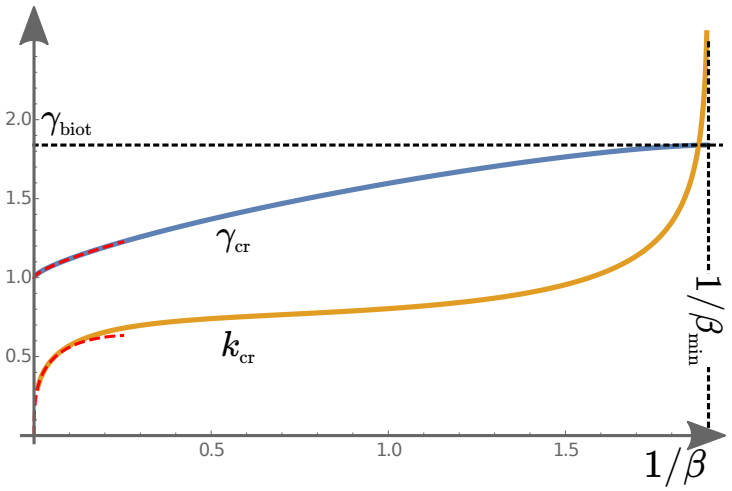


Figure 3.4: Critical solutions value of growth and wavenumber as a function of $1/\beta$ (asymptotic approximations shown dashed). Critical solutions exist for $\beta > \beta_{\text{min}} \approx 1/1.9$ after which, the Biot instability is the dominant instability.

As shown in Figure 3.4, for large values of β, the critical values are well approximated by

$$\gamma_{\mathrm{cr}}^2 = 1 + \frac{3^{2/3}}{2}\beta^{-2/3} + \frac{2\cdot 3^{1/3}}{5}\beta^{-4/3} + \frac{201}{2800}\beta^{-2} - \frac{27403}{112000\cdot 3^{1/3}}\beta^{-8/3} + \frac{583461\cdot 3^{1/3}}{21560000}\beta^{-10/3} - \frac{553132947}{22422400000}\beta^{-4} + \mathrm{O}(\beta^{-14/3}) \quad (3.20)$$

$$k_{\mathrm{cr}} = 3^{1/3}\beta^{-1/3} - \frac{11}{10}\beta^{-1} + \frac{881}{1400\cdot 3^{1/3}}\beta^{-5/3} + \frac{601}{2800\times 3^{2/3}}\beta^{-7/3} - \frac{1193837}{8624000}\beta^{-3} + \frac{56746499}{343200000\cdot 3^{1/3}}\beta^{-11/3} + \mathrm{O}(\beta^{-13/3}). \quad (3.21)$$

3.3 Generalisations

We now investigate a number of modifications to the physical problem that model different effects seen in nature. Of particular interest is the effect of these changes on the presence and position of Euler-type (large wavelength) and Biot-type (small wavelength) instabilities in the system. To this end, we repeat the linear analysis found in section 3.1, adding additional insights where necessary. Since the method has already been described at length, we briefly explain the new aspects of the problem without details.

3.3.1 Bilayer with surface tension

The first modification we consider is the addition of surface energy. In elastic solids, there is an energetic cost to maintaining a surface that we must incorporate into our variational formulation when the material is sufficiently soft or to model the effect of a small layer on top of the material surface. To do this, we add another term to the energy functional in (2.8) to represent the surface energy at the interface between the layers and/or at the top of the upper layer. Following Ben Amar and Bordner (2017), this contribution takes the form

$$d\int_{\Gamma} \mathrm{d}s, \quad (3.22)$$

where d is a constant surface energy density and Γ is a subset of $\partial\mathcal{B}_{\mathrm{f}} \cup \partial\mathcal{B}_{\mathrm{s}}$. In the present contribution, we take Γ to be the free surface $\{Y = 1\}$. The addition of

this term has no effect on the bulk Euler-Lagrange equations (2.16), but instead modifies the boundary conditions. In particular, (A.2a) becomes

$$\lambda^2 \frac{\mathrm{d}^3 h_{\mathrm{f}}^{(1)}}{\mathrm{d}Y^3}(1) - k^2(2\gamma^4 + \lambda^4)\frac{\mathrm{d}h_{\mathrm{f}}^{(1)}}{\mathrm{d}Y}(1) - d\beta^{-1}k^4\gamma^6\lambda h_{\mathrm{f}}^{(1)}(1) = 0. \tag{3.23}$$

This extra term adds dependence on the surface energy parameter d to the system of linear equations (3.8) so that it is now of the form

$$\hat{\mathbf{M}}(k, \gamma, \lambda, \beta, d)\mathbf{c} = \mathbf{0}. \tag{3.24}$$

As before, this homogeneous system of linear equations has nontrivial solutions precisely when the determinant of the matrix $\hat{\mathbf{M}}$ vanishes.

Compression

In the compression case ($\gamma = 1$), we can write the determinant in the form

$$\det \hat{\mathbf{M}}(k, \lambda, \beta, d) = \frac{1}{\lambda^5}\sum_{i=0}^{4} \hat{p}_i(k, \lambda, \beta, d)e^{k\zeta_i}, \tag{3.25}$$

where each $\hat{p}_i$ is some polynomial in its arguments and $(\zeta_i)_{i=0}^4 = (0, \lambda^{-1} + \lambda, -\lambda^{-1} + \lambda, \lambda^{-1} - \lambda, -\lambda^{-1} - \lambda)$. First, we remark that $k = 0$ is always a solution for $\lambda = \lambda_{\mathrm{biot}}$. Second, for large values of k, we have again that $\exp(k\zeta_1)$ is the dominant term and hence for large k, $\hat{p}_1$ must vanish. There is no longer a zero of this polynomial at λ_{biot} for all k, but there is still one at $\lambda_*(\beta)$ (for $\beta \neq 1$). For this root, we have $\lambda_*(\beta) < \lambda_{\mathrm{biot}}$ for all $\beta > 0$ as shown in fig. 3.5. Hence, we conclude that as λ decreases, it eventually reaches λ_{biot} at $k = 0$ which becomes the first instability.

When we compute the position of the critical growth and wavenumber as a function of β^{-1} (plotted in fig. 3.6), we see a dramatic change in the qualitative behaviour of both quantities. Firstly, we see the disappearance of the critical point for values of $\beta \lesssim 2.1$. However, the critical point ceases to be a global maximum before this occurs: for values of $\beta \lesssim 2.6$ the global maximum of the dispersion curve occurs at $k = 0$ with a selected compression ratio of λ_{biot}. Hence the addition of surface tension prevents the Biot instability from occurring, which is replaced by an Euler-type instability. If the film is sufficiently soft then the whole system buckles in a similar manner to a beam instead of displaying periodic fine wrinkling.

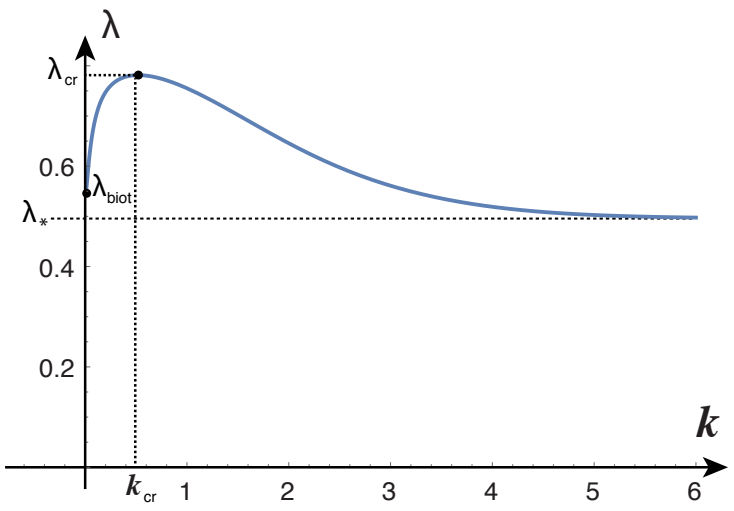


Figure 3.5: λ as a function of k for $\beta = 10$, $d = 7.5$ (here $k_{\mathrm{cr}} \approx 0.58$ and $\lambda_{\mathrm{cr}} \approx 0.78$).

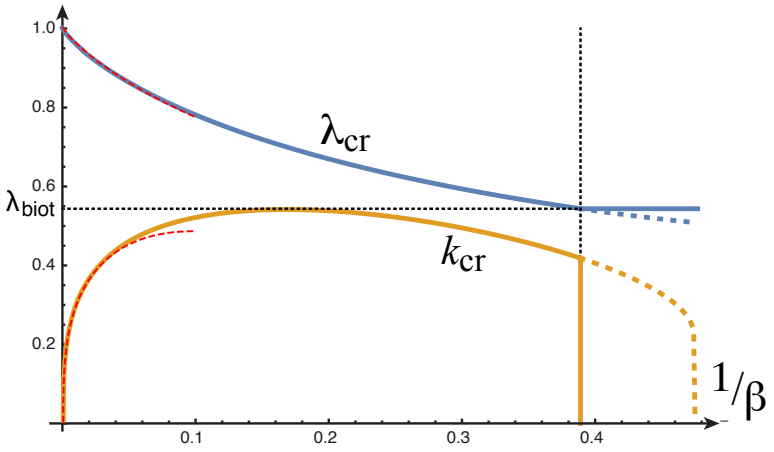


Figure 3.6: Exact (solid) and approximate (dashed) values of k_{cr} and λ_{cr} as functions of β^{-1} for $d = 7.5$

With the addition of another parameter, we can also fix the value of β and track the change in the critical growth and wavenumber as d varies. As one might expect, fig. 3.7 demonstrates that the higher the surface energy density, the lower the compression ratio required to induce wrinkling and the lower the wavenumber of the wrinkling.

As before, for large values of β corresponding to a stiff film on a soft substrate, the selected wavenumber becomes vanishingly small and the critical compression factor approaches 1. A standard asymptotic analysis reveals the following approximations (illustrated in fig. 3.6) that demonstrate the influence of the surface energy parameter

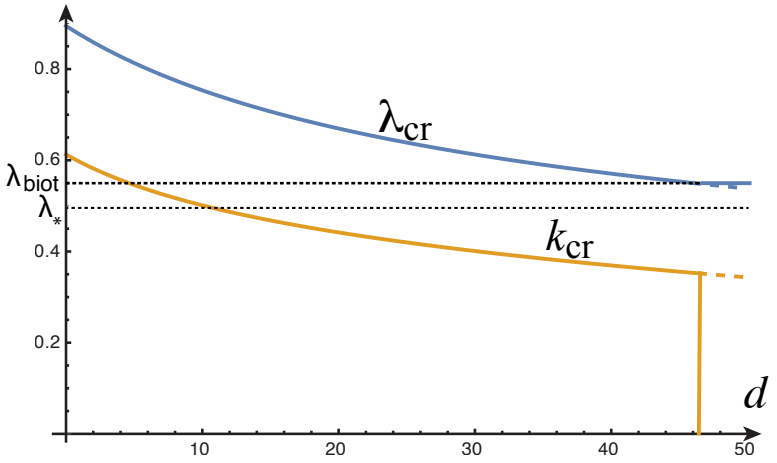


Figure 3.7: k_{cr} and λ_{cr} as functions of d for $\beta = 10$

d on the critical growth factor and wavenumber selection when compared to (3.14) and (3.15):

$$\lambda_{\mathrm{cr}} = 1 - \frac{3^{2/3}}{4}\beta^{-2/3} - \frac{d}{4}\beta^{-1} - \frac{33 \cdot 3^{1/3}}{160}\beta^{-4/3} - \frac{1}{16}\left(2 \cdot 3^{2/3} - 3 \cdot 3^{2/3} d\right)\beta^{-5/3} + O(\beta^{-2}), \tag{3.26}$$

$$k_{\mathrm{cr}} = 3^{1/3}\beta^{-1/3} - \frac{3}{5}\beta^{-1} - \frac{1}{4}3^{1/3} d \beta^{-4/3} + O(\beta^{-5/3}). \tag{3.27}$$

Growth

In the growth case, we can write the determinant in the form

$$\det \hat{\mathbf{M}}(k, \gamma, \beta, d) = \frac{1}{\gamma^3}\sum_{i=0}^{4} \hat{p}_i(k, \gamma, \beta, d) e^{k\zeta_i}, \tag{3.28}$$

where each $\hat{p}_i$ is some polynomial in its arguments and $(\zeta_i)_{i=0}^4 = (0, 1+\gamma^2, -1+\gamma^2, -1-\gamma^2, 1-\gamma^2)$. Consideration of the dominant term in the large k limit yields an asymptote at $\gamma = \gamma_*(\beta)$, which approaches γ_{biot} from above in the large β limit. As in the compression case, this asymptote is independent from d. The dispersion curve is similar to fig. 3.1 with $\gamma_*(\beta)$ replacing γ_{biot}. Echoing the results from the compression case, the critical growth factor is significantly increased, but occurs at a smaller wavenumber.

When we compute the position of the critical growth and wavenumber as a function of β^{-1} (plotted in fig. 3.8), we see a dramatic change in the qualitative

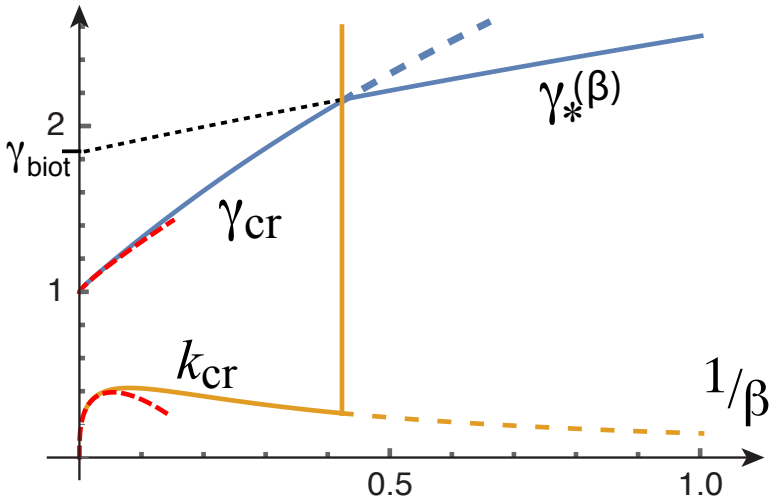


Figure 3.8: Exact (solid) and approximate (dashed) values of k_{cr} and γ_{cr} as functions of β^{-1} for $d = 7.5$

behaviour of both quantities. In particular, we no longer see a blow-up in the wavenumber as β decreases and we see an apparent increase in γ_{cr} without bound. However, the critical point that we are computing stops being a global minimum of γ for sufficiently small values of β. For β under this threshold, we would again expect a Biot-type instability.

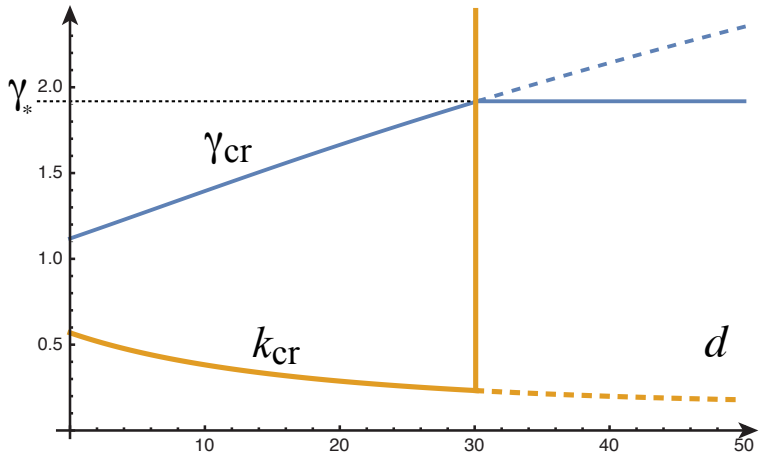


Figure 3.9: k_{cr} and γ_{cr} as functions of d for $\beta = 10$.

Plotting the critical growth factor and wavenumber as a function of d (shown in fig. 3.9) reveals that the higher the surface energy density, the higher the growth factor required to induce wrinkling and the lower the wavenumber of the wrinkling.

Another standard asymptotic analysis for large values of β gives the following

approximations (illustrated in fig. 3.8) for the correction that the surface energy parameter d induces on the critical growth factor:

$$\gamma_{\mathrm{cr}}^2 = 1 + \frac{3^{2/3}}{2}\beta^{-2/3} + \frac{d}{2}\beta^{-1} + \frac{2\cdot 3^{1/3}}{5}\beta^{-4/3} + \frac{5d}{8\cdot 3^{1/3}}\beta^{-5/3} + O(\beta^{-2}), \tag{3.29}$$

$$k_{\mathrm{cr}} = 3^{1/3}\beta^{-1/3} - \frac{11}{10}\beta^{-1} - \frac{5d}{4\cdot 3^{2/3}}\beta^{-4/3} + O(\beta^{-5/3}). \tag{3.30}$$

3.3.2 Bilayer with upper substrate

A second modification is to add another elastic layer (of either finite or infinite thickness) on top of the film. Here, we modify $\mathcal{B}$ to include an additional subdomain $\mathcal{B}_{\mathrm{t}}$ with shear modulus μ_{t} and relabel the stiffness ratios as $\beta_{\mathrm{f}} \coloneqq \mu_{\mathrm{f}}/\mu_{\mathrm{s}}$ and $\beta_{\mathrm{t}} \coloneqq \mu_{\mathrm{t}}/\mu_{\mathrm{s}}$. Considering the case of an infinitely thick top layer, for which $\mathcal{B}_{\mathrm{t}} = [-L, L]\times(0,\infty]$, we now have a system of three ODEs for our Euler-Lagrange equations:

$$\begin{aligned}
&\lambda^2\frac{\mathrm{d}^4 h_{\mathrm{t}}^{(1)}}{\mathrm{d}Y^4} - k^2(1+\lambda^4)\frac{\mathrm{d}^2 h_{\mathrm{t}}^{(1)}}{\mathrm{d}Y^2} + k^4\lambda^2 h_{\mathrm{t}}^{(1)} = 0,\\
&\lambda^2\frac{\mathrm{d}^4 h_{\mathrm{f}}^{(1)}}{\mathrm{d}Y^4} - k^2(\gamma^4+\lambda^4)\frac{\mathrm{d}^2 h_{\mathrm{f}}^{(1)}}{\mathrm{d}Y^2} + \gamma^4 k^4\lambda^2 h_{\mathrm{f}}^{(1)} = 0,\\
&\lambda^2\frac{\mathrm{d}^4 h_{\mathrm{s}}^{(1)}}{\mathrm{d}Y^4} - k^2(1+\lambda^4)\frac{\mathrm{d}^2 h_{\mathrm{s}}^{(1)}}{\mathrm{d}Y^2} + k^4\lambda^2 h_{\mathrm{s}}^{(1)} = 0,
\end{aligned} \tag{3.31}$$

with boundary conditions given in Appendix A. After consideration of the decay conditions at $Y \to +\infty$ ((A.3k) and (A.3l)), we obtain the following general solution for h_{t} (the others are unchanged):

$$h_{\mathrm{t}}(Y) = \begin{cases} c_7 e^{-kY} + c_8 Y e^{-kY} & \text{if } \lambda = 1,\\ c_7 e^{-k\lambda^{-1}Y} + c_8 e^{-k\lambda Y} & \text{otherwise.}\end{cases} \tag{3.32}$$

Following the same method as before, we obtain a homogeneous linear system of eight equations in the eight unknowns $\tilde{\mathbf{c}} \coloneqq \{c_i\}_{i=1}^8$. This leads to the solvability condition

$$\tilde{\mathbf{M}}(k,\gamma,\lambda,\beta_{\mathrm{f}},\beta_{\mathrm{t}})\tilde{\mathbf{c}} = \mathbf{0}, \tag{3.33}$$

which only has nontrivial solutions if $\det\tilde{\mathbf{M}} = 0$.

Compression

In the compression case, on numerically plotting the solution set of the determinant relation, we find a similar dispersion curve compared to the unmodified problem (fig. 3.1) but with λ_{biot} replaced by an asymptote λ_* that depends on both β_{f} and β_{t}.

The addition of another elastic layer decreases the critical compression ratio and the compression threshold for large k while increasing the critical wavenumber.

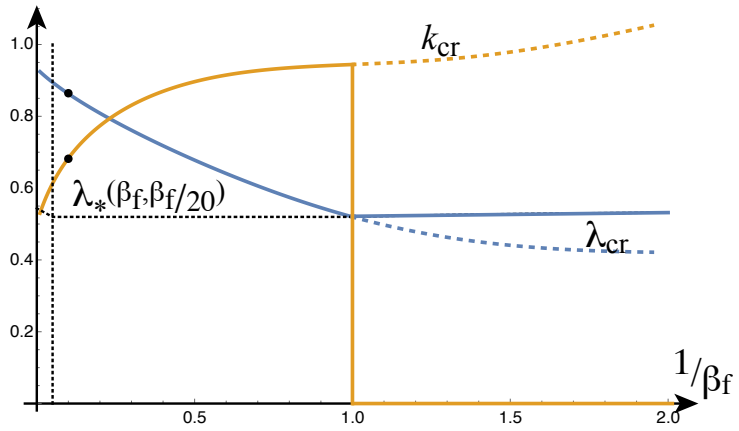


Figure 3.10: The critical wavenumber k_{cr} and compression λ_{cr} as functions of β_{f}^{-1} for $\beta_{\text{t}} = \beta_{\text{f}}/20$

For a given, fixed stiffness ratio $\beta_{\text{f}}\beta_{\text{t}}^{-1}$, from fig. 3.10 we can see that as β_{f} and β_{t} decrease, the critical compression ratio approaches the previously discussed threshold. However, we now find that for $\beta < 1$, we have an Euler-type buckling instability where the wavenumber $k = 0$ is selected.

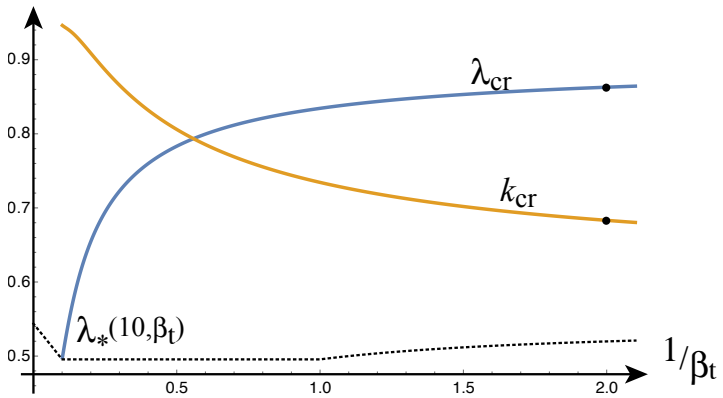


Figure 3.11: The critical wavenumber k_{cr} and compression λ_{cr} as functions of β_{t}^{-1} for $\beta_{\text{f}} = 10$

In contrast, fig. 3.11 shows us that if we fix β_f and vary β_t, we observe a gradual increase in λ_cr and a gradual decrease in k_cr as β_t decreases, with the wavenumber remaining well determined. Thus, the addition of an upper layer decreases the critical compression ratio and increases the critical wavenumber selected in the system.

For film with large stiffness, the asymptotic expressions are

$$\lambda_\mathrm{cr} = 1 - \frac{k_1^3 + 6\beta_\mathrm{t} + 6}{12\,k_1}\beta_\mathrm{f}^{-2/3} + \frac{99\,(\beta_\mathrm{t}+1)^{\,2}}{160\,k_1^2}\beta_\mathrm{f}^{-4/3} + O(\beta_\mathrm{f}^{-2}), \tag{3.34}$$

$$k_\mathrm{cr} = k_1\beta_\mathrm{f}^{-1/3} - \frac{3}{5}\,(\beta_\mathrm{t}+1) + O(\beta_\mathrm{f}^{-5/3}), \tag{3.35}$$

where $k_1 = (3 + 3\beta_\mathrm{f})^{1/3}$.

Growth

Repeating the techniques used in our previous cases, for large k we identify a critical growth threshold at a particular root $\gamma_\star(\beta_\mathrm{f}, \beta_\mathrm{t})$ of the following equation:

$$\begin{cases} \beta_\mathrm{f}^2\gamma^6 - (3\beta_\mathrm{f}^2 + 2\beta_\mathrm{f}\beta_\mathrm{t})\gamma^4 - (\beta_\mathrm{f}^2 + 4\beta_\mathrm{f}\beta_\mathrm{t} + 4\beta_\mathrm{t}^2)\gamma^2 - (\beta_\mathrm{f}^2 + 2\beta_\mathrm{f}\beta_\mathrm{t}) = 0 & \beta_\mathrm{t} < 1, \\ \beta_\mathrm{f}^2\gamma^6 - (3\beta_\mathrm{f}^2 + 2\beta_\mathrm{f})\gamma^4 - (\beta_\mathrm{f}^2 + 4\beta_\mathrm{f} + 4)\gamma^2 - (\beta_\mathrm{f}^2 + 2\beta_\mathrm{f}) = 0 & \beta_\mathrm{t} \geq 1 \end{cases} \tag{3.36}$$

Thus, we see that whichever substrate is softer dictates the position of the large k asymptote. In the limit of small β_t (very soft upper layer), we see that $\gamma_\star \to \gamma_\mathrm{biot}$ is a solution of the relation as before and we recover the bilayer. As in the compression case, the profile of the dispersion curve is similar to the corresponding unmodified problem (fig. 3.3). The addition of another elastic layer only slightly increases the critical growth factor, the critical wavenumber and the growth threshold for large k (shown in fig. 3.12).

Finally, fig. 3.13 demonstrates that if we again fix β_f and decrease β_t, γ_cr and k_cr both decrease with no apparent blow-up behaviour. Hence, the addition of an upper layer increases the critical growth factor and critical wavenumber selected in the system. In particular, as the stiffness of the upper layer approaches that of the film from below, the critical growth and wavenumber increase without bound.

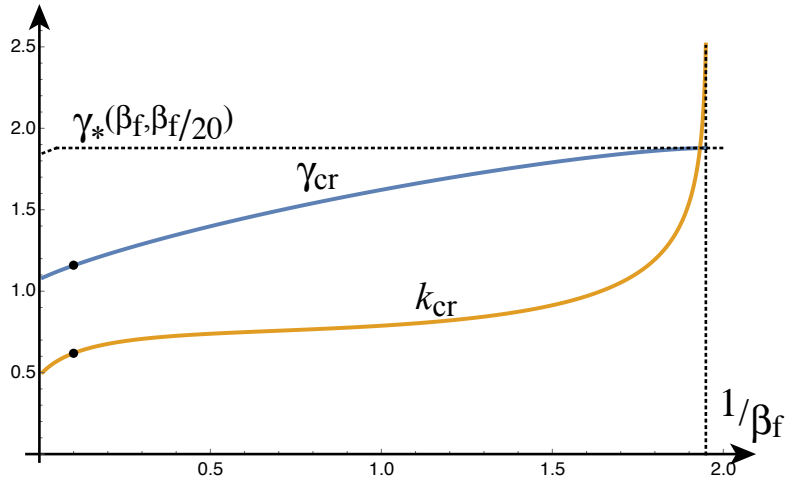


Figure 3.12: The critical wavenumber k_{cr} and compression λ_{cr}as functions of β_{f}^{-1} for $\beta_{\mathrm{t}} = \beta_{\mathrm{f}}/20$

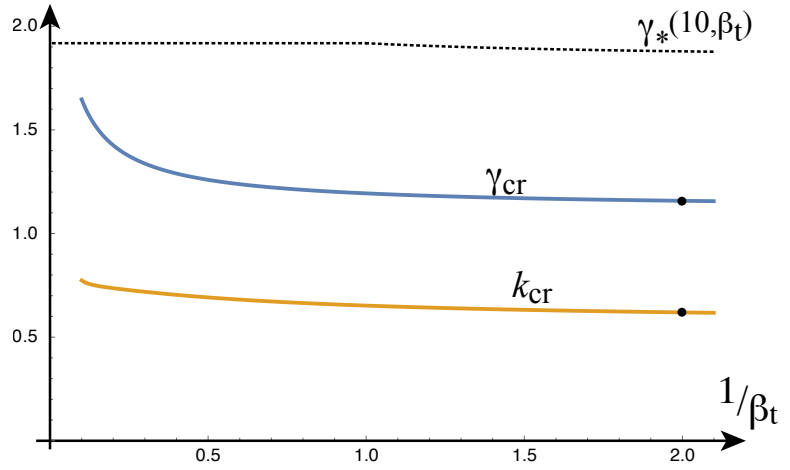


Figure 3.13: The critical wavenumber k_{cr} and compression λ_{cr} as functions of β_{t}^{-1} for $\beta_{\mathrm{f}} = 10$

3.3.3 Pressure

We can derive the effect of a normal pressure of magnitude p acting on the top of the film layer by directly imposing this constraint on the surface. A pressure p on the surface can be expressed in terms of the Cauchy stress tensor $\mathbf{T}$ as $\mathbf{T} \cdot \mathbf{n} = p\mathbf{n}$ for all points on the top surface. To express this condition, we compute, to first order, the normal vector field and the Cauchy stress. First, we recall that for a sufficiently regular deformation, the unit surface normal vector in the

deformed configuration is given by

$$\mathbf{n}(X) = \frac{1}{\sqrt{\left(\partial_X y(X,1)\right)^2 + 1}}(-\partial_X y(X,1), 1). \tag{3.37}$$

After changing coordinates into our stream function formulation, applying our perturbation $\Psi = \Psi^{(0)} + \epsilon\Psi^{(1)}$ from the homogeneous solution (3.1) and our periodic decomposition $\Psi^{(1)}(x,Y) = \sin(kx)h^{(1)}(Y)$, we can rewrite (3.37) as:

$$\mathbf{n}(x) = (0,1) + (1, \frac{1}{2})k^2 h(1)\sin(kx)\epsilon + O(\epsilon^2). \tag{3.38}$$

Second, we compute the Cauchy stress by using the constitutive equations for an incompressible neo-Hookean material:

$$\overline{\mathbf{T}} = \mu\mathbf{A}\mathbf{A}^T - q\mathbf{I}, \tag{3.39}$$

where q denotes the Lagrange multiplier associated with incompressibility. We expand both $\overline{\mathbf{T}} = \overline{\mathbf{T}}^{(0)} + \epsilon\overline{\mathbf{T}}^{(0)}$ and $q = q_0 + \epsilon q_1$. Since the base solution is homogeneous, it can be solved directly by using the boundary condition and to order 0 in ϵ, we find

$$\mathbf{T}^{(0)} = \begin{pmatrix} \frac{\lambda^2\mu_\mathrm{f}}{\gamma^2} - q_0 & 0 \\ 0 & \frac{\gamma^2\mu_\mathrm{f}}{\lambda^2} - q_0 \end{pmatrix}, \tag{3.40}$$

where $q_0 = \lambda^{-2}(\gamma^2\mu_\mathrm{f} - p\lambda^2)$. To first order, we use the the equilibrium equation

$$\operatorname{div}\overline{\mathbf{T}} = \mathbf{0}, \tag{3.41}$$

to find

$$\overline{\mathbf{T}}^{(1)} = \begin{pmatrix} -\frac{2k\mu\cos(kx)\lambda^2}{\gamma^4}\frac{\mathrm{d}h_\mathrm{f}^{(1)}}{\mathrm{d}Y} - q_1(Y) & -\frac{\mu\sin(kx)}{\gamma^2\lambda}\left(k^2h_1(Y)\lambda^2 + \frac{\mathrm{d}^2h_\mathrm{f}^{(1)}}{\mathrm{d}Y^2}\right) \\ -\frac{\mu\sin(kx)}{\gamma^2\lambda}\left(k^2h_1(Y)\lambda^2 + \frac{\mathrm{d}^2h_\mathrm{f}^{(1)}}{\mathrm{d}Y^2}\right) & \frac{2k\mu\cos(kx)}{\lambda^2}\frac{\mathrm{d}h_\mathrm{f}^{(1)}}{\mathrm{d}Y} - q_1(Y) \end{pmatrix}, \tag{3.42}$$

where

$$q_1 = \frac{\mu_\mathrm{f}}{\gamma^4 k}\cos(kx)\left(\frac{\mathrm{d}^3h_\mathrm{f}^{(1)}}{\mathrm{d}Y^3} - k^2\lambda^2\frac{\mathrm{d}h_\mathrm{f}^{(1)}}{\mathrm{d}Y}\right). \tag{3.43}$$

Substituting these expressions into the first-order traction condition

$$\overline{\mathbf{T}}^{(0)}\cdot\mathbf{n}^{(1)} + \overline{\mathbf{T}}^{(1)}\cdot\mathbf{n}^{(0)} = p\mathbf{n}^{(1)}, \tag{3.44}$$

yields precisely (A.2a) and (A.2b). We conclude that the pressure has no effect on the linear analysis of the system: a bilayer develops the same wrinkling instability regardless of the pressure.

3.3.4 Fibre-reinforced substrate

A last modification we make to the bilayer system is to introduce embedded elastic fibres into the elastic substrate, as considered in Stewart et al. (2016). This adds an orientational anisotropy into the system that mimics structures seen in many biological materials. For simplicity, we restrict our attention to the case of a single family of fibres with a vertical orientation and no pre-stretch. To describe the energetic cost of deforming the fibres, we add the following term to the energy density function (Goriely and Tabor, 2013; Melnik, Rocha, and Goriely, 2015):

$$W_r(\mathbf{A}) = m\left((\mathbf{A}\cdot\mathbf{N})\cdot(\mathbf{A}\cdot\mathbf{N})-1\right)^2, \tag{3.45}$$

where $\mathbf{N}$ is a vertical unit vector in the reference configuration and m quantifies both the stiffness of the fibres and their volume fraction. As this modification changes the bulk energy, it has a corresponding effect on the Euler-Lagrange equation for the substrate. After perturbation and periodic decomposition, it reads:

$$\left(\lambda^2-4m(1-\lambda^{-2})\right)\frac{\mathrm{d}^4h_{\mathrm{s}}^{(1)}}{\mathrm{d}Y^4}-k^2\left(1+\lambda^4-4m(1-3\lambda^{-2})\right)\frac{\mathrm{d}^2h_{\mathrm{s}}^{(1)}}{\mathrm{d}Y^2}+k^4\lambda^2h_{\mathrm{s}}^{(1)}=0. \tag{3.46}$$

Similarly, the traction boundary conditions at the film-substrate interface become

$$\begin{aligned}\beta\left(\lambda\frac{\mathrm{d}^3h_{\mathrm{f}}^{(1)}}{\mathrm{d}Y^3}(0)-k^2\lambda^{-1}(2\gamma^4+\lambda^4)\frac{\mathrm{d}h_{\mathrm{f}}^{(1)}}{\mathrm{d}Y}(0)\right)=\\ \gamma^4\left(\left(\lambda-4m(\lambda-\lambda^{-1})\right)\frac{\mathrm{d}^3h_{\mathrm{s}}^{(1)}}{\mathrm{d}Y^3}(0)-k^2\lambda^{-1}\left(2+\lambda^4-8m(1-2\lambda^{-2})\right)\frac{\mathrm{d}h_{\mathrm{s}}^{(1)}}{\mathrm{d}Y}(0)\right),\end{aligned} \tag{3.47a}$$

$$\begin{aligned}\beta\left(\lambda\frac{\mathrm{d}^2h_{\mathrm{f}}^{(1)}}{\mathrm{d}Y^2}(0)+k^2\gamma^4\lambda^{-1}h_{\mathrm{f}}^{(1)}(0)\right)=\\ \gamma^2\left(1-4m(1-\lambda^{-2})\right)\left(\lambda\frac{\mathrm{d}^2h_{\mathrm{s}}^{(1)}}{\mathrm{d}Y^2}(0)+k^2\lambda^{-1}h_{\mathrm{s}}^{(1)}(0)\right).\end{aligned} \tag{3.47b}$$

Compression

In the compression case, the addition of fibres initially seems to have a limited effect. Compared to the unmodified case with the same large stiffness ratio, adding fibres

with $0 < m < 1$ causes the critical wavenumber to increase, the critical compression ratio to decrease and has no effect on the large k asymptote.

However, as we vary the stiffness ratio, we see some markedly different behaviour in the evolution of the critical point as a function of β (demonstrated in fig. 3.14). For stiffness ratios $\beta < \beta_c \approx 8$, the critical wavenumber rapidly decreases. This local maximum close to $k = 0$ persists even when $\beta > 1$ (at $\beta = 1$ we have no length scale and the wavelength is again undetermined). The position of the critical compression ratio does not appear to degenerate to λ_{biot} for small values of β.

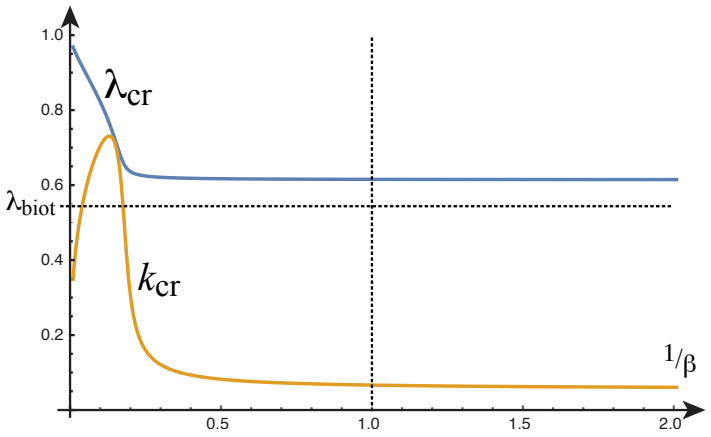


Figure 3.14: k_{cr} and λ_{cr} as functions of β^{-1} for $m = 5/9$

Increasing the fibre stiffness parameter m (shown in fig. 3.15) has a similar effect; for fibres stiffer than $m = m_c \approx 0.67$, the critical wavenumber becomes close to $k = 0$.

To summarise, for fibres significantly stiffer than the elastic substrate in which they are embedded, we see a lower wavenumber wrinkling pattern emerge.

Growth

In the growth case, the addition of fibres causes both the critical wavenumber and the critical growth factor to increase slightly but the large k behaviour of the system is unchanged. The critical growth factor and wavenumber have a similar qualitative behaviour compared to the unmodified case with the notable characteristic that the stiffness ratio $1/\beta_{\text{min}}$ at which the wavenumber blows up is significantly reduced. Plotting the dependence of the critical growth factor and wavenumber on the fibre

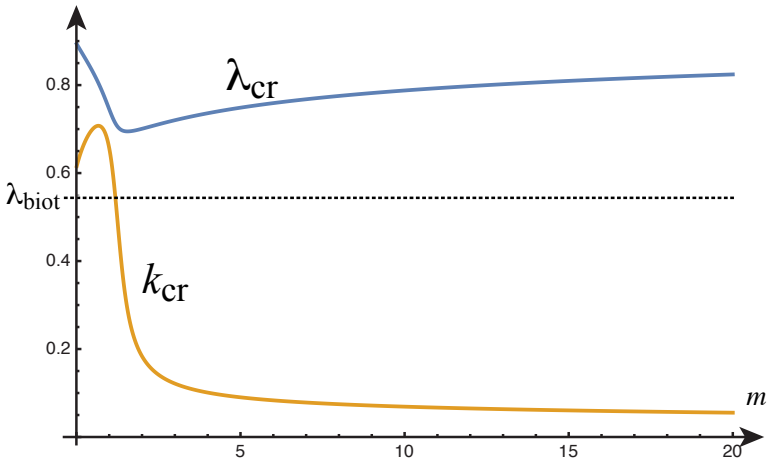


Figure 3.15: k_{cr} and λ_{cr} as functions of m for $\beta = 10$

stiffness parameter m as in fig. 3.16 shows a gradual increase in both quantities as the fibres become stiffer. For a fixed β, there exists a finite (but extremely large) m such that $\gamma_{\mathrm{cr}} = \gamma_{\mathrm{biot}}$ and k_{cr} becomes infinite.

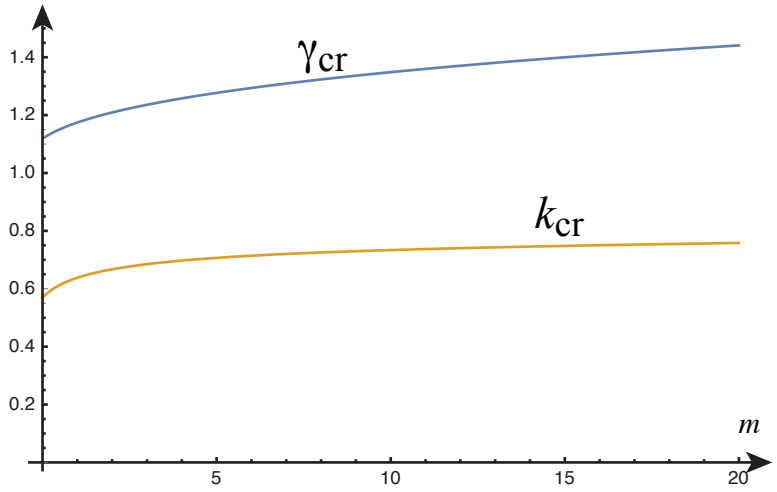


Figure 3.16: k_{cr} and γ_{cr} as functions of m for $\beta = 10$

3.4 Conclusions

We have presented a complete linear analysis for the plane-strain wrinkling of a film on an elastic substrate in the case of lateral compression and film growth. The analysis does not make any approximation on the thinness of the film or the relative stiffness ratio between substrate and film. Hence, it can be used as a general

benchmark for approximate theories and identify their domain of validity. We also considered the role of secondary effects such as surface tension, pressure, and fibres.

Our analysis further establishes that for films that are much stiffer than the substrate, a regular asymptotic expression in powers of $1/\beta$ leads to accurate predictions for the critical parameter and critical wavenumber selected at the wrinkling instability even when supplementary effects are considered. A rule of thumb is that for $\beta \gtrsim 10$, a 3-term expansion is sufficient in all cases to capture the correct behaviour. It also suggests that in this regime, approximate theories (beams and plates) may be sufficient as long as they correctly model the effect of the substrate. Our analysis can be used to gauge this calibration by matching the asymptotic behaviours of a plate or beam to the ones derived here.

As β decreases, a number of different effects appear that make general conclusions harder to reach. Depending on both the loading and the effect considered, qualitatively different behaviours are observed. For instance, the addition of any surface tension in compression changes the Biot surface instability ($k_{\mathrm{cr}} \to \infty$) to a Euler-type instability ($k_{\mathrm{cr}} \to 0$). Yet, the Biot instability is still the first selected for a growing film. Similarly, the minimal value β_{min} at which a linear instability is found depends greatly on both the loading and extra surface effects. It is therefore harder to obtain a general picture for the bifurcation of soft films on substrate. Yet, the linear analysis may not even be relevant in that regime for two reasons.

First, the film may undergo a creasing instability for values of the axial stretch around $\lambda = 1/\gamma \approx 0.64$ (Ciarletta, 2018). Hence, the linear unstable wrinkling mode may not be observed past that critical value. Whether this instability is universally observed in bilayers and always selected is still an open problem.

Second, the analysis performed here is only a linear analysis and does not allow us to conclude about the existence of periodic solutions past the bifurcation point. The main problem is that the wrinkling instability may be supercritical or subcritical depending on the stiffness ratio (Cao and Hutchinson, 2011; Cao and Hutchinson, 2012; Hutchinson, 2013; Ciarletta and Fu, 2015; Fu and Ciarletta, 2015). Previous studies suggest that for sufficiently stiff films, the wrinkling instability

is supercritical. The question is then to determine the value of β at which this supercritical bifurcation becomes subcritical and whether this value occurs before or after the Biot instability or the wrinkling instability.

This chapter is derived from Alawiye, Farrell, and Goriely (2020).

4 Derivation of the amplitude relation

Contents

4.1 Growth case 57
4.1.1 On creasing 62
4.1.2 Verification of the amplitude relation 63
4.2 Compression case 64

4.1 Growth case

We first focus on the growth case and extend our previous analysis by including higher order terms in our perturbation expansion of the stream function. This will allow us to derive a so-called *amplitude equation*, the solutions of which specify the as-of-yet undetermined amplitude of the oscillatory solutions. At this point, we also allow the amplitude to depend on a far spatial $\zeta := \epsilon x$ and a slow temporal variable $\tau := \epsilon t$ that evolve over longer length and time scales than the oscillations themselves. We consider perturbations of the form

$$\Psi = \Psi^{(0)} + \epsilon\Psi^{(1)} + \epsilon^2\Psi^{(2)} + \epsilon^3\Psi^{(3)}, \tag{4.1}$$

and furthermore perturb the critical parameter

$$\gamma = \gamma_{\mathrm{cr}}(1 + \epsilon^2\gamma_1). \tag{4.2}$$

We then take periodic decompositions of the form

$$\begin{aligned}
\Psi^{(1)}(x,Y,t) =& a(\epsilon x,\epsilon t)h^{(1,1)}(Y)e^{ikx} + \text{c.c.},\\
\Psi^{(2)}(x,Y,t) =& a(\epsilon x,\epsilon t)^2h^{(2,2)}(Y)e^{2ikx} + \partial_\zeta a(\epsilon x,\epsilon t)h^{(2,1)}(Y)e^{ikx} + \text{c.c.},\\
\Psi^{(3)}(x,Y,t) =& a(\epsilon x,\epsilon t)^3h^{(3,3)}(Y)e^{3ikx} + 2a(\epsilon x,\epsilon t)\partial_\zeta a(\epsilon x,\epsilon t)h^{(3,2)}(Y)e^{2ikx}\\
&+ \partial_{\zeta\zeta} a(\epsilon x,\epsilon t)h^{(3,1)}(Y)e^{ikx} + \text{c.c.},
\end{aligned} \tag{4.3}$$

where c.c. denotes the complex conjugate of all preceding expressions. To deal with the added slow dynamics of the system, we replace our neo-Hookean energy density W with the Lagrangian density

$$\frac{1}{2}\rho\left|\frac{\partial \mathbf{x}}{\partial t}\right|^2 - W(\mathbf{A}). \tag{4.4}$$

To use this in our formulation, we must be able to express the kinetic energy of the system in terms of stream functions. We can compute the components of the time derivative of the displacement as

$$\begin{aligned}
\frac{\partial x}{\partial t} &= -\frac{\partial_{Yt}\Psi}{\partial_{xY}\Psi}\\
\frac{\partial y}{\partial t} &= \frac{1}{\lambda}\left(\partial_{xt}\Psi - \frac{\partial_{Yt}\Psi\partial_{xx}\Psi}{\partial_{xY}\Psi}\right).
\end{aligned} \tag{4.5}$$

Combining these expressions with (4.4), we can write the Lagrangian of the system in the form

$$\tilde{I}(\Psi) = \int_{\tilde{\mathcal{B}}} f(\partial_{xx}\Psi, \partial_{xY}\Psi, \partial_{YY}\Psi, \partial_{xt}\Psi, \partial_{Yt}\Psi)\,\mathrm{d}x\mathrm{d}Y. \tag{4.6}$$

The Euler-Lagrange equations are then given by

$$\begin{aligned}
&\frac{\partial^2}{\partial x^2}\left(\frac{\partial f}{\partial(\partial_{xx}\Psi_{\mathrm{f}})}\right) + \frac{\partial^2}{\partial x\partial Y}\left(\frac{\partial f}{\partial(\partial_{xY}\Psi_{\mathrm{f}})}\right) + \frac{\partial^2}{\partial Y^2}\left(\frac{\partial f}{\partial(\partial_{YY}\Psi_{\mathrm{f}})}\right)\\
&\qquad + \frac{\partial^2}{\partial x\partial t}\left(\frac{\partial f}{\partial(\partial_{xt}\Psi_{\mathrm{f}})}\right) + \frac{\partial^2}{\partial Y\partial t}\left(\frac{\partial f}{\partial(\partial_{Yt}\Psi_{\mathrm{f}})}\right) = 0,\\
&\frac{\partial^2}{\partial x^2}\left(\frac{\partial f}{\partial(\partial_{xx}\Psi_{\mathrm{s}})}\right) + \frac{\partial^2}{\partial x\partial Y}\left(\frac{\partial f}{\partial(\partial_{xY}\Psi_{\mathrm{s}})}\right) + \frac{\partial^2}{\partial Y^2}\left(\frac{\partial f}{\partial(\partial_{YY}\Psi_{\mathrm{s}})}\right)\\
&\qquad + \frac{\partial^2}{\partial x\partial t}\left(\frac{\partial f}{\partial(\partial_{xt}\Psi_{\mathrm{s}})}\right) + \frac{\partial^2}{\partial Y\partial t}\left(\frac{\partial f}{\partial(\partial_{Yt}\Psi_{\mathrm{s}})}\right) = 0.
\end{aligned} \tag{4.7}$$

The linear analysis we have already carried out is unchanged by these modifications (although we relabel $h_{\mathrm{f}}^{(1)}$ as $h_{\mathrm{f}}^{(1,1)}$ and c_i as $c_i^{(1,1)}$), so we proceed to the second order. After substituting (4.1) into (2.16), the Euler-Lagrange equations for the first mode at second order in ϵ read

$$\begin{aligned}\frac{\mathrm{d}^4 h_{\mathrm{f}}^{(2,1)}}{\mathrm{d}Y^4} - k^2(1+\gamma_{\mathrm{cr}}^4)\frac{\mathrm{d}^2 h_{\mathrm{f}}^{(2,1)}}{\mathrm{d}Y^2} + \gamma_{\mathrm{cr}}^4 k^4 h_{\mathrm{f}}^{(2,1)} &= -2ik(1+\gamma_{\mathrm{cr}}^4)\frac{\mathrm{d}^2 h_{\mathrm{f}}^{(1,1)}}{\mathrm{d}Y^2} + 4ik^3\gamma_{\mathrm{cr}}^4 h_{\mathrm{f}}^{(1,1)},\\ \frac{\mathrm{d}^4 h_{\mathrm{s}}^{(2,1)}}{\mathrm{d}Y^4} - 2k^2\frac{\mathrm{d}^2 h_{\mathrm{s}}^{(2,1)}}{\mathrm{d}Y^2} + k^4 h_{\mathrm{s}}^{(2,1)} &= -4ik\frac{\mathrm{d}^2 h_{\mathrm{s}}^{(1,1)}}{\mathrm{d}Y^2} + 4ik^3 h_{\mathrm{s}}^{(1,1)}.\end{aligned} \tag{4.8}$$

We also obtain a complex conjugate set of equations. On substitution of the first order solution, we can write each of the equations (4.8) in the form

$$\mathcal{L}^{(1)}[h^{(2,1)}] = \mathscr{F}^{(2,1)}, \tag{4.9}$$

where $\mathcal{L}^{(n)}$ is one of the linear differential operators

$$\begin{aligned}\mathcal{L}_{\mathrm{f}}^{(n)}[h] &\coloneqq \frac{\mathrm{d}^4 h}{\mathrm{d}Y^4} - (nk)^2(1+\gamma_{\mathrm{cr}}^4)\frac{\mathrm{d}^2 h}{\mathrm{d}Y^2} + \gamma_{\mathrm{cr}}^4 (nk)^4 h,\\ \mathcal{L}_{\mathrm{s}}^{(n)}[h] &\coloneqq \frac{\mathrm{d}^4 h}{\mathrm{d}Y^4} - 2(nk)^2\frac{\mathrm{d}^2 h}{\mathrm{d}Y^2} + (nk)^4 h,\end{aligned} \tag{4.10}$$

and $\mathscr{F}^{(2,1)}$ represents a (known) scalar, nonlinear function of β (through γ_{cr} and k). The equations for the second mode at second order can also be written in a similar form:

$$\mathcal{L}^{(2)}[h^{(2,2)}] = \mathscr{F}^{(2,2)}. \tag{4.11}$$

We can then solve these equations exactly using computer-based symbolic algebra as the particular integrals are straightforward but intractable by hand. By again considering decay conditions of the form $\lim_{Y\to-\infty} h_{\mathrm{s}} = 0$, we obtain the general solutions

$$\begin{aligned}h_{\mathrm{f}}^{(2,1)}(Y) &= c_1^{(2,1)}e^{-k\gamma_{\mathrm{cr}}^2 Y} + c_2^{(2,1)}e^{k\gamma_{\mathrm{cr}}^2 Y} + c_3^{(2,1)}e^{-kY} + c_4^{(2,1)}e^{kY} + \mathscr{G}_{\mathrm{f}}^{(2,1)},\\ h_{\mathrm{s}}^{(2,1)}(Y) &= c_5^{(2,1)}e^{kY} + c_6^{(2,1)}Ye^{kY} + \mathscr{G}_{\mathrm{s}}^{(2,1)},\end{aligned} \tag{4.12}$$

and

$$\begin{aligned}h_{\mathrm{f}}^{(2,2)}(Y) &= c_1^{(2,2)}e^{-2k\gamma_{\mathrm{cr}}^2 Y} + c_2^{(2,2)}e^{2k\gamma_{\mathrm{cr}}^2 Y} + c_3^{(2,2)}e^{-2kY} + c_4^{(2,2)}e^{2kY} + \mathscr{G}_{\mathrm{f}}^{(2,2)},\\ h_{\mathrm{s}}^{(2,2)}(Y) &= c_5^{(2,2)}e^{2kY} + c_6^{(2,2)}Ye^{2kY} + \mathscr{G}_{\mathrm{s}}^{(2,2)}.\end{aligned} \tag{4.13}$$

where each $\mathscr{G}$ is a (known) scalar, nonlinear function of $k(\beta)$ and $\gamma_{\mathrm{cr}}(\beta)$. To determine the arbitrary coefficients in (4.12) and (4.13), we must apply the boundary conditions (we omit their precise form for brevity) to obtain two inhomogeneous systems of linear equations of the form

$$\mathbf{M}^{(2,1)}\mathbf{c}^{(2,1)} = \boldsymbol{\mathscr{H}}^{(2,1)}, \tag{4.14}$$

$$\mathbf{M}^{(2,2)}\mathbf{c}^{(2,2)} = \boldsymbol{\mathscr{H}}^{(2,2)}, \tag{4.15}$$

for some (known) nonlinear, vector-valued functions $\boldsymbol{\mathscr{H}}$ of $k(\beta)$, $\gamma_{\mathrm{cr}}(\beta)$, and β. On closer inspection, we find that $\mathbf{M}^{(2,1)}$ is singular and so we must establish whether any solutions to (4.14) do in fact exist. The Fredholm alternative tells us that the system has a solution if and only if every $\boldsymbol{\xi}$ in the left null space of $\mathbf{M}^{(2,1)}$ satisfies

$$\boldsymbol{\xi}\boldsymbol{\mathscr{H}}^{(2,1)} = 0. \tag{4.16}$$

This condition is satisfied identically and $\mathbf{M}^{(2,2)}$ has full rank so we can proceed to third order.

After substituting (4.1) and the computed first and second-order solutions into (2.16), the Euler-Lagrange equations for the first mode at third order in ϵ can be written in a similar form to (4.9):

$$\mathcal{L}^{(1)}[h^{(3,1)}] = \mathscr{F}^{(3,1)}. \tag{4.17}$$

We finally see the impact of the perturbed growth factor in (4.2) as $\mathscr{F}^{(3,1)}$ is a function of γ_1 in addition to $\gamma_{\mathrm{cr}}(\beta)$ and $k(\beta)$. We then obtain the general solutions

$$\begin{aligned} h_{\mathrm{f}}^{(3,1)}(Y) &= c_1^{(3,1)}e^{-k\gamma_{\mathrm{cr}}^2 Y} + c_2^{(3,1)}e^{k\gamma_{\mathrm{cr}}^2 Y} + c_3^{(3,1)}e^{-kY} + c_4^{(3,1)}e^{kY} + \mathscr{G}_{\mathrm{f}}^{(3,1)}, \\ h_{\mathrm{s}}^{(3,1)}(Y) &= c_5^{(3,1)}e^{kY} + c_6^{(3,1)}Ye^{kY} + \mathscr{G}_{\mathrm{s}}^{(3,1)}, \end{aligned} \tag{4.18}$$

with $\mathscr{G}_{\mathrm{f}}^{(3,1)}$ featuring dependence on γ_1 in addition to $k(\beta)$ and $\gamma_{\mathrm{cr}}(\beta)$. On applying the boundary conditions, we find a mismatch that will allow us to constrain the amplitude of the oscillations of our solution. The inhomogeneous system of linear equations for the arbitrary coefficients in (4.18) is of the form

$$\mathbf{M}^{(3,1)}\mathbf{c}^{(3,1)} = \boldsymbol{\mathscr{H}}^{(3,1)}, \tag{4.19}$$

where $\mathscr{H}^{(3,1)}$ contains the γ_1 dependence. On left-multiplying both sides of (4.19) by a vector $\boldsymbol{\xi}$ from the left nullspace of the singular matrix $\mathbf{M}^{(3,1)}$, we obtain

$$\boldsymbol{\xi}\mathscr{H}^{(3,1)} = 0. \tag{4.20}$$

Closer inspection reveals that (4.20) is an equation of the form

$$\frac{\partial^2 a}{\partial \tau^2} - \mathscr{C}_2 \frac{\partial^2 a}{\partial \zeta^2} = \mathscr{C}_0 \gamma_1 a + \mathscr{C}_1 |a|^2 a, \tag{4.21}$$

where $\mathscr{C}_0$, $\mathscr{C}_1$ and $\mathscr{C}_2$ are real-valued functions of β. This equation is a nonlinear Klein-Gordon equation, typical for pitchfork bifurcations in spatially-extended conservative problems found in solid mechanics (see e.g. Lange and Newell, 1971; Goriely, Nizette, and Tabor, 2001).

For instance, substituting in the previously computed critical parameter values for $\beta = 10$ yields $\mathscr{C}_0 \approx 4.75$ and $\mathscr{C}_1 \approx -0.05$. In the case of constant amplitude, nontrivial solutions for a are given by

$$|a|^2 = -\frac{\mathscr{C}_0}{\mathscr{C}_1}\gamma_1. \tag{4.22}$$

It is immediately apparent that the sign of $\mathscr{C}_0$ and $\mathscr{C}_1$ is of particular importance in determining the type of bifurcation (Cai and Fu, 1999; Fu and Ogden, 1999). Indeed a direct analysis for the existence of homogeneous solutions of this amplitude equation shows that the bifurcation will be subcritical for values of $\mathscr{C}_1 > 0$ and supercritical for values of $\mathscr{C}_1 < 0$. We plot the dependence of $\mathscr{C}_0$ and $\mathscr{C}_1$ on β in fig. 4.1 and track the changes in sign that signify qualitative changes in physical behaviour.

Recalling that we must have $\beta > \beta_{\min} \approx 1.9^{-1}$ for the instability to take place, the bifurcation is subcritical for

$$\beta_{\min} < \beta < 0.95^{-1} \tag{4.23}$$

and supercritical for

$$\beta > 0.95^{-1} \tag{4.24}$$

We can now focus on the particular parameter value $\beta_{\text{ss}} \approx 0.95^{-1}$ where the bifurcation goes from supercritical to subcritical. We return to the critical solutions of the dispersion relation illustrated in fig. 3.4 and identify the critical growth factor $\gamma_{\text{ss}} \approx 1.576$ associated with β_{ss} (shown in fig. 4.2).

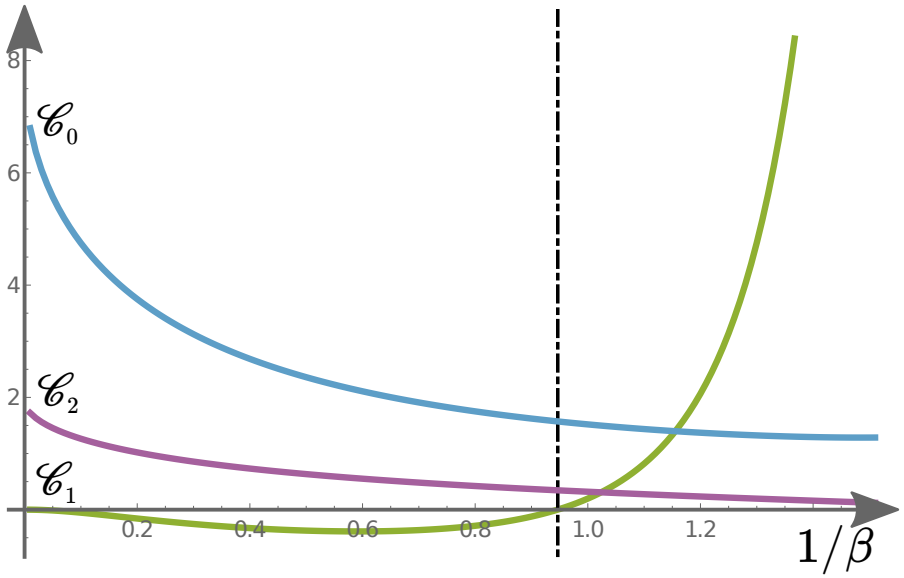


Figure 4.1: $\mathscr{C}_0$, $\mathscr{C}_1$ and $\mathscr{C}_2$ as functions of β^{-1} in the growth case

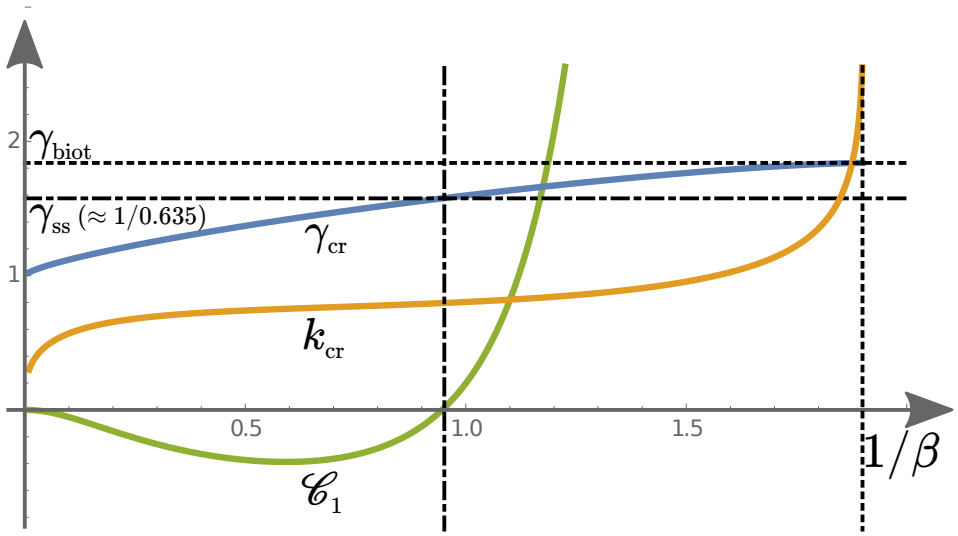


Figure 4.2: Growth factor γ_{ss} at the super-to-sub transition

4.1.1 On creasing

It has long been known that homogeneous soft elastic solids under compressive stress will undergo a creasing instability—the development of localised, self-contacting cusps on the free surface—rather than a wrinkling instability, thus avoiding the quandary of wrinkling length scale posed by Biot (1963). It has been well documented in the experimental and numerical literature that for bilayers

Reference	$\varepsilon_{\text{crease}}$	Method
Ciarletta and Truskinovsky, 2019	0.364	theory: asymptotic matching
Ciarletta, 2018	0.362	theory: asymptotic matching
Jin et al., 2015	0.35–0.36	simulation: finite element
Diab and Kim, 2014	0.35	simulation: finite element
Hohlfeld, 2013	0.35	simulation: finite element
Hohlfeld and Mahadevan, 2011	0.354	simulation: finite element
Wong et al., 2010	0.35	simulation: finite element
Hong, Zhao, and Suo, 2009	0.35	simulation: finite element
Tang et al., 2017	0.33–0.38	experiment: PDMS
Wang and Zhao, 2015	0.36	experiment: elastomer
Jin et al., 2015	0.37	experiment: PDMS
Trujillo, Kim, and Hayward, 2008	0.33	experiment: hydrogel

Table 4.1: Previous results on the critical strain $\varepsilon_{\text{crease}}$ required for creasing

with a sufficiently soft upper layer, we also see a creasing instability (see Wang and Zhao (2015)).

At the point of the super-to-sub transition, the strain in the upper layer of the homogeneous trivial solution is given by $1 - \gamma_{\text{ss}}^{-1} \approx 0.365$. This is noteworthy by virtue of the fact that it corresponds almost exactly to the critical strain associated with some experimental studies on creasing in soft polymers (Trujillo, Kim, and Hayward, 2008; Tang et al., 2017) (a summary of significant results in the literature can be found in table 4.1). While our analysis does not yet constructively say anything about the formation of creases, the coincidence of the computed value of strain at the point at which wrinkling becomes unstable and the observed value for strain for which we expect a homogeneous medium to crease suggests that these phenomena might be related, or at least that these two instabilities may interact in the nonlinear regime.

4.1.2 Verification of the amplitude relation

Clearly, $a \equiv 0$ is always a solution of (4.21). For values of γ_1 close to 0 in the supercritical case, we expect a to remain small and so we can then neglect the cubic term in our examination of the amplitude near the bifurcation point. Hence, in

the static case we are interested in solutions of the linear ODE

$$\mathscr{C}_2 \frac{\partial^2 a}{\partial \zeta^2} + \mathscr{C}_0 \gamma_1 a = 0, \tag{4.25}$$

which has general solution

$$a(\zeta) = c_1 \sin(\sqrt{\mathscr{C}_0 \mathscr{C}_2^{-1} \gamma_1}\zeta) + c_2 \cos(\sqrt{\mathscr{C}_0 \mathscr{C}_2^{-1} \gamma_1}\zeta). \tag{4.26}$$

On examination of the linear order of the periodic decomposition of the stream function found in (4.3), we see that the periodic behaviour is modulated by the changing amplitude. More precisely, through use of Euler's formula, we see that we can rewrite $\Psi^{(1)}$ as a sum of terms of the form

$$c e^{(\pm k_{\mathrm{cr}} \pm \sqrt{\mathscr{C}_0 \mathscr{C}_2^{-1} \gamma_1}\epsilon) i x} h^{(1,1)}(Y). \tag{4.27}$$

Thus, the change in wavenumber $\delta \coloneqq \epsilon^{-1}(k - k_{\mathrm{cr}})$ is related to the change in growth factor by the relation

$$\delta^2 = \frac{\mathscr{C}_0}{\mathscr{C}_2} \gamma_1. \tag{4.28}$$

We can compute the relationship between δ and γ_1 in an alternate manner by returning to the dispersion ratio. If we perturb (3.9) by changing γ as prescribed in (4.2) and k as $k = k_{\mathrm{cr}} + \epsilon\delta$, at second order in ϵ we obtain a closed form expression of the same form as (4.28). While it is computationally intractable to verify their equality analytically due to the form of $\mathscr{C}_0$ and $\mathscr{C}_1$, we can show their excellent agreement numerically.

4.2 Compression case

We can perform the same computations in the case of pure lateral compression. We perturb the critical compression ratio

$$\lambda = \lambda_{\mathrm{cr}}(1 + \epsilon^2 \lambda_1), \tag{4.29}$$

and take the same periodic decompositions (4.3). The Euler-Lagrange equations for the first mode at second order now read

$$\begin{aligned}\lambda_{\mathrm{cr}}^2\frac{\mathrm{d}^4 h_{\mathrm{f}}^{(2,1)}}{\mathrm{d}Y^4} - k^2(1+\lambda_{\mathrm{cr}}^4)\frac{\mathrm{d}^2 h_{\mathrm{f}}^{(2,1)}}{\mathrm{d}Y^2} + \lambda_{\mathrm{cr}}^2 k^4 h_{\mathrm{f}}^{(2,1)} = \\ -2ik(1+\lambda_{\mathrm{cr}}^4)\frac{\mathrm{d}^2 h_{\mathrm{f}}^{(1,1)}}{\mathrm{d}Y^2} + 4ik^3\lambda_{\mathrm{cr}}^2 h_{\mathrm{f}}^{(1,1)},\\ \lambda_{\mathrm{cr}}^2\frac{\mathrm{d}^4 h_{\mathrm{s}}^{(2,1)}}{\mathrm{d}Y^4} - k^2(1+\lambda_{\mathrm{cr}}^4)\frac{\mathrm{d}^2 h_{\mathrm{s}}^{(2,1)}}{\mathrm{d}Y^2} + \lambda_{\mathrm{cr}}^2 k^4 h_{\mathrm{s}}^{(2,1)} = \\ -2ik(1+\lambda_{\mathrm{cr}}^4)\frac{\mathrm{d}^2 h_{\mathrm{s}}^{(1,1)}}{\mathrm{d}Y^2} + 4ik^3\lambda_{\mathrm{cr}}^2 h_{\mathrm{s}}^{(1,1)},\end{aligned} \tag{4.30}$$

and the family of linear differential operators corresponding to (4.10) is given by

$$\mathcal{L}_{\mathrm{f}}^{(n)}[h] = \mathcal{L}_{\mathrm{s}}^{(n)}[h] \coloneqq \lambda_{\mathrm{cr}}^2\frac{\mathrm{d}^4 h}{\mathrm{d}Y^4} - (nk)^2(1+\lambda_{\mathrm{cr}}^4)\frac{\mathrm{d}^2 h}{\mathrm{d}Y^2} + \lambda_{\mathrm{cr}}^2(nk)^4 h. \tag{4.31}$$

The general solutions of the Euler-Lagrange equations at second order are given by

$$\begin{aligned}h_{\mathrm{f}}^{(2,1)}(Y) &= c_1^{(2,1)}e^{-k\lambda_{\mathrm{cr}}^{-1}Y} + c_2^{(2,1)}e^{k\lambda_{\mathrm{cr}}^{-1}Y} + c_3^{(2,1)}e^{-k\lambda_{\mathrm{cr}}Y} + c_4^{(2,1)}e^{k\lambda_{\mathrm{cr}}Y} + \mathscr{G}_{\mathrm{f}}^{(2,1)},\\ h_{\mathrm{s}}^{(2,1)}(Y) &= c_5^{(2,1)}e^{k\lambda_{\mathrm{cr}}^{-1}Y} + c_6^{(2,1)}e^{k\lambda_{\mathrm{cr}}Y} + \mathscr{G}_{\mathrm{s}}^{(2,1)},\end{aligned} \tag{4.32}$$

and

$$\begin{aligned}h_{\mathrm{f}}^{(2,2)}(Y) &= c_1^{(2,2)}e^{-2k\lambda_{\mathrm{cr}}^{-1}Y} + c_2^{(2,2)}e^{2k\lambda_{\mathrm{cr}}^{-1}Y} + c_3^{(2,2)}e^{-2k\lambda_{\mathrm{cr}}Y} + c_4^{(2,2)}e^{2k\lambda_{\mathrm{cr}}Y} + \mathscr{G}_{\mathrm{f}}^{(2,2)},\\ h_{\mathrm{s}}^{(2,2)}(Y) &= c_5^{(2,2)}e^{2k\lambda_{\mathrm{cr}}^{-1}Y} + c_6^{(2,2)}e^{2k\lambda_{\mathrm{cr}}Y} + \mathscr{G}_{\mathrm{s}}^{(2,2)},\end{aligned} \tag{4.33}$$

where each $\mathscr{G}$ is a scalar, nonlinear function of $k(\beta)$ and $\lambda_{\mathrm{cr}}(\beta)$. Repeating the previously detailed procedure for the third order equations yields an amplitude relation of the form

$$\frac{\partial^2 a}{\partial\tau^2} - \mathscr{C}_2\frac{\partial^2 a}{\partial\zeta^2} = \mathscr{C}_0\lambda_1 a + \mathscr{C}_1|a|^2 a. \tag{4.34}$$

Once more, supercritical solutions correspond to negative values of $\mathscr{C}_1$ (note that we are concerned with negative values of λ_1). Plots of the coefficients $\mathscr{C}_0$ and $\mathscr{C}_1$ are given in fig. 4.3.

We see that the transition from supercritical to subcritical behaviour with decreasing β occurs at $\beta_{\mathrm{ss}} \approx 0.571^{-1} \approx 1.75$, which corresponds to a critical compression ratio of $\lambda_{\mathrm{ss}} \approx 0.6747$. Our computed value of β_{ss} is close to, but differs slightly from the previously reported values of 1.74 (Cai and Fu, 1999) and 1.73

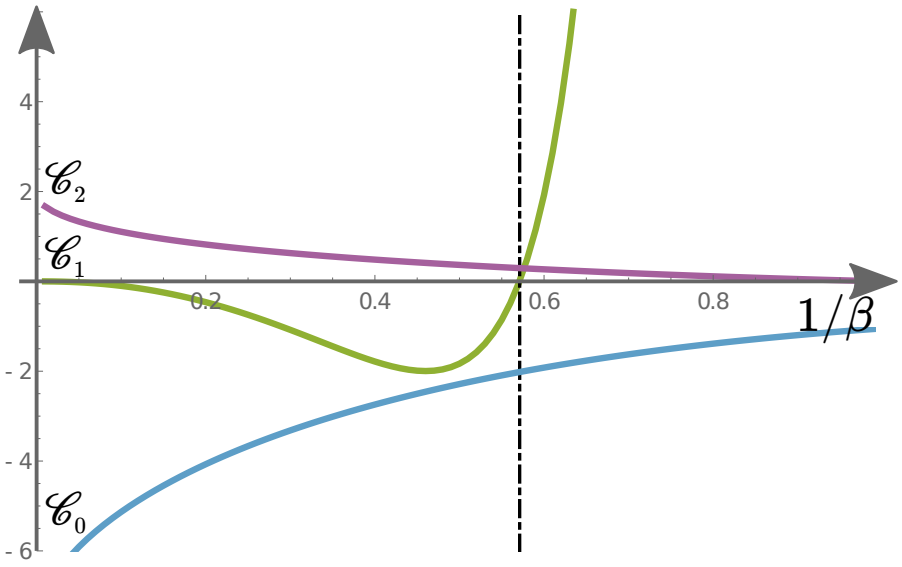


Figure 4.3: $\mathscr{C}_0$, $\mathscr{C}_1$ and $\mathscr{C}_2$ as functions of β^{-1} in the compression case

(Hutchinson, 2013). The difference may be due to a difference in the ansatz that we use (the base solutions are not strictly equivalent since we use a mixed-coordinates system). It should also be noted that the critical compression ratio agrees less well with the critical strain reported in creasing experiments. However, this is still consistent with these experimental observations—we show that when the wrinkling instability is stable, the critical strain required for wrinkling is always lower than the experimentally reported strain required for creasing.

We have now successfully characterised the behaviour of the wrinkling amplitude in the immediate post-buckling regime, but to probe the behaviour of solutions further past the bifurcation point, we turn to numerical tools.

This chapter is derived from Alawiye, Farrell, and Goriely (2020).

5 Numerical bifurcation analysis

Contents

5.1 Discretisation of the problem 67
5.2 Computation of bifurcation diagrams 69
5.3 Numerical results 71
5.3.1 Comparison of amplitude of numerical and analytical solutions 73
5.4 Direct computation of the primary bifurcation point . 73
5.4.1 Effect of computational domain aspect ratio 74

5.1 Discretisation of the problem

In addition to the analytical calculations presented above, we carried out a systematic program of numerical experiments to explore the post-buckling regime in the growth case. In contrast to the approach used above, these finite element method computations were carried out without the use of the stream function construction—while this made the analysis more tractable, the full nonlinearity it introduces into (2.16) makes it unattractive for discretisation. Instead, we adopted a mixed displacement-pressure formulation and imposed the incompressibility constraint with a Lagrange multiplier.

Another difference between the approaches comes from the nature of the domain. In our analytical calculations, we made use of a semi-infinite domain as an idealised model of the physical situation. Discretising such domains is subtle, so we choose to truncate it in the Y direction at some point. Various numerical studies (Cao and Hutchinson, 2012; Jin et al., 2015) suggest that a substrate ten times thicker than the film is sufficiently deep to negate any possible interaction between the bottom of the substrate and any wrinkles on the surface of the film as we expect the displacements to decay exponentially in the negative Y direction. Additionally, we must choose a boundary condition to apply to the bottom of the substrate, which we choose to be zero displacement (although zero traction might also be appropriate). On the sides of the domain, we allow the material to slide freely up the "walls" of the domain, but not to penetrate through them (the displacement in the X direction must vanish). A further difficulty arises from the width of the domain: in our analysis, we were able to choose this *a posteriori* to fit an integer number of wrinkles into it—a luxury we are not afforded in the numerical setting. We can inform our choice of domain size using the results of our perturbation analysis, but this will preclude us from independently verifying it.

Based on the above considerations, we restate our minimisation problem:

$$\underset{\substack{\mathbf{u}\in\boldsymbol{\Upsilon}\\ p\in L^2(\mathcal{B};\mathbb{R})}}{\text{minimise}} \quad I(\mathbf{u},p) \coloneqq \int_{\mathcal{B}} (\frac{\mu}{2}\det\mathbf{G})(\operatorname{tr}\mathbf{A}\mathbf{A}^T-2) - p(\det\mathbf{A}-1)\,\mathrm{d}\mathbf{X}. \tag{5.1}$$

where $\mathcal{B} = (-L, L) \times (-10, 1)$ for some $L > 0$, $\mathbf{G} = g\mathbf{1}$, $\mathbf{A} = \mathbf{1} + \frac{\partial \mathbf{u}}{\partial \mathbf{X}}$ and the set of admissible displacements is given by

$$\boldsymbol{\Upsilon} = \{\mathbf{u} \in H^1(\mathcal{B};\mathbb{R}^2) : \mathbf{u}(\cdot,-10) = (0,0),\, u(\pm L,\cdot) = 0\}, \tag{5.2}$$

where $\mathbf{u}(\mathbf{X}) = (u(X,Y), v(X,Y))$ and evaluation on the boundary is understood in the sense of traces. As usual, we compute solutions of (5.1) by solving the Euler-Lagrange equation

$$\delta I = 0, \tag{5.3}$$

varying in $\mathbf{u}$ and p simultaneously.

After unreported numerical experiments, we settled on using the Scott-Vogelius $(CG_k)^2 \times DG_{k-1}$ mixed finite element on an unstructured triangular mesh with a single iteration of barycentric mesh refinement applied to it, yielding a total of 141,730 degrees of freedom for each PDE solve for $k = 2$. The mesh was graded in such a way that the vast majority of resolution was concentrated in the film; the predicted exponential decay in the displacement in the substrate allowed for a very coarse mesh towards the bottom of the computational domain. The choice of finite element discretisation comes from both considerations of stability and effective imposition of the nonlinear incompressibility condition. Braess and Ming (2005) demonstrated that any pair of spaces that is stable for the Stokes problem will also be stable for incompressible hyperelasticity. The Scott-Vogelius element pair has been shown by Arnold and Qin (1992) to be stable for the 2D Stokes problem on barycentrically refined meshes for $k \geq 2$ and enjoys a number of advantageous properties (see Olshanskii and Rebholz (2011)) such as exact imposition of the divergence-free constraint found in the incompressible formulation of the problem. While achieving exact discrete enforcement of the nonlinear constraint in this formulation is not possible, we noted a two order of magnitude reduction in the constraint residual

$$\| \det \mathbf{A} - 1 \|_{L^2(\mathcal{B};\mathbb{R})}, \tag{5.4}$$

compared to the more common Taylor-Hood element. For a detailed exposition of the substantial effects that poor enforcement of the incompressibility constraint can have on the computation of bifurcation points for problems in elasticity, we refer to Auricchio et al. (2013).

5.2 Computation of bifurcation diagrams

We wish to understand the evolution of the solution set of the PDE as its parameters are varied. The main tool we apply is *deflated continuation*, an algorithm that advantageously combines two existing numerical techniques in nonlinear PDE analysis: *deflation* and *continuation*.

Deflation can be summarised as the positive answer to the following question:

> Given a solution z^* to a nonlinear PDE problem $\mathcal{F}$ on a Banach space Z, can we (under reasonable conditions) define a new problem $\mathcal{G}$ that satisfies the conditions below?
>
> 1. applying Newton's method to $\mathcal{G}$ will not yield z^*;
> 2. for $z \neq z^*$, z solves $\mathcal{F} \Leftrightarrow z$ solves $\mathcal{G}$.

This is achieved by systematically introducing singularities to the problem that will prevent the rediscovery of z^* by Newton's method. This technique was introduced in Farrell, Birkisson, and Funke (2015) as an adaptation of the approach presented in Brown and Gearhart (1971) for the solution of nonlinear algebraic equations.

Continuation methods are a classical tool in bifurcation analysis. Given a nonlinear equation

$$\mathcal{F}(z, \gamma) = 0, \tag{5.5}$$

with parameter $\gamma \in \mathbb{R}$, suppose we have found a solution z_0^* for a particular γ_0 and wish to now solve the equation for a slightly perturbed parameter value, say $\gamma_1 = \gamma_0 + \Delta\gamma$. There are several approaches to this problem, the most obvious of which is *zero-order continuation*. For this, we simply use z_0^* as the initial guess for the solution at $\gamma = \gamma_1$.

The two procedures are combined as follows. Given a bifurcation problem (5.5), we specify a range of parameter values $[\gamma_{\min}, \gamma_{\max}]$ of interest and a continuation step size $\Delta\gamma$. Then, starting from $\gamma = \gamma_{\min}$, we first perform zero-order continuation followed by deflation on each of the known solutions for the current value of γ. We then search for new solutions using Newton's method, with one initial guess for each of the previous solutions. If we find another solution, we can deflate it and repeat our search from the same initial guess until Newton's method fails to converge. Finally, we increment γ by $\Delta\gamma$ and repeat the whole process until we reach $\gamma_{\max}$. The main advantage of this approach is that it allows for the detection of disconnected branches, so long as they are close to known ones.

5.3 Numerical results

We discretised and numerically solved the Euler-Lagrange equation (5.3) using Firedrake (Rathgeber et al., 2016) and PETSc (Balay et al., 2019). We considered 19 values of the inverse stiffness ratio β^{-1} between 0.05 and 0.95. While the method is capable of computing unstable bifurcation branches, we did not explore the subcritical regime in depth due to the presence of spurious solutions in the discretised system for sufficiently low values of β. For each fixed value of β, we applied deflated continuation in γ for an appropriate subset of $[1, 1.6]$. We used a non-uniform spacing of values with the density of continuation points increasing with proximity to an asymptotic approximation of the critical growth value γ_{cr}. Each solve of the nonlinear PDE was performed using Newton's method, with the linear system arising at each Newton iteration solved using the sparse LU factorisation algorithm of MUMPS (Amestoy et al., 2001).

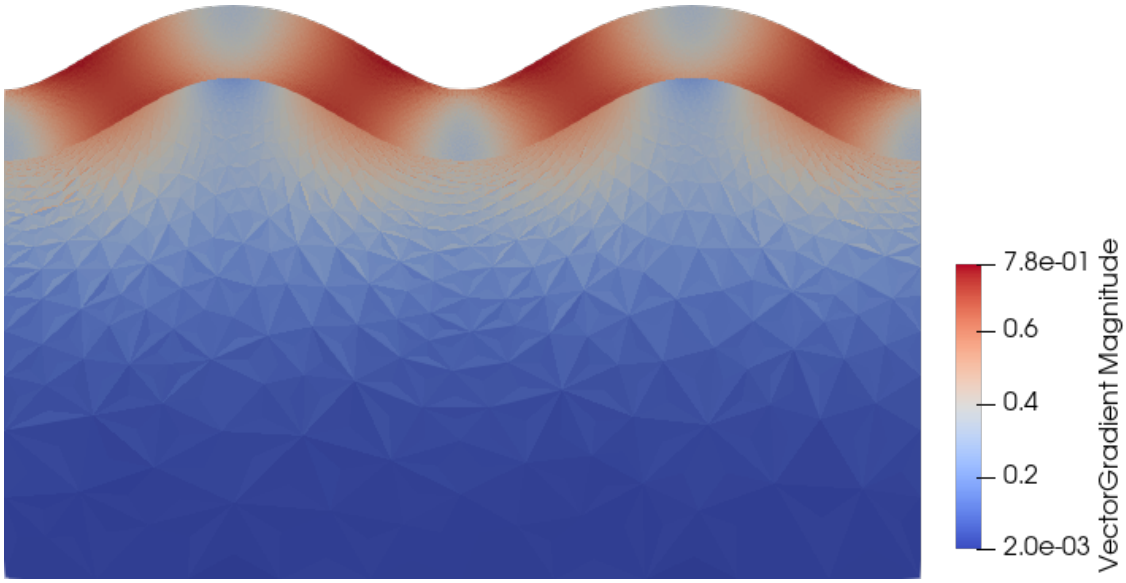


Figure 5.1: Example numerical wrinkling solution for $\beta = 4$, $\gamma = 1.303$ (colored by strain—we can see the mesh because the strain approximation is discontinuous)

We were able to discover the primary wrinkling bifurcation and continue solutions past the critical growth parameter for the full range of stiffness ratios considered. An example of a post-bifurcation wrinkling solution for an intermediate value of β is shown in fig. 5.1. For each stiffness ratio, we can then compute the

evolution of the observed wrinkling amplitude of the numerical solutions as γ is increased past γ_{cr} by computing

$$a_{\text{obs}} = \|v\|_{L^\infty(\{Y=1\};\mathbb{R})} - (\gamma^2 - 1), \tag{5.6}$$

where the $\gamma - 1$ term arises from the vertical displacement present in the uniform growth solution. This was then compared (see section 5.3.1) to the corresponding solutions of the static amplitude equation (4.22) (an example is shown in fig. 5.2) and found to be in excellent agreement with no fitting parameters in most cases. However, for some stiffness ratios we found that the bifurcation did not occur until slightly after the predicted critical value of γ (although the shape of the bifurcating branch remained correct). To investigate this phenomenon further, we turned to direct methods for determining where the first instance of a non-trivial solution branch occurs in the numerics.

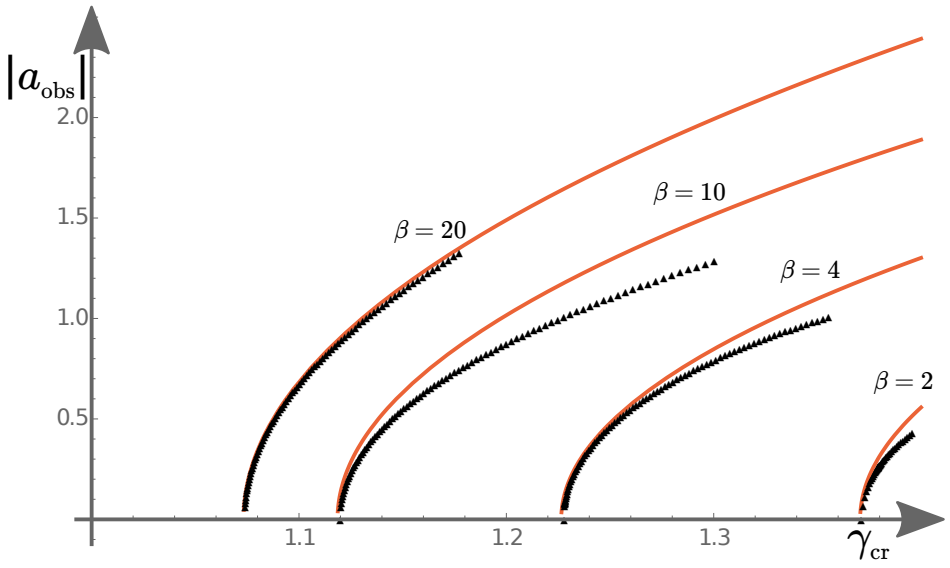


Figure 5.2: Observed amplitude of numerical solutions (black) and amplitude relation (4.22) (orange) for $\beta \in \{20, 10, 4, 2\}$. The amplitude relation (which is valid for a small perturbation of γ_{cr}) shows good agreement with the numerics well into the post-buckling regime.

5.3.1 Comparison of amplitude of numerical and analytical solutions

In order to compare the observed amplitude (5.6) with our analytical prediction, we recall that the vertical displacement can be computed from the stream function in the growth case by

$$v = y - Y = \frac{\partial \Psi}{\partial x} - Y. \tag{5.7}$$

Taking the first two terms of the perturbation expansion (4.1) and substituting in (4.3), we find that

$$v|_{Y=1} = \gamma^2 - 1 + \epsilon \left(ika(\epsilon x, \epsilon t) h^{(1,1)}(1) + \text{c.c.} \right) + O(\epsilon^2). \tag{5.8}$$

Substituting in the constant amplitude solutions (4.22), we then have

$$\begin{aligned} a_{\text{obs}} &= \|v\|_{L^\infty(\{Y=1\};\mathbb{R})} - (\gamma^2 - 1) \\ &= 2k \sqrt{\frac{\mathscr{C}_0(\gamma - \gamma_{\text{cr}})}{\mathscr{C}_1 \gamma_{\text{cr}}}} \left| h_{\text{f}}^{(1,1)}(1) \right| + O(\epsilon^2). \end{aligned} \tag{5.9}$$

which can be computed explicitly to produce figures such as fig. 5.2.

5.4 Direct computation of the primary bifurcation point

While the computations described in the previous section allow us to examine the post-buckling behaviour of the system past the bifurcation point, it is somewhat difficult to see precisely where the pitchfork begins. However, we can identify the bifurcation point of the discretised system by solving an extended set of equations known as the Moore-Spence system (introduced by Moore and Spence (1980) for the computation of turning points and adapted to pitchfork bifurcations by Werner and Spence (1984)).

The essential idea is to treat the bifurcation parameter γ in (5.5) as a variable we wish to solve for and augment the equation with the requirement that the derivative of the residual in the z direction is not invertible (and hence has a

nonzero eigenvector w with eigenvalue 0). Mathematically the combined system can be written as: find $z, \gamma, w \in Z \times \mathbb{R} \times Z$ such that

$$\mathcal{F}(z, \gamma) = 0, \tag{5.10a}$$

$$\mathcal{F}_z(z, \gamma)w = 0, \tag{5.10b}$$

$$\|w\| = 1. \tag{5.10c}$$

In order to solve a discretisation of this system using Newton's method, an initial guess must be carefully constructed. First, we solve (5.10a) for z using the following asymptotic approximation for γ_{cr} for our chosen value of β (see section 3.2.2 for its derivation):

$$\gamma_{\text{cr}}^2 \approx 1 + \frac{3^{2/3}}{2}\beta^{-2/3} + \frac{2 \cdot 3^{1/3}}{5}\beta^{-4/3} + \frac{201}{2800}\beta^{-2}. \tag{5.11}$$

We then use this computed z to solve the generalised eigenvalue problem

$$\mathcal{F}_z(z, \gamma)w = rw, \tag{5.12}$$

for the eigenmode w associated with the minimal eigenvalue r using the SLEPc (Hernandez, Roman, and Vidal, 2005) implementation of the Krylov-Schur algorithm (Stewart, 2001). We can then combine our approximate z, γ_{cr} and w to form an initial guess for Newton's method applied to the complete Moore-Spence system (5.10). This approach is extremely robust and Newton's method converges to the solution of (5.10) in 4 iterations.

5.4.1 Effect of computational domain aspect ratio

Due to the finite width of our computational domain and our enforcement of sliding boundary conditions on the vertical walls, we are constrained to only ever realise an integer number of wrinkling periods in the numerical solutions we find. This both makes it difficult to verify precisely the predictions regarding wavenumber from the linear analysis and has the effect of delaying the bifurcation slightly past the predicted critical growth threshold. To examine this effect more closely, we

can introduce an aspect ratio parameter α in order to transform the computational domain from width $2L$ to $2\alpha L$ while keeping the height of both layers the same. We apply the simple coordinate transform

$$\begin{aligned} X &= \alpha^{-1}\tilde{X} & Y &= \tilde{Y} \\ u(X,Y) &= \alpha^{-1}\tilde{u}(\tilde{X},\tilde{Y}) & v(X,Y) &= \tilde{v}(\tilde{X},\tilde{Y}), \end{aligned} \tag{5.13}$$

which gives us the deformation gradient relation

$$\begin{aligned} \frac{\partial\tilde{u}}{\partial\tilde{X}} &= \frac{\partial u}{\partial X} & \frac{\partial\tilde{u}}{\partial\tilde{Y}} &= \alpha\frac{\partial u}{\partial Y}, \\ \frac{\partial\tilde{v}}{\partial\tilde{X}} &= \alpha^{-1}\frac{\partial v}{\partial X} & \frac{\partial\tilde{v}}{\partial\tilde{Y}} &= \frac{\partial v}{\partial Y}. \end{aligned} \tag{5.14}$$

Using these relations, we can replace the appropriate terms in (5.1) to formulate a minimisation problem for the rescaled system. This approach carries the significant benefit of allowing us to perform solves for domains of different aspect ratios without the tedious process of re-meshing.

Equally, we can also use this rescaling with the discretised Moore-Spence system to efficiently examine the effect of domain width on the observed bifurcation point in the numerical system. Of particular interest is the observed wavenumber k_{obs} of a numerical wrinkling solution given by

$$k_{\text{obs}} \coloneqq \frac{(n_{\text{obs}}+1)\pi}{2L\alpha}, \tag{5.15}$$

where n_{obs} is the observed number of minima and maxima of the vertical displacement of the top surface of the domain (excluding the endpoints). Given a fixed stiffness ratio β and corresponding critical wavenumber k_{cr}, we can then compute the value of the aspect ratio α_n that would allow $(n+1)/2$ periods (or equivalently n interior extrema) of a sinusoidal profile with wavenumber k_{cr} to fit into the interval $[-\alpha L, \alpha L]$:

$$\alpha_n \coloneqq \frac{(n+1)\pi}{2Lk_{\text{cr}}}. \tag{5.16}$$

By solving the discretised Moore-Spence system for a range of values of α, we see that those which minimise the gap between the expected and realised value of γ_{cr} occur close to some α_n for an even value of n (see fig. 5.3 for an example). This

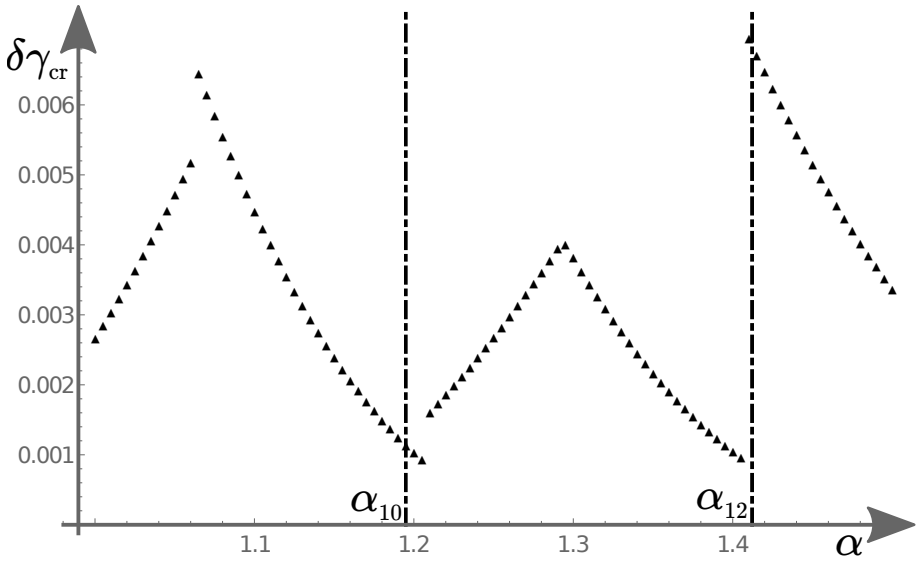


Figure 5.3: Error in computed bifurcation point as a function of aspect ratio α for $\beta = 2.5$

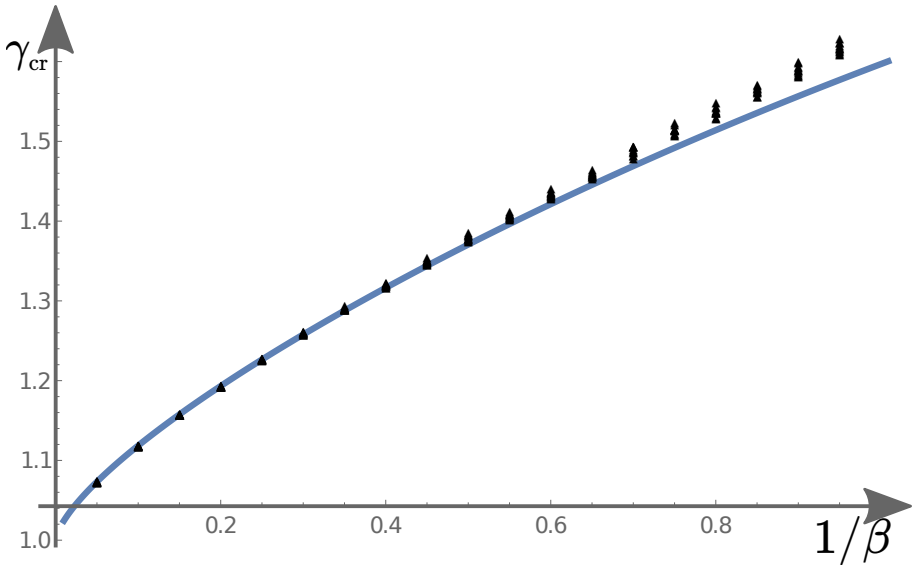


Figure 5.4: Computed critical growth factor as a function of β^{-1}. For each value of β considered, we performed the computations for 11 uniformly spaced aspect ratios $\alpha \in [1, 1.5]$ (all shown)

suggests that the delay in bifurcation is predominantly caused by the domain-width constraint. This effect is accentuated at lower values of β, as illustrated in fig. 5.4.

As hinted at in fig. 5.3, even with the optimal aspect ratio, there remains a small but significant difference between the expected and observed value of γ_{cr} for some values of β. Some of this can be explained by discretisation error and the domain

truncation that we carry out, but we have not yet performed a comprehensive analysis on whether we can explicitly account for all of the difference as a result of these factors. Nonetheless, our numerical experiments have provided a robust corroboration of our weakly-nonlinear analysis and given us further insight into the post-buckling behaviour of the system past the bifurcation point. In particular, the tools developed are easily adaptable to further numerical experiments such as different domain geometries or boundary conditions.

This chapter is derived from Alawiye, Farrell, and Goriely (2020).

6 Solutions of the amplitude relation

Contents

6.1 Hamiltonian form 79
6.2 Explicit solutions 82

The computations and comparisons featured in chapter 5 all relate to solutions with constant amplitude a. However, the decomposition (4.3) allowed for variations of the amplitude on far spatial and long temporal scales, ultimately yielding the nonlinear Klein-Gordon type amplitude equation (4.21). We now search for solutions of this nonlinear PDE, following the method set out by Lega and Goriely (1999).

6.1 Hamiltonian form

First, let us consider travelling wave solutions for which

$$a(\zeta, \tau) = \tilde{a}(\zeta - c\tau)e^{i\omega\tau}, \tag{6.1}$$

for some wave speed c and phase shift ω. Writing $\xi = \zeta - c\tau$, we then obtain

$$(\mathscr{C}_2 - c^2)\tilde{a}'' + 2ic\omega\tilde{a}' + (\mathscr{C}_0\gamma_1 + \omega^2)\tilde{a} + \mathscr{C}_1|\tilde{a}|^2\tilde{a} = 0. \tag{6.2}$$

This can be further transformed into a pair of real-valued equations by writing $\tilde{a}$ in polar form, i.e. $\tilde{a}(\xi) = r(\xi)e^{i\theta(\xi)}$, and taking real and imaginary parts of the resulting equation. Here it is useful to write the derivative of θ as Θ:

$$\begin{aligned}(\mathscr{C}_2 - c^2)r'' + \left(-2c\omega\Theta(\mathscr{C}_2 - c^2)\Theta^2 + \mathscr{C}_0\gamma_1 + \omega^2\right) r + \mathscr{C}_1 r^3 = 0,\\ -2\left((\mathscr{C}_2 - c^2)\Theta - c\omega\right) r' + (\mathscr{C}_2 - c^2)\Theta' r = 0.\end{aligned} \tag{6.3}$$

We can then find two first integrals of (6.3):

$$\begin{aligned}\Phi_1 &= c(\mathscr{C}_2 - c^2)\omega(r')^2 + (\mathscr{C}_2 - c^2)r^2\Theta(c\omega\Theta - \mathscr{C}_0\gamma_1 - \omega^2) + \frac{1}{2}c\mathscr{C}_1\omega r^4,\\ \Phi_2 &= -r^2\left((\mathscr{C}_2 - c^2)\Theta + c\omega\right).\end{aligned} \tag{6.4}$$

The latter equation can be rearranged to provide a closed form expression for Θ in terms of r:

$$\Theta = -\frac{\Phi_2 + c\omega r^2}{(\mathscr{C}_2 - c^2)r^2}. \tag{6.5}$$

The two first integrals can be combined to write down a useful conserved quantity

$$\Phi = \frac{(\mathscr{C}_2 - c^2)(\Phi_1 - \mathscr{C}_0\gamma_1\Phi_2) - (\mathscr{C}_2 + c^2)\Phi_2\omega^2}{c(\mathscr{C}_2 - c^2)^2\omega}. \tag{6.6}$$

In particular, we can interpret Φ as a Hamiltonian for the motion of a particle in a potential V_{eff} defined as follows:

$$\Phi - (r')^2 = v_{-2}r^{-2} + v_2 r^2 + v_4 r^4 =: V_{\text{eff}}, \tag{6.7}$$

where the coefficients v_i are given by:

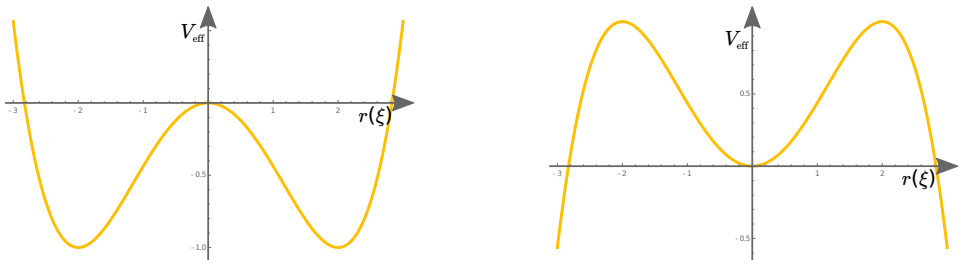
$$v_{-2} = \frac{\Phi_2^2}{(\mathscr{C}_2 - c^2)^2}, \qquad v_2 = \frac{\mathscr{C}_2(\mathscr{C}_0\gamma_1 + \omega^2) - c^2\mathscr{C}_0\gamma_1}{(\mathscr{C}_2 - c^2)^2}, \qquad v_4 = \frac{\mathscr{C}_1}{2(\mathscr{C}_2 - c^2)}. \tag{6.8}$$

Depending on the values of the parameters, the "potential" V_{eff} can take a number of different shapes (illustrated in figs. 6.1 and 6.2), only some of which support periodic orbits. Of particular importance in determining this are signs of v_2 and v_4 as well as whether v_{-2} vanishes. Let us restrict our attention to the static case ($c = \omega = 0$). We always have $\mathscr{C}_0 > 0$ and $\mathscr{C}_2 > 0$ and we see a sign change in $\mathscr{C}_1$ from negative for $\beta > \beta_{\text{ss}}$ to positive for $\beta < \beta_{\text{ss}}$. At the same point, we also

see a change in the sign of γ_1 from positive to negative as the system changes from supercritical to subcritical with decreasing β. The coefficients of V_{eff} are given by

$$v_{-2} = \frac{\Phi_2^2}{\mathscr{C}_2^2}, \qquad v_2 = \frac{\mathscr{C}_0\gamma_1}{\mathscr{C}_2}, \qquad v_4 = \frac{\mathscr{C}_1}{2\mathscr{C}_2}. \tag{6.9}$$

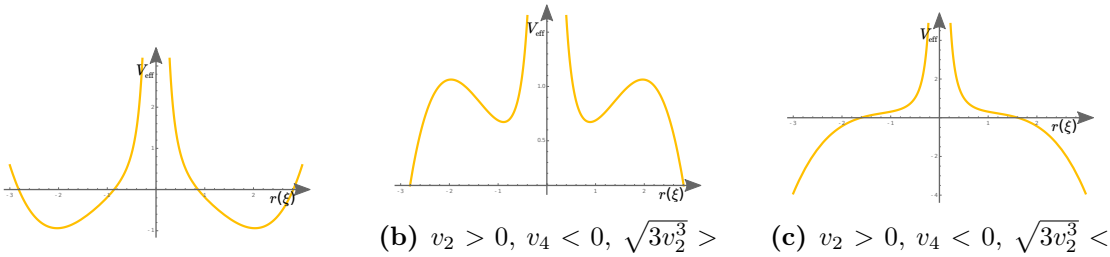
By considering the shape of V_{eff}, we see that if Φ_2 (and hence v_{-2}) vanishes, we can find localised solutions if and only if v_2 and v_4 have opposite sign. By the observations above, we see that this is always true.



(a) $v_2 < 0$, $v_4 > 0$ **(b)** $v_2 > 0$, $v_4 < 0$

Figure 6.1: Potentials for which v_{-2} vanishes

If Φ_2 is nonzero, we must have $v_2 > 0$, $v_4 < 0$ and $\sqrt{3v_2^3} + 9v_4 > 0$ in order to see such solutions, which immediately limits us to the supercritical case.



(a) $v_2 < 0$, $v_4 > 0$ **(b)** $v_2 > 0$, $v_4 < 0$, $\sqrt{3v_2^3} > -9v_4$ **(c)** $v_2 > 0$, $v_4 < 0$, $\sqrt{3v_2^3} < -9v_4$

Figure 6.2: Potentials for which v_{-2} does not vanish

In our efforts to better understand the subcritical case, let us focus on the case in which $v_{-2} = 0$, $v_2 < 0$ and $v_4 > 0$. localised solutions in such potentials consist of homoclinic orbits linking $\tilde{r} = 0$ to itself. The maximal value of r achieved in such orbits can easily be seen to be

$$r_{\max} = \sqrt{-\frac{v_2}{v_4}} = \sqrt{-\frac{2\mathscr{C}_0\gamma_1}{\mathscr{C}_1}}. \tag{6.10}$$

6.2 Explicit solutions

In order to compute explicit solutions, it is convenient to make the substitution

$$\tilde{r}(\xi) = -\left(\frac{v_2}{3} + v_4 r(\xi)^2\right). \tag{6.11}$$

The Hamiltonian (6.7) then becomes

$$(\tilde{r}')^2 = 4\tilde{r}^3 - g_2\tilde{r} - g_3, \tag{6.12}$$

where the *invariants* g_i are given by

$$g_2 = \frac{4}{3}(v_2^2 + 3\Phi v_4), \qquad g_3 = -\left(\frac{8v_2^3}{27} + \frac{4\Phi v_2 v_4}{3} + 4v_4^2 v_{-2}\right). \tag{6.13}$$

So long as $g_2^3 \neq 27g_3^2$, the general solution of (6.12) is given by

$$\tilde{r}(\xi) = \wp(\xi + \xi_0|\omega_1, \omega_3), \tag{6.14}$$

where $\wp$ is the Weierstrass elliptic function and ξ_0 is a constant of integration. To compute the *half periods* ω_i, let us label the roots of the cubic on the right hand side of (6.12) as e_1, e_2 and e_3 so that it reads

$$(\tilde{r}')^2 = 4(\tilde{r} - e_1)(\tilde{r} - e_2)(\tilde{r} - e_3). \tag{6.15}$$

If $g_2^3 > 27g_3^2$, all three roots are real and distinct. In this case, let us order them so that $e_1 > e_2 > e_3$. We then have

$$\begin{aligned}
\omega_1 &= \int_{e_1}^{\infty} \left(4\hat{r}^3 - g_2\hat{r} - g_3\right)^{-1/2} \mathrm{d}\hat{r}, \\
\omega_3 &= i\int_{e_3}^{\infty} \left(4\hat{r}^3 - g_2\hat{r} - g_3\right)^{-1/2} \mathrm{d}\hat{r}, \\
\omega_2 &= -(\omega_1 + \omega_3).
\end{aligned} \tag{6.16}$$

For a detailed review of the theory of elliptic functions in this context, refer to Whittaker and Watson (1920). Reversing the transformation (6.11), we can now write an expression for r:

$$r(\xi) = \sqrt{-\frac{v_2 + 3\wp(\xi + \xi_0|\omega_1, \omega_3)}{3v_4}}. \tag{6.17}$$

At this stage, we make the important observation that in the static case, the first integrals (6.4) are actually scalar multiples of one another:

$$\Phi_1 = -\mathscr{C}_0\mathscr{C}_2\gamma_1 r^2\Theta, \qquad \Phi_2 = -\mathscr{C}_2 r^2\Theta. \tag{6.18}$$

If Φ_2 vanishes, Φ_1 (and hence Φ) must also vanish and either $r \equiv 0$ or θ is constant (i.e. it just has the effect of a uniform phase shift). The vanishing of both Φ and Φ_2 means we now have $g_2^3 = 27g_3^2$ and $\omega_3 = \infty$. In this special case, the Weierstrass elliptic function and its imaginary half period ω_1 can be expressed in the following elementary fashion:

$$\wp(\xi|\omega_1,\infty) = \left(\frac{\pi}{2\omega_1}\right)^2\left(\frac{1}{\sin^2\left(\frac{\pi\xi}{2\omega_1}\right)} - \frac{1}{3}\right), \qquad \omega_1^2 = \frac{g_2\pi^2}{18g_3} = \frac{\mathscr{C}_2\pi^2}{4\mathscr{C}_0\gamma_1}. \tag{6.19}$$

We can now use (6.17) and (6.19) to write down an explicit form for a localised solution in the subcritical case $v_{-2} = 0, v_2 < 0, v_4 > 0$. Taking ξ_0 to be an odd multiple of ω_1 in (6.14) to ensure a real-valued solution, we then obtain

$$r(\xi) = \sqrt{-\frac{2\mathscr{C}_0\gamma_1}{\mathscr{C}_1}}\,\operatorname{sech}\left(\sqrt{-\frac{\mathscr{C}_0\gamma_1}{\mathscr{C}_2}}\xi\right). \tag{6.20}$$

Finally, we return to our perturbation expansion (4.1) and periodic decomposition (4.3) to realise mathematically the profile of a variable amplitude solution to our system, an example of which is shown graphically in fig. 6.3.

We conclude with the remark that it is not clear which non-constant solutions of the amplitude equation correspond to physically realisable wrinkling envelopes. Our suspicion is that this set consists of only the "pulse" solution given in (6.20), but this has yet to be confirmed.

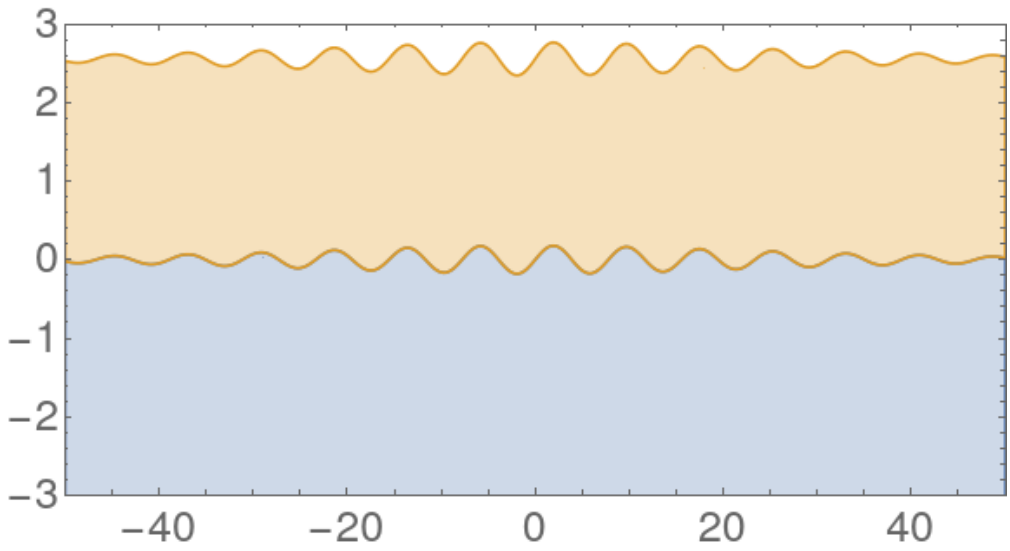


Figure 6.3: Profile of a subcritical variable amplitude solution for $\beta^{-1} = 1.01$, $\gamma = \gamma_{\mathrm{cr}} - 0.01^2$. Note that the aspect ratio is not 1:1

7 Epilogue

7.1 Summary

This thesis has given a detailed exposition of the post-buckling behaviour of an elastic film bonded to an elastic substrate and subjected to compressive stress induced by either growth of the film or lateral compression.

Chapter 1 presented a brief history of mathematical modelling of growth mechanics, an exposition of the theory of incremental deformation and a summary of how previous studies have used these elements to study growth-induced instabilities. This chapter provides context and motivation for how this thesis project came about and fixes notation for the rest of the document.

Chapter 2 presented a general formulation for the modelling of an incompressible hyperelastic bilayer subjected to film growth or lateral compression. A mixed coordinate formulation involving a stream function type construction was specified and the Euler-Lagrange equations and their boundary conditions were derived.

In chapter 3, this formulation was used to perform a linear bifurcation analysis to identify the critical values of the driving parameters that would permit the formation of a wrinkling instability in the bilayer. The asymptotic behaviour of these parameters was derived in the stiff-film limit and the effect of a number of additional physical effects on the critical parameters was considered.

Chapter 4 extended the linear analysis into the weakly-nonlinear regime by perturbing the critical parameters and solving the Euler-Lagrange equations of the systems at higher orders in the perturbation expansion. At third order, an amplitude equation that describes how the magnitude of surface oscillations increased past the critical growth factor was derived. Analysis of this equation also yielded a threshold value for the transition between a supercritical and subcritical bifurcation when the film becomes sufficiently soft relative to the substrate.

In chapter 5, the above analyses were corroborated by a numerical bifurcation analysis using a carefully chosen finite element discretisation. Good agreement with the post-buckling amplitude was demonstrated without the use of fitting parameters. A numerical scheme to directly compute the bifurcation point of the system was described and used to investigate the effect of domain aspect ratio on the observed value of the critical growth factor in the computations.

In chapter 6, qualitative behaviours of non-constant solutions to the amplitude equations were examined to give an explicit general solution in terms of an elliptic function and to realise a variable-amplitude solution of our system in the subcritical regime that features completely localised deformation.

7.2 Future work

Though the investigations in this thesis are in some sense self-contained, there are a number of immediate extensions that would naturally follow from the work contained within it.

7.2.1 Numerical realisation of variable amplitude solutions

As of yet, we have been unable to discover any variable amplitude solutions of the type discussed in chapter 6. It is likely that in order to realise such solutions numerically, one would have to carry out computations with a domain width much larger than that considered in chapter 5. Aside from the obvious increase in the degrees of freedom required to discretise a larger domain to the same degree of fineness, there is an additional cost associated with performing a numerical

bifurcation analysis on these larger domains. In our numerical experiments, it became apparent that various local alterations of a wrinkling deformation could often produce further solutions to the discretised Euler-Lagrange equations. Each of these localised variations could occur in a number of places, as demonstrated in fig. 7.1.

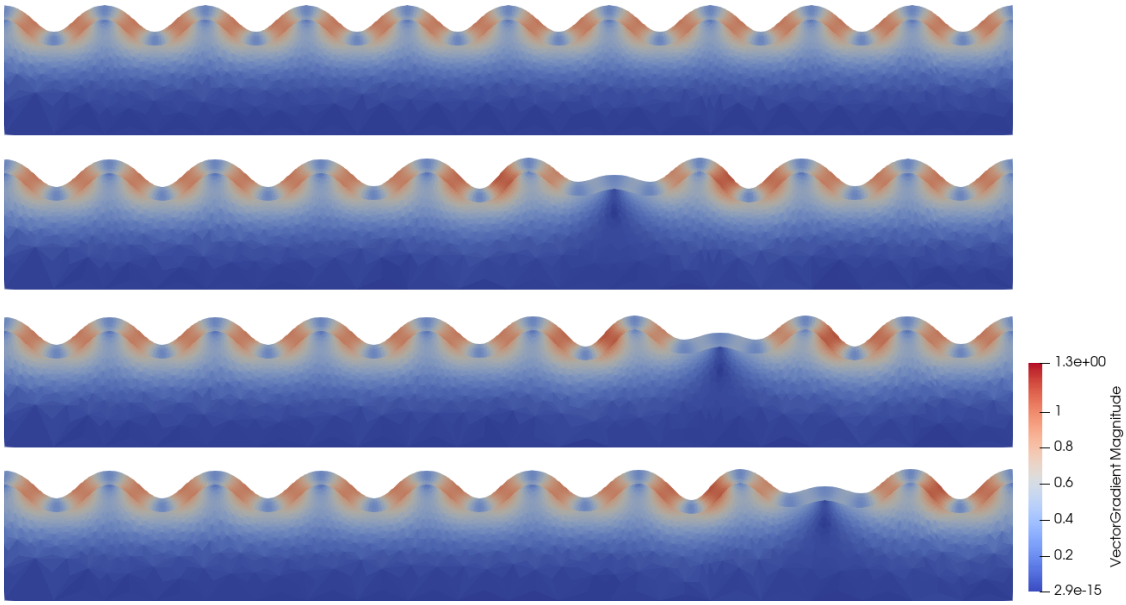


Figure 7.1: Example of the same localised alteration to a wrinkling solution in different places for $\gamma = 1.27$, $\beta = 10$.

This causes a combinatorial blowup in the number of solution branches present in wide domain, thus slowing the deflated continuation process down to a crawl. Future investigations could make use of large-scale computational resources in order to address this, or a more narrowly targeted bifurcation analysis algorithm.

7.2.2 Period-doubling

Another ongoing avenue of research is the study of the secondary period-doubling bifurcation that has been experimentally observed to occur in elastic bilayers with sufficiently stiff films (Pocivavsek et al., 2008; Brau et al., 2011). In their experiments, a stiff polymer film was bonded to a much softer gel or elastomer substrate and subjected to lateral compression. After sufficient compression, the wrinkling instability described in this thesis occurred as expected, but further increasing compression induced interesting post-buckling behaviour, as illustrated in fig. 7.2.

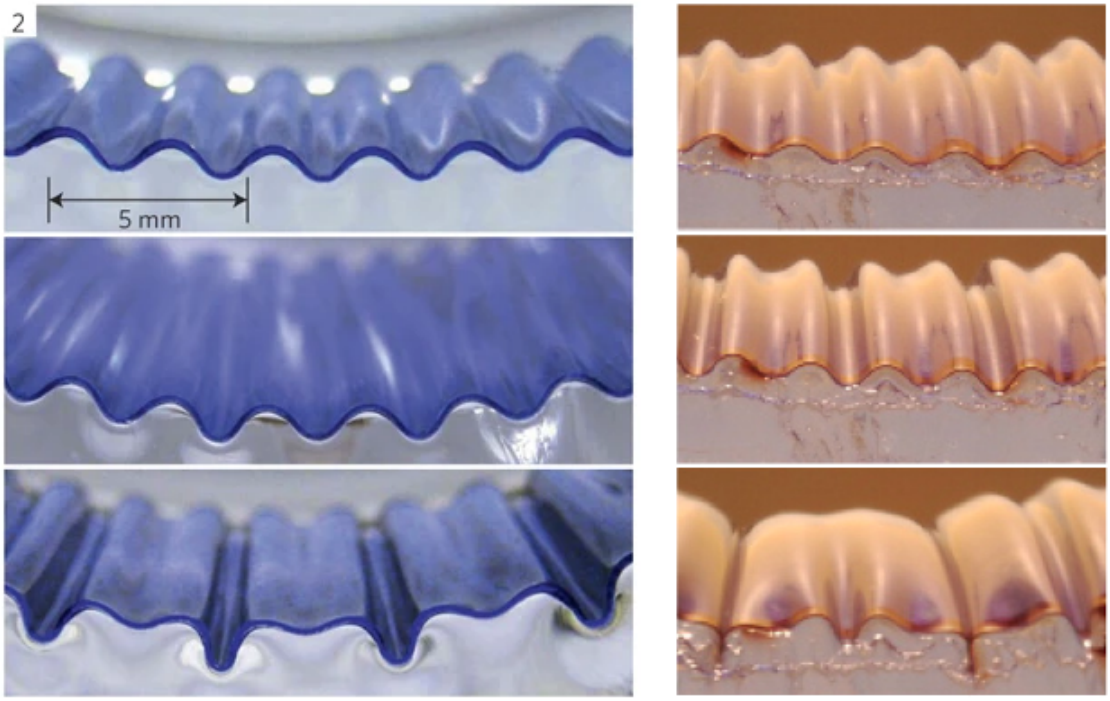


Figure 7.2: Experimental images demonstrating the evolution of a wrinkling instability into a period-doubling instability. Reproduced with permission from Pocivavsek et al. (2008) and Brau et al. (2011).

Reference	Model	Case	Method
Cao and Hutchinson, 2012	INH	comp.	commercial FE
Sun et al., 2012	CNH	comp.	commercial FE
Budday, Kuhl, and Hutchinson, 2015	CNH	growth	direct FE
Fu and Cai, 2015	INH	comp.	perturbation method
Cai and Fu, 2019	various	comp.	perturbation method

Table 7.1: Previous analyses of period-doubling in hyperelastic bilayers ("INH" and "CNH" denote incompressible and compressible neo-Hookean models respectively).

In a periodic fashion, some wrinkles grow in amplitude at the expense of their neighbours, resulting in a pattern consisting of the superposition of two periodic elements: a primary wrinkle with the original wavenumber k and a secondary, period-doubled wrinkle with wavenumber $k/2$. Mathematical analysis of this secondary bifurcation has proven difficult in the fully nonlinear elastic case, with notable contributions displayed in table 7.1.

Our numerical methods are able to realise period-doubled solutions and evolve them until the top surface is deeply folded and approaching self contact (illustrated

in fig. 7.3) through the deflated continuation procedure.

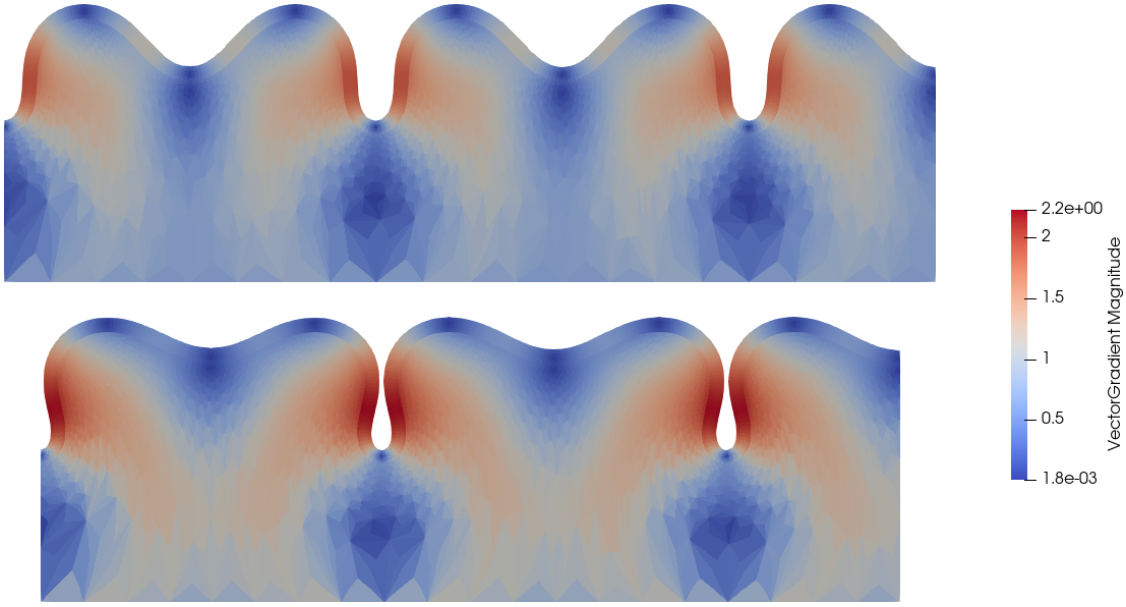


Figure 7.3: Period-doubled finite element solution in the compression case with $\beta = 100$, $\lambda = 0.6425$ (top). Further continuation to $\lambda = 0.5925$ brings the top surface into a deeply folded configuration approaching self contact (bottom).

We believe it should be possible to capture this bifurcation analytically in our stream function formulation, though we have not yet carried this out.

7.2.3 Creasing

As remarked in sections 1.2.5 and 4.1.1, the creasing instability remains poorly understood, with the literature featuring scant theoretical explanations for its occurrence and no rigorous numerical studies. Much of the difficulty surrounding this problem is the incidence of self-contact: while the class of admissible deformations in the minimisation problem of nonlinear elasticity ensures local invertibility by way of the orientation-preserving condition, this is not sufficient to ensure global injectivity of solutions. This was demonstrated in our own numerical investigations with softer films, as shown in fig. 7.4. In order to ensure global injectivity, one must verify the *Ciarlet-Nečas condition*

$$\int_{\mathcal{B}} \det \mathbf{F}(\mathbf{X}) \, \mathrm{d}\mathbf{X} \leq \operatorname{vol} \boldsymbol{\chi}(\mathcal{B}). \tag{7.1}$$

It is possible to prove necessary conditions on the solution of the minimisation problem with this additional condition by way of a modified boundary value problem (see Ciarlet (1987) for details), but it is not tractable to directly solve through either analytical or numerical means. Significant new theoretical work will be required before we are able to explicitly solve for self-contacting solutions in this framework.

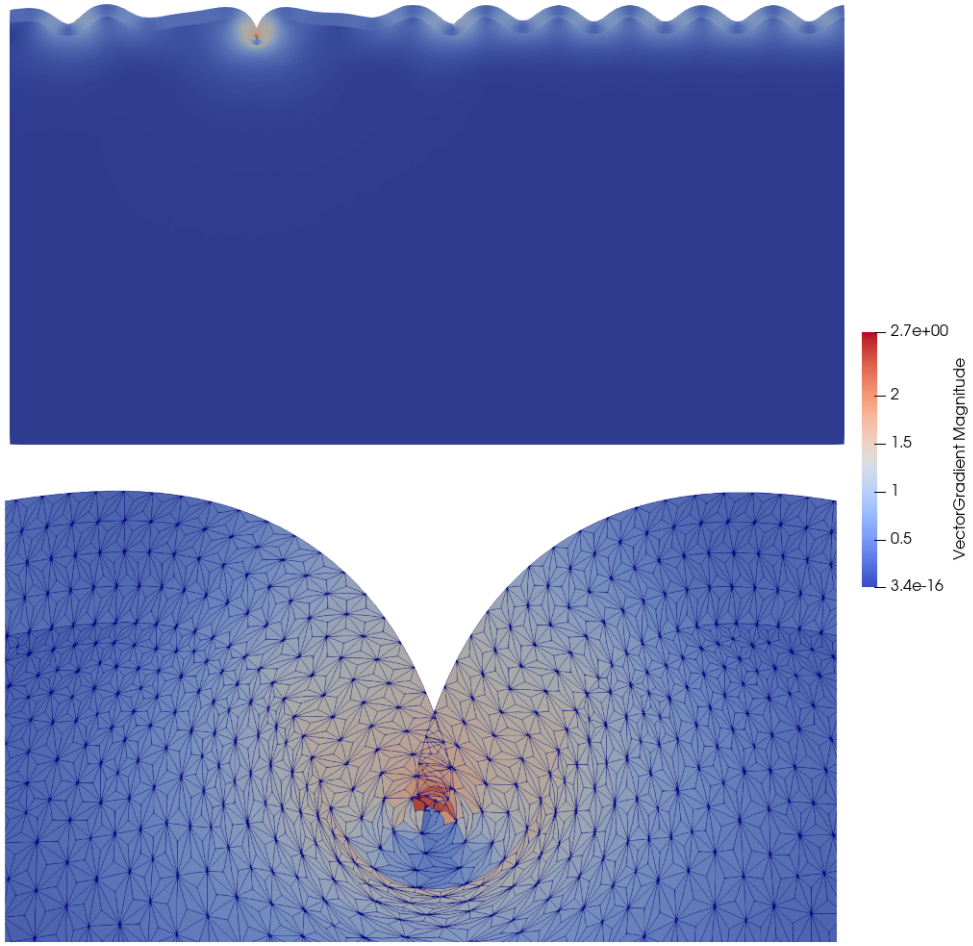


Figure 7.4: Self-intersecting numerical solution (top) with zoom detail (bottom) for $\beta = 5$, $\gamma \approx 1.3$.

7.2.4 Three dimensional models

One limitation of our work is the restriction of our analyses to the case of uniaxial compression in plane strain. The stream function approach does not easily generalise to the fully three-dimensional description required for the study of biaxial compression. In the closest analogous construction, two of the three coordinates

can be written as derivatives of a generating function as in the method employed in this manuscript, but the third can only be described implicitly, which greatly complicates the mathematical analysis. Recent progress has been made in works such as Cheewaruangroj and Biggins (2019) by analysis of the original equations, but this forgoes the benefits of exact imposition of the incompressibility constraint that the stream function formulation provides. While aspects of our analysis appear similar to previous works, we believe that a detailed post-bifurcation analysis validated with a dedicated numerical scheme is necessary for the further development of the field. In particular, outstanding questions regarding the long-time behaviour of the subcritical bifurcation branches remain open.

7.2.5 Remodelling and general growth laws

In the course of this work, we have only considered isotropic growth processes; that is to say those for which the growth tensor $\mathbf{G}$ is given by a constant multiple of the identity at any given point in the domain. While this allows us to capture all of the important phenomena of the wrinkling instability, there are many other growth tensors that could be considered. The formulation presented in chapter 2 is generalisable to arbitrary Y-dependent functions and there is no theoretical obstacle to the treatment of such growth tensors (and others) in the numerical schemes detailed in chapter 5. A simple anisotropy to consider might be one of the form

$$\mathbf{G} = \begin{pmatrix} g & 0 \\ 0 & g^{-1} \end{pmatrix}. \tag{7.2}$$

Here, the "growth" tensor does not actually change the volume of the material, but rather *remodels* it by organising its mass in some preferential direction. Remodelling processes are of great importance in many biological contexts, though in many cases they are driven by factors such as mechanical loading which greatly increase the mathematical complexity of the system. Nevertheless, we have performed preliminary numerical experiments (sampled in fig. 7.5) that demonstrate that the simple anisotropic growth law given in (7.2) can produce both the wrinkling instability and some more interesting morphologies that give immediate starting points for further theoretical study.

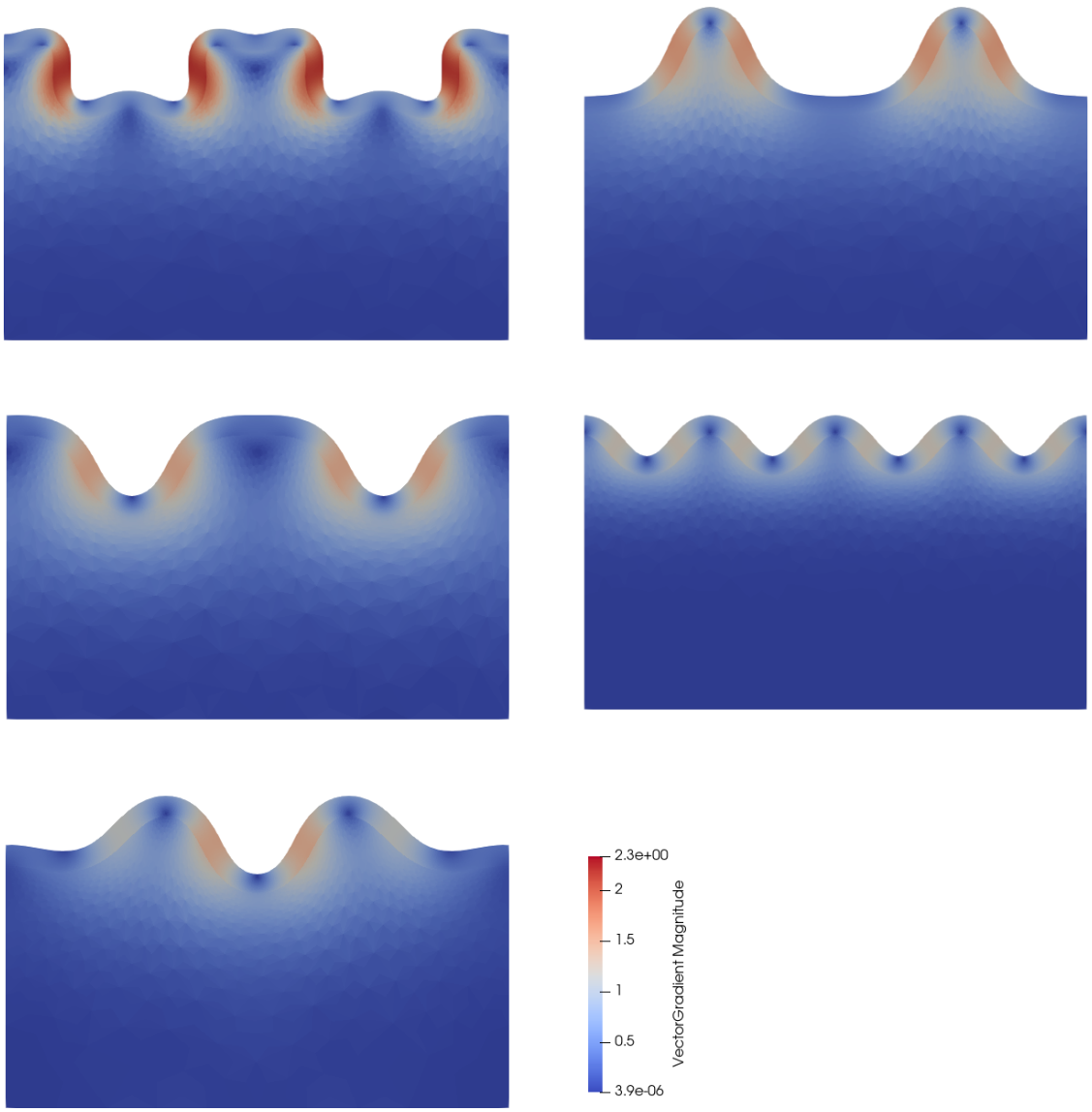


Figure 7.5: Morphologies in numerical solutions for the anisotropic growth tensor (7.2) with $\beta = 20$ and various $\gamma \in [1, 1.6]$.

Appendices

A
Boundary conditions

A.1 Regular case

The boundary conditions for the stream functions are

$$\lambda\frac{\partial^3\Psi_{\mathrm{f}}^{(1)}}{\partial Y^3}(x,1)+\lambda^{-1}(2\gamma^4+\lambda)\frac{\partial^3\Psi_{\mathrm{f}}^{(1)}}{\partial x^2\partial Y}(x,1)=0, \tag{A.1a}$$

$$\lambda\frac{\partial^2\Psi_{\mathrm{f}}^{(1)}}{\partial Y^2}(x,1)-\lambda^{-1}\gamma^4\frac{\partial^2\Psi_{\mathrm{f}}^{(1)}}{\partial x^2}(x,1)=0, \tag{A.1b}$$

$$\frac{\partial\Psi_{\mathrm{f}}^{(1)}}{\partial x}(x,0)-\frac{\partial\Psi_{\mathrm{s}}^{(1)}}{\partial x}(x,0)=0, \tag{A.1c}$$

$$\frac{\partial\Psi_{\mathrm{f}}^{(1)}}{\partial Y}(x,0)-\gamma^2\frac{\partial\Psi_{\mathrm{s}}^{(1)}}{\partial Y}(x,0)=0, \tag{A.1d}$$

$$\begin{aligned}\beta\left(\lambda\frac{\partial^3\Psi_{\mathrm{f}}^{(1)}}{\partial Y^3}(x,0)+\lambda^{-1}(2\gamma^4+\lambda^4)\frac{\partial^3\Psi_{\mathrm{f}}^{(1)}}{\partial x^2\partial Y}(x,0)\right)-\\ \gamma^4\left(\lambda\frac{\partial^3\Psi_{\mathrm{s}}^{(1)}}{\partial Y^3}(x,0)+\lambda^{-1}(2+\lambda^4)\frac{\partial^3\Psi_{\mathrm{s}}^{(1)}}{\partial x^2\partial Y}(x,0)\right)=0,\end{aligned} \tag{A.1e}$$

$$\begin{aligned}\beta\left(\lambda\frac{\partial^2\Psi_{\mathrm{f}}^{(1)}}{\partial Y^2}(x,0)-\gamma^4\lambda^{-1}\frac{\partial^2\Psi_{\mathrm{f}}^{(1)}}{\partial x^2}(x,0)\right)\\ -\gamma^2\left(\lambda\frac{\partial^2\Psi_{\mathrm{s}}^{(1)}}{\partial Y^2}(x,0)-\lambda^{-1}\frac{\partial^2\Psi_{\mathrm{s}}^{(1)}}{\partial x^2}(x,0)\right)=0,\end{aligned} \tag{A.1f}$$

$$\lim_{Y\to-\infty}\Psi_{\mathrm{s}}^{(1)}(x,Y)=0, \tag{A.1g}$$

$$\lim_{Y\to-\infty}\frac{\partial\Psi_{\mathrm{s}}^{(1)}}{\partial Y}(x,Y)=0. \tag{A.1h}$$

After substitution of $\Psi^{(1)}(x,Y) = \sin(kx)h^{(1)}(Y)$ for some $k > 0$, these boundary conditions read

$$\lambda\frac{\mathrm{d}^3 h_{\mathrm{f}}^{(1)}}{\mathrm{d}Y^3}(1) - k^2\lambda^{-1}(2\gamma^4+\lambda^4)\frac{\mathrm{d}h_{\mathrm{f}}^{(1)}}{\mathrm{d}Y}(1) = 0, \tag{A.2a}$$

$$\lambda\frac{\mathrm{d}^2 h_{\mathrm{f}}^{(1)}}{\mathrm{d}Y^2}(1) + k^2\gamma^4\lambda^{-1}h_{\mathrm{f}}^{(1)}(1) = 0, \tag{A.2b}$$

$$h_{\mathrm{f}}(0) - h_{\mathrm{s}}(0) = 0, \tag{A.2c}$$

$$\frac{\mathrm{d}h_{\mathrm{f}}^{(1)}}{\mathrm{d}Y}(0) - \gamma^2\frac{\mathrm{d}h_{\mathrm{s}}^{(1)}}{\mathrm{d}Y}(0) = 0, \tag{A.2d}$$

$$\begin{aligned}\beta\left(\lambda\frac{\mathrm{d}^3 h_{\mathrm{f}}^{(1)}}{\mathrm{d}Y^3}(0) - k^2\lambda^{-1}(2\gamma^4+\lambda^4)\frac{\mathrm{d}h_{\mathrm{f}}^{(1)}}{\mathrm{d}Y}(0)\right)\\ - \gamma^4\left(\lambda\frac{\mathrm{d}^3 h_{\mathrm{s}}^{(1)}}{\mathrm{d}Y^3}(0) - k^2\lambda^{-1}(2+\lambda^4)\frac{\mathrm{d}h_{\mathrm{s}}^{(1)}}{\mathrm{d}Y}(0)\right) = 0,\end{aligned} \tag{A.2e}$$

$$\beta\left(\lambda\frac{\mathrm{d}^2 h_{\mathrm{f}}^{(1)}}{\mathrm{d}Y^2}(0) + k^2\gamma^4\lambda^{-1}h_{\mathrm{f}}^{(1)}(0)\right) - \gamma^2\left(\lambda\frac{\mathrm{d}^2 h_{\mathrm{s}}^{(1)}}{\mathrm{d}Y^2}(0) + k^2\lambda^{-1}h_{\mathrm{s}}^{(1)}(0)\right) = 0, \tag{A.2f}$$

$$\lim_{Y\to-\infty} h_{\mathrm{s}}^{(1)}(Y) = 0, \tag{A.2g}$$

$$\lim_{Y\to-\infty} \frac{\mathrm{d}h_{\mathrm{s}}^{(1)}}{\mathrm{d}Y}(Y) = 0. \tag{A.2h}$$

A.2 Boundary conditions for an upper substrate

In the presence of an upper layer, the boundary conditions must be transformed as follows with boundary conditions given by

$$h_{\mathrm{f}}(1) - h_{\mathrm{t}}(1) = 0, \tag{A.3a}$$

$$\frac{\mathrm{d}h_{\mathrm{f}}^{(1)}}{\mathrm{d}Y}(1) - \gamma^2 \frac{\mathrm{d}h_{\mathrm{t}}^{(1)}}{\mathrm{d}Y}(1) = 0, \tag{A.3b}$$

$$\beta_{\mathrm{f}} \left(\lambda^2 \frac{\mathrm{d}^3 h_{\mathrm{f}}^{(1)}}{\mathrm{d}Y^3}(1) - k^2(2\gamma^4 + \lambda^4) \frac{\mathrm{d}h_{\mathrm{f}}^{(1)}}{\mathrm{d}Y}(1) \right) - \beta_{\mathrm{t}}\gamma^4 \left(\lambda^2 \frac{\mathrm{d}^3 h_{\mathrm{t}}^{(1)}}{\mathrm{d}Y^3}(1) - k^2(2 + \lambda^4) \frac{\mathrm{d}h_{\mathrm{t}}^{(1)}}{\mathrm{d}Y}(1) \right) = 0, \tag{A.3c}$$

$$\beta_{\mathrm{f}} \left(\lambda^2 \frac{\mathrm{d}^2 h_{\mathrm{f}}^{(1)}}{\mathrm{d}Y^2}(1) + k^2\gamma^2 h_{\mathrm{f}}^{(1)}(1) \right) - \beta_{\mathrm{t}}\gamma^2 \left(\lambda^2 \frac{\mathrm{d}^2 h_{\mathrm{t}}^{(1)}}{\mathrm{d}Y^2}(1) + k^2 h_{\mathrm{t}}^{(1)}(1) \right) = 0, \tag{A.3d}$$

$$\lim_{Y \to \infty} h_{\mathrm{t}}^{(1)}(Y) = 0, \tag{A.3e}$$

$$\lim_{Y \to \infty} \frac{\mathrm{d}h_{\mathrm{t}}^{(1)}}{\mathrm{d}Y}(Y) = 0, \tag{A.3f}$$

$$h_{\mathrm{f}}(0) - h_{\mathrm{s}}(0) = 0, \tag{A.3g}$$

$$\frac{\mathrm{d}h_{\mathrm{f}}^{(1)}}{\mathrm{d}Y}(0) - \gamma^2 \frac{\mathrm{d}h_{\mathrm{s}}^{(1)}}{\mathrm{d}Y}(0) = 0, \tag{A.3h}$$

$$\beta_{\mathrm{f}} \left(\lambda^2 \frac{\mathrm{d}^3 h_{\mathrm{f}}^{(1)}}{\mathrm{d}Y^3}(0) - k^2(2\gamma^4 + \lambda^4) \frac{\mathrm{d}h_{\mathrm{f}}^{(1)}}{\mathrm{d}Y}(0) \right) - \gamma^4 \left(\lambda^2 \frac{\mathrm{d}^3 h_{\mathrm{s}}^{(1)}}{\mathrm{d}Y^3}(0) - k^2(2 + \lambda^4) \frac{\mathrm{d}h_{\mathrm{s}}^{(1)}}{\mathrm{d}Y}(0) \right) = 0, \tag{A.3i}$$

$$\beta_{\mathrm{f}} \left(\lambda^2 \frac{\mathrm{d}^2 h_{\mathrm{f}}^{(1)}}{\mathrm{d}Y^2}(0) + k^2\gamma^2 h_{\mathrm{f}}^{(1)}(0) \right) - \gamma^2 \left(\lambda^2 \frac{\mathrm{d}^2 h_{\mathrm{s}}^{(1)}}{\mathrm{d}Y^2}(0) + k^2 h_{\mathrm{s}}^{(1)}(0) \right) = 0, \tag{A.3j}$$

$$\lim_{Y \to -\infty} h_{\mathrm{s}}^{(1)}(Y) = 0, \tag{A.3k}$$

$$\lim_{Y \to -\infty} \frac{\mathrm{d}h_{\mathrm{s}}^{(1)}}{\mathrm{d}Y}(Y) = 0. \tag{A.3l}$$

B
Software availability

At various points during the course of this work we have made reference to the particular form of some expressions being too lengthy to write in full. In the interests of our results being reproducible by others, we have archived a copy of the Mathematica code used to perform the analyses described in chapters 3 and 4. It is available for perusal at (Alawiye, 2020).

References

Alawiye, H. (2020). *WrinklingRevisited*. Version 1.0.0. URL: https://doi.org/10.5281/zenodo.3993418.

Alawiye, H., P. E. Farrell, and A. Goriely (2020). "Revisiting the wrinkling of elastic bilayers II: post-bifurcation analysis". In: *Journal of the Mechanics and Physics of Solids* 143, p. 104053.

Alawiye, H., E. Kuhl, and A. Goriely (2019). "Revisiting the wrinkling of elastic bilayers I: Linear analysis". In: *Philosophical Transactions of the Royal Society A* 377, p. 20180076.

Allen, H. G. (1969). *Analysis and Design of Structural Sandwich Panels*. Pergamon Press.

Ambrosi, D. et al. (2011). "Perspectives on biological growth and remodeling". In: *Journal of the Mechanics and Physics of Solids* 59.4, pp. 863–883.

Amestoy, P. R. et al. (2001). "A Fully Asynchronous Multifrontal Solver Using Distributed Scheduling". In: *SIAM Journal on Matrix Analysis and Applications* 23.1, pp. 15–41.

Arnold, D. N. and J. Qin (1992). "Quadratic Velocity/Linear Pressure Stokes Elements". In: *Advances in Computer Methods for Partial Differential Equations VII*. IMACS, pp. 28–34.

Asally, M. et al. (2012). "Localized cell death focuses mechanical forces during 3D patterning in a biofilm". In: *Proceedings of the National Academy of Sciences of the United States of America* 109.46, pp. 18891–18896.

Audoly, B. and A. Boudaoud (2008). "Buckling of a stiff film bound to a compliant substrate—Part I: Formulation, linear stability of cylindrical patterns, secondary bifurcations". In: *Journal of the Mechanics and Physics of Solids* 56.7, pp. 2401–2421.

Auricchio, F. et al. (2013). "Approximation of incompressible large deformation elastic problems: some unresolved issues". In: *Computational Mechanics* 52, pp. 1153–1167.

Balay, S. et al. (2019). *PETSc Users Manual*. Tech. rep. ANL-95/11 - Revision 3.11. Argonne National Laboratory. URL: http://www.mcs.anl.gov/petsc.

Barnette, A. R. et al. (2009). "Characterization of Brain Development in the Ferret *via* MRI". In: *Pediatric Research* 66, pp. 80–84.

Bayly, P. V., L. A. Taber, and C. D. Kroenke (2014). "Mechanical forces in cerebral cortical folding: A review of measurements and models". In: *Journal of the Mechanical Behaviour of Biomedical Materials* 29, pp. 568–581.

Bayly, P. V. et al. (2013). "A cortical folding model incorporating stress-dependent growth explains gyral wavelengths and stress patterns in the developing brain". In: *Physical Biology* 10.1.

Bella, P. and R. V. Kohn (2017). "Wrinkling of a thin circular sheet bonded to a spherical substrate". In: *Philosophical Transactions of the Royal Society A* 375.2093.

Ben Amar, M. and A. Bordner (2017). "Mimicking cortex convolutions through the wrinkling of growing soft bilayers". In: *Journal of Elasticity* 129.1–2, pp. 213–238.

Ben Amar, M. and P. Ciarletta (2010). "Swelling instability of surface-attached gels as a model of soft tissue growth under geometric constraints". In: *Journal of the Mechanics and Physics of Solids* 58.7, pp. 935–954.

Ben Amar, M. and A. Goriely (2005). "Growth and instability in elastic tissues". In: *Journal of the Mechanics and Physics of Solids* 53, pp. 2284–2319.

Ben Amar, M. and F. Jia (2013). "Anisotropic growth shapes intestinal tissues during embryogenesis". In: *Proceedings of the National Academy of Sciences of the United States of America* 110.26, pp. 10525–10530.

Biot, M. A. (1937). "Bending of an Infinite Beam on an Elastic Foundation". In: *Journal of Applied Mechanics*.

— (1963). "Surface instability of rubber in compression". In: *Applied Scientific Research, Section A* 12.2, pp. 168–182.

— (1965). *Mechanics of Incremental Deformation*. John Wiley & Sons, Inc.

Boffi, D., F. Brezzi, and M. Fortin (2013). *Mixed Finite Element Methods and Applications*. 1st ed. Vol. 44. Springer Series in Computational Mathematics. Springer-Verlag Berlin Heidelberg.

Bowden, N. et al. (1998). "Spontaneous formation of ordered structures in thin films of metals supported on an elastomeric polymer". In: *Nature* 393, pp. 146–149.

Braess, D. and P. Ming (2005). "A finite element method for nearly incompressible elasticity problems". In: *Mathematics of Computation* 74.249, pp. 25–52.

Brau, F. et al. (2011). "Multiple-length-scale elastic instability mimics parametric resonance of nonlinear oscillators". In: *Nature Physics* 7.1, pp. 56–60.

Brenner, S. C. and L. R. Scott (2008). *The Mathematical Theory of Finite Elements*. 3rd ed. Vol. 15. Texts in Applied Mathematics. Springer-Verlag New York.

Brown, K. M. and W. B. Gearhart (1971). "Deflation techniques for the calculation of further solutions of a nonlinear system". In: *Numerische Mathematik* 16.4, pp. 334–342.

Budday, S., E. Kuhl, and J. W. Hutchinson (2015). "Period-doubling and period-tripling in growing bilayered systems". In: *Philosophical Magazine* 95.28–30, pp. 3208–3224.

Budday, S., P. Steinmann, and E. Kuhl (2014). "The role of mechanics during brain development". In: *Journal of the Mechanics and Physics of Solids* 72, pp. 75–82.

Budday, S. et al. (2015). "Size and curvature regulate pattern selection in the mammalian brain". In: *Extreme Mechanics Letters* 4, pp. 193–198.

Cai, S. et al. (2012). "Creasing instability of elastomer films". In: *Soft Matter* 8, pp. 1301–1304.

Cai, Z. X. and Y. B. Fu (1999). "On the imperfection sensitivity of a coated elastic half-space". In: *Proceedings of the Royal Society of London A*, pp. 3285–3309.

— (2019). "Effects of pre-stretch, compressibility and material constitution on the period-doubling secondary bifurcation of a film/substrate bilayer". In: *International Journal of Non-Linear Mechanics* 115, pp. 11–19.

Cao, C. et al. (2014). "Harnessing Localized Ridges for High-Aspect-Ratio Hierarchical Patterns with Dynamic Tunability and Multifunctionality". In: *Advanced Materials* 26, pp. 1763–1770.

Cao, Y.-P. and J. W. Hutchinson (2011). "From wrinkles to creases in elastomers: the instability and imperfection-sensitivity of wrinkling". In: *Proceedings of the Royal Society A* 468.2137, pp. 94–115.

— (2012). "Wrinkling Phenomena in Neo-Hookean Film/Substrate Bilayers". In: *Journal of Applied Mechanics* 79.3.

Cauchy, A. L. (1823). "Recherches sur l'équilibre et le mouvement intérieur des corps solides ou fluides, élastiques ou non élastiques". In: *Bulletin de la Société Philomatique*, pp. 9–13.

— (1827). "De la pression ou tension dans un corps solide". In: *Exercises de Mathématiques* 2, pp. 42–56.

Cheewaruangroj, N. and J. S. Biggins (2019). "Pattern selection when a layer buckles on a soft substrate". In: *Soft Matter* 15, pp. 3751–3770.

Chung, J. Y., A. J. Nolte, and C. M. Stafford (2011). "Surface Wrinkling: A Versatile Platform for Measuring Thin-Film Properties". In: *Advanced Materials* 23, pp. 349–368.

Ciarlet, P. G. (1987). *Mathematical Elasticity Volume I: Three Dimensional Elasticity*. Vol. 20. Studies in mathematics and its applications. Elsevier Science Publishers B.V.

— (1997). *Mathematical Elasticity Volume II: Theory of Plates*. Vol. 27. Studies in mathematics and its applications. Elsevier Science B.V.

Ciarletta, P. (2018). "Matched asymptotic solution for crease nucleation in soft solids". In: *Nature Communications* 9.

Ciarletta, P., V. Balbi, and E. Kuhl (2014). "Pattern Selection in Growing Tubular Tissues". In: *Physical Review Letters* 113.24, p. 248101.

Ciarletta, P. and M. Ben Amar (2012). "Papillary networks in the dermal-epidermal junction of skin: a biomechanical model". In: *Mechanics Research Communications* 42, pp. 68–76.

Ciarletta, P. and Y. B. Fu (2015). "A semi-analytical approach to Biot instability in a growing layer: Strain gradient correction, weakly non-linear analysis and imperfection sensitivity". In: *International Journal of Non-Linear Mechanics* 75, pp. 38–45.

Ciarletta, P. and L. Truskinovsky (2019). "Soft Nucleation of an Elastic Crease". In: *Physical Review Letters* 122, p. 248001.

Diab, M. and K.-S. Kim (2014). "Ruga-formation instabilities of a graded stiffness boundary layer in a neo-Hookean solid". In: *Proceedings of the Royal Society A* 470, p. 20140218.

Euler, L. (1744). *Methodus Inveniendi Lineas Curvas Maximi Minimive proprietate gaudentes, sive Solutio Problematis Isoperimetrici Latissimo sensu accepti*. Apud Marcum-Michaelem Bousquet & Socios.

Evans, L. C. (2010). *Partial Differential Equations*. 2nd ed. Vol. 19. Graduate Studies in Mathematics. American Mathematical Society.

Farrell, P. E. (2020). *Finite Element Methods for PDEs*. Lecture notes. University of Oxford.

Farrell, P. E., Á. Birkisson, and S. W. Funke (2015). "Deflation Techniques for Finding Distinct Solutions of Nonlinear Partial Differential Equations". In: *SIAM Journal on Scientific Computing* 37.4, A2026–A2045.

Fu, Y. B. (2001). "Perturbation methods and nonlinear stability analysis". In: *Nonlinear Analysis: Theory and Applications*. Vol. 283. London Mathematical Society Lecture Note Series. Cambridge University Press, pp. 345–391.

Fu, Y. B. and Z. X. Cai (2015). "An asymptotic analysis of the period-doubling secondary bifurcation in a film/substrate bilayer". In: *SIAM Journal on Applied Mathematics* 75.6, pp. 2381–2395.

Fu, Y. B. and P. Ciarletta (2015). "Buckling of a coated elastic half-space when the coating and substrate have similar material properties". In: *Proceedings of the Royal Society of London A* 471.2178.

Fu, Y. B. and R. W. Ogden (1999). "Nonlinear stability analysis of pre-stressed elastic bodies". In: *Continuum Mechanics and Thermodynamics* 11, pp. 141–172.

Galilei, G. (1638). *Discorsi e Dimostrazioni Matematiche intorno a due nuove scienze: attenenti alla Mechanica & i Movimenti Locali*. In Leida.

Garcia, K. E. et al. (2018). "Dynamic patterns of cortical expansion during folding of the preterm human brain". In: *Proceedings of the National Academy of Sciences of the United States of America* 115.12, pp. 3156–3161.

Garikipati, K. (2009). "The Kinematics of Biological Growth". In: *Applied Mechanics Reviews* 62.3, p. 030801.

Goriely, A. (2017). *The Mathematics and Mechanics of Biological Growth*. Vol. 45. Interdisciplinary Applied Mathematics. Springer-Verlag New York.

Goriely, A., M. Nizette, and M. Tabor (2001). "On the Dynamics of Elastic Strips". In: *Journal of Nonlinear Science* 11, pp. 3–45.

Goriely, A. and M. Tabor (2013). "Rotation, inversion and perversion in anisotropic elastic cylindrical tubes and membranes". In: *Proceedings of the Royal Society of London A* 469.2153.

Goriely, A. et al. (2015). "Mechanics of the brain: perspectives, challenges and opportunities". In: *Biomechanics and Modeling in Mechanobiology* 14.5, pp. 931–965.

Hernandez, V., J. E. Roman, and V. Vidal (2005). "SLEPc: A scalable and flexible toolkit for the solution of eigenvalue problems". In: *ACM Transactions on Mathematical Software* 31.3, pp. 351–362.

Hill, R. S. and C. A. Walsh (2005). "Molecular insights into human brain evolution". In: *Nature* 437, pp. 64–67.

Hohlfeld, E. (2013). "Coexistence of Scale-Invariant States in Incompressible Elastomers". In: *Physical Review Letters* 111, p. 185701.

Hohlfeld, E. and L. Mahadevan (2011). "Unfolding the sulcus". In: *Physical Review Letters* 106.10.

Holland, M. A. et al. (2017). "Instabilities of soft films on compliant substrates". In: *Journal of the Mechanics and Physics of Solids* 98, pp. 350–365.

Holland, M. A. et al. (2018). "Symmetry breaking in wrinkling patterns: Gyri are universally thicker than sulci". In: *Physical Review Letters* 121, p. 228002.

Hong, W., X. Zhao, and Z. Suo (2009). "Formation of creases on the surfaces of elastomers and gels". In: *Applied Physics Letters* 95.11.

Hooke, R. (1678). *Lectures de Potentia Restitutiva, Or of Spring: Explaining the Power of Springing Bodies*. John Martyn.

Hutchinson, J. W. (2013). "The role of nonlinear substrate elasticity in the wrinkling of thin films". In: *Philosophical Transactions of the Royal Society A* 371, p. 20120422.

Jin, L. et al. (2015). "Bifurcation Diagrams for the Formation of Wrinkles or Creases in Soft Bilayers". In: *Journal of Applied Mechanics* 82.6.

Karpitschka, S. et al. (2017). "Cusp-shaped elastic creases and furrows". In: *Physical Review Letters* 119.19, p. 198001.

Khang, D.-Y. et al. (2006). "A stretchable form of single-crystal silicon for high-performance electronics on rubber substrates". In: *Science* 311.5758, pp. 208–212.

Kim, J., J. Yoon, and R. C. Hayward (2010). "Dynamic display of biomolecular patterns through an elastic creasing instability of stimuli-responsive hydrogels". In: *Nature Materials* 9, pp. 159–164.

Kohn, R. V. (July 2014). *Wrinkling of Thin Elastic Sheets*. Lecture slides. Lectures given at Park City Mathematics Institute.

Kohn, R. V. and H.-M. Nguyen (2013). "Analysis of a Compressed Thin Film Bonded to a Compliant Substrate: The Energy Scaling Law". In: *Journal of Nonlinear Science* 23.3, pp. 343–362.

Koiter, W. T. (1945). *The Stability of Elastic Equilibrium*. Thesis. Technische Hogeschool Delft.

Lacour, S. P. et al. (2004). "Design and Performance of Thin Metal Film Interconnects for Skin-Like Electronic Circuits". In: *IEEE Electron Device Letters* 25.4, pp. 179–181.

Lange, C. G. and A. C. Newell (1971). "The post-buckling problem for thin elastic shells". In: *SIAM Journal on Applied Mathematics* 21.4, pp. 605–629.

Le Tallec, P. (1994). "Numerical methods for nonlinear three-dimensional elasticity". In: vol. 3. Handbook of Numerical Analysis. Elsevier, pp. 465–622.

Lega, J. and A. Goriely (1999). "Pulses, fronts and oscillations of an elastic rod". In: *Physica D* 132, pp. 373–391.

Li, B. et al. (2011). "Surface wrinkling of mucosa induced by volumetric growth: theory, simulation and experiment". In: *Journal of the Mechanics and Physics of Solids* 59.4, pp. 758–774.

— (2012). "Mechanics of morphological instabilities and surface wrinkling in soft materials: a review". In: *Soft Matter* 8.21, pp. 5728–5745.

Melnik, A. V., H. B. Da Rocha, and A. Goriely (2015). "On the modeling of fiber dispersion in fiber-reinforced elastic materials". In: *International Journal of Non-Linear Mechanics* 75, pp. 92–106.

Menzel, A. and E. Kuhl (2012). "Frontiers in growth and remodeling". In: *Mechanics Research Communications* 42, pp. 1–14.

Mihai, L. A. et al. (2017). "A family of hyperelastic models for human brain tissue". In: *Journal of the Mechanics and Physics of Solids* 106, pp. 60–79.

Mooney, M. (1940). "A Theory of Large Elastic Deformation". In: *Journal of Applied Physics* 11.9, pp. 582–592.

Moore, G. and A. Spence (1980). "The calculation of turning points of nonlinear equations". In: *SIAM Journal on Numerical Analysis* 17.4, pp. 567–576.

Olshanskii, M. A. and L. G. Rebholz (2011). "Application of barycenter refined meshes in linear elasticity and incompressible fluid dynamics". In: *Electronic Transactions on Numerical Analysis* 38, pp. 258–274.

Pocivavsek, L. et al. (2008). "Stress and Fold Localization in Thin Elastic Membranes". In: *Science* 320.5878, pp. 932–953.

Rathgeber, F. et al. (2016). "Firedrake: automating the finite element method by composing abstractions". In: *ACM Transactions on Mathematical Software* 43.3, 24:1–24:27.

Rivlin, R. S. (1948). "Large elastic deformations of isotropic materials. I. Fundamental concepts". In: *Philosophical Transactions of the Royal Society A* 240.822, pp. 459–490.

Rodriguez, E. K., A. Hoger, and A. D. McCulloch (1994). "Stress-dependent finite growth in soft elastic tissues". In: *Journal of Biomechanics* 27.4, pp. 455–467.

Ronan, L. et al. (2013). "Differential tangential expansion as a mechanism for cortical gyrification". In: *Cerebral Cortex* 24.8, pp. 2219–2228.

Rooney, F. J. and M. M. Carroll (1984). "Generating functions for plane or axisymmetric isochoric deformations". In: *Quarterly of Applied Mathematics* 42.2, pp. 249–253.

Scott, L. R. and M. Vogelius (1985). "Norm estimates for a maximal right inverse of the divergence operator in spaces of piecewise polynomials". In: *Mathematical Modelling and Numerical Analysis* 19.1, pp. 111–143.

Skalak, R. (1981). "Growth as a finite displacement field". In: *Proceedings of the IUTAM Symposium on Finite Elasticity*. Ed. by D. E. Carlson and R. T. Shield. Springer, Dordrecht, pp. 347–355.

Skalak, R. et al. (1996). "Compatibility and the genesis of residual stress by volumetric growth". In: *Journal of Mathematical Biology* 34, pp. 889–914.

Stewart, G. W. (2001). "A Krylov-Schur Algorithm for Large Eigenproblems". In: *SIAM Journal on Matrix Analysis and Applications* 23.3, pp. 601–614.

Stewart, P. S. et al. (2016). "Wrinkling, creasing and folding in fiber-reinforced soft tissues". In: *Extreme Mechanics Letters* 8, pp. 22–29.

Sun, J.-Y. et al. (2012). "Folding wrinkles of a thin stiff layer on a soft substrate". In: *Proceedings of the Royal Society A* 468, pp. 932–953.

Taber, L. A. (1995). "Biomechanics of growth". In: *Applied Mechanics Reviews* 48.8, pp. 487–545.

Tanaka, T. et al. (1987). "Mechanical instability of gels at the phase transition". In: *Nature* 325, pp. 796–798.

Tang, S. et al. (2017). "Dimension-controlled formation of crease patterns on soft solids". In: *Soft Matter* 13, pp. 619–626.

Taylor, C. and P. Hood (1973). "A numerical solution of the Navier-Stokes equations using the finite element technique". In: *Computers & Fluids* 1.1, pp. 73–100.

Thompson, D. W. (1961). *On Growth and Form*. Abridged. Cambridge University Press.

Treloar, L. R. G. (1956). "Large Elastic Deformations in Rubberlike Materials". In: *Deformation and Flow of Solids. International Union of Theoretical and Applied Mechanics*. Ed. by R. Grammel. Springer, Berlin, Heidelberg, pp. 208–217.

Trujillo, V., J. Kim, and R. C. Hayward (2008). "Creasing instability of surface-attached hydrogels". In: *Soft Matter* 4.3, pp. 564–569.

Turing, A. M. (1952). *Can automatic calculating machines be said to think?* Typescript of broadcast discussion transmitted on BBC Third Programme, 14 and 23 Jan. 1952 between M. H. A. Newman, AMT, Sir Geoffrey Jefferson and R. B. Braithwaite.

Wang, Q. and X. Zhao (2015). "A three-dimensional phase diagram of growth-induced surface instabilities". In: *Scientific Reports* 5.

Werner, B. and A. Spence (1984). "The Computation of Symmetry-Breaking Bifurcation Points". In: *SIAM Journal on Numerical Analysis* 21.2, pp. 388–399.

Whittaker, E. T. and G. N. Watson (1920). *A Course of Modern Analysis*. Cambridge University Press.

Wong, W. H. et al. (2010). "Surface instability maps for soft materials". In: *Soft Matter* 6, pp. 5743–5750.

Xu, G. et al. (2010). "Axons pull on the brain, but tension does not drive cortical folding". In: *Journal of Biomechanical Engineering* 132, p. 071013.

Yin, J. et al. (2008). "Stress-driven buckling patterns in spheroidal core/shell structures". In: *Proceedings of the National Academy of Sciences of the United States of America* 105.49, pp. 19132–19135.